Mémoire

Auteur : Geraets, Alice
Promoteur(s) : Jehin, Emmanuel
Faculté : Faculté des Sciences
Diplôme : Master en sciences spatiales, à finalité approfondie
Année académique : 2024-2025
URI/URL : http://hdl.handle.net/2268.2/23898

Comparison of a Dynamically New and a Long period Comet's compositions using TRAPPIST

Author : Alice Geraets

Promoter: Dr. Emmanuel JEHIN

University of Liège
Faculty of Sciences
Academic Year 2024-2025

Graduation Studies conducted for obtaining the Master's degree in Space Sciences

Aknowledgements

I would like to thank Professor Emmanuel Jehin for being my promoter, as well as Mathieu Vander Bronckt for his continuous support and the help he provided. I would also like to thank the members of my committee, Damien Hutsemékers, Benoît Hubert and Johan Dekeyser for their time.

Moreover, I would like to thank every teacher in the Master in Space Sciences for sharing with me their passion of space and physics and making me love them even more. Finally, I would like to thank my friends and family for their continued support. In particular, I would like to thank my mom, Anne Geraets, for always being there for me.

Contents

Chapter 1

Introduction

Life on Earth began at the end of a period called the *Late Heavy Bombardment*, around 3.8 billion years ago. Before this, frequent collisions with interplanetary debris kept the young Earth too hot and unstable for life to develop: under this heavy bombardment of asteroids and comets, the early oceans would have vaporized, and the carbon molecules that life is built upon would have been destroyed. Despite this hostile beginning, the oldest known fossils date back to approximately 3.5 billion years ago [1], remarkably soon after the heavy bombardment ended. Some evidence even suggests that biological life may have begun almost immediately after conditions became favorable. This implies a very narrow window for the appearance of life: as soon as life could arise, it did.

This raises a fundamental question: How did life appear so quickly on a planet that, at the time, had limited surface water and organic carbon-based molecules? One possible answer lies in the small bodies of the solar system, and more specifically, comets. Not only are comets rich in water, but they also have been recently discovered to contain organic compounds crucial for the origin of life. ESA's Rosetta mission, which studied comet 67P/Churyumov–Gerasimenko, detected glycine, an important amino acid found in proteins, and phosphorus, a key component of DNA and cell membranes [2]. These findings suggest that comet collisions are what provided the molecular building blocks of life. Studying them, therefore, is crucial for uncovering the roots of biology on Earth and understanding where life comes from.

Small bodies in space didn't just supply the ingredients for life, however. They also supplied the ingredients for the planets themselves, Earth included. Our solar system as we know it today formed from grains of dust swirling in a disk around the infant Sun. Most of the material from this disk fell into the newborn star, but some bits avoided that fate and stuck together, growing into asteroids, comets, and even planets. Unlike planets, however, which have undergone significant physical and geological evolution, comets have remained largely unchanged. Formed 4.6 billion years ago, they contain primitive material from the formation of the solar system, preserved in its cold and dark outskirts ever since, far from solar radiation or planetary activity. In this sense, comets are frozen time capsules, offering

the closest physical record we have of the birth of the solar system [3].

Moreover, as our understanding of the solar system grows and astronomical technology gets more advanced, it is becoming apparent that the boundary between asteroids and comets is not as clear-cut as once thought. As telescope observations increase and we compare a large variety of astronomical objects, some objects in the Main Asteroid Belt have shown comet-like activity as part of their orbit, such as outgassing or the presence of a tail [4], despite residing in a traditionally "asteroid-like" zone. Conversely, short-period comets could ultimately evolve into asteroid-like objects after depletion of their volatile ice. This growing overlap challenges the definition of asteroids and comets and begs the question: what truly differentiates an asteroid from a comet?

Understanding comets is thus a key step in unraveling the first stages of the formation of the solar system, its current dynamics, as well as the emergence of life itself. This thesis aims to contribute to our understanding of the nature, composition, and behavior of these celestial bodies. For this purpose, we will study two comets: the dynamically new comet C/2012 K1 (PanSTARRS) and the returning long-period comet C/2013 R1 (Lovejoy). Both were observed around the time of their passage to perihelion, using the telescope TRAPPIST (TRAnsiting Planets and PlanetesImals Small Telescope) to measure their flux of light through several filters for several months.

We begin in Chapter 2 with a brief review of the history of cometary science, as well as a presentation of the general properties of comets. We will cover their origin, formation process, and composition. Chapter 3 then details the specific properties of the two comets chosen for the study, as well as how the data used for the analysis was gathered and its calibration process.

Once the data is processed, we make the measurements and finally analyze the results. Chapter 4 describes the light curves and radial profiles obtained from the cometary data. This is then used in Chapter 5, which contains the analysis of the molecular activity. In this chapter, the Haser model is used to infer the production rates of different radicals produced by the comets. The evolution of production rates as the comets move towards and away from the Sun will be followed. This will allow us to make assumptions about the composition of these two comets.

Chapter 6 covers the analysis of the dust activity of the two comets. An important quantity relating to dust activity, the $Af\rho$, is calculated and its evolution with respect to heliocentric distance is studied, as well as ratios between the production of dust and gases, which allows us to identify the taxonomy of the comets. Finally, we perform an analysis of the coma's features in Chapter 7.

Chapter 2

The state of the art

2.1 History of comets

Before beginning our study of comets, let us review what a comet is and how mankind has come to its current understanding of them. Comets have been noticed by humans for millennia, but their nature has remained mysterious for much of history. Unlike stars that decorate the night sky in a constant manner, comet appearances are ephemeral and spectacular. For this reason, they were often considered bad omens, their appearance thought to herald natural disasters or the death of an important figure.

It is only in the 16th century that scientists started developing proper theories regarding comets. Tycho Brahe and Michael Maestlin demonstrated that comets must exist outside Earth's atmosphere by measuring the parallax of the Great Comet of 1577. Through these observations, they implied that the comet's distance to Earth must be at least four times that of the Moon [5].

Isaac Newton, in his Principia Mathematica of 1687, proved that objects under the influence of gravity must follow an orbit shaped like conic sections. He pointed out that comets often appear near the Sun, and thus proposed the theory that they orbit around it. He stated regarding their luminosity that "The comets shine by the Sun's light, which they reflect".

In 1705, Edmond Halley studied 23 cometary apparitions that had occurred between 1337 and 1698. He noted that three of these, the comets of 1531, 1607, and 1682, had very similar orbital elements; notably, they had a periodic separation between their times of passage, being separated each by a period of roughly 75 years. He guessed correctly that these comets were the same, a singular comet that orbited around the Sun and was observed every time that orbit crossed or came close enough to that of Earth. Halley was able to correctly infer the date of the next passage of the comet, which is now known as Halley's Comet [6]. Human understanding of comets only improved from there. In the 18th century, scientists began to formulate correct hypotheses regarding comets' composition. In 1755, Kant suggested

that comets were made from primitive matter beyond the known planets, and Bessel in 1836 proposed, based on observations of the stream of vapors emitted by Halley's Comet, that the jet forces of evaporating material could be great enough to significantly alter a comet's orbit, arguing that the non-gravitational movements of Encke's Comet resulted from this phenomenon.
This period marked a fundamental turning point in comprehending the true nature of comets and the dynamics of their orbits. Now that the nature of comets was elucidated, scientists began studying their composition. Major scientific advances in the second half of the 19th century in the domain of photography and spectroscopy allowed the discovery of spectral emission lines in comets, revealing the main components: molecules made of hydrogen, oxygen, carbon and nitrogen, as well as dust particles such as silicates.

This led to the currently accepted model of cometary composition: the "dirty snowballs" model, suggested by the astronomer Fred Whipple in 1950 [7]. This model describes cometary nuclei as an agglutination of dust together with water ice, methane and carbon dioxide. This composition is due to the primitive nature of comets: comets were formed around the time of the formation of the solar system and have orbited in the outskirts of it ever since, where the solar radiation necessary for significant chemical alterations cannot reach them. Comets are thus made of primitive leftovers from the formation of the solar system.
As a comet follows its eccentric orbit around the Sun however, it eventually draws closer to it until the Sun's heat causes the surface ice to sublimate into jets of gas and dust. If this activity is strong enough, it causes the comet to have tails and an atmosphere called the coma; features that will be explained in the next section.

2.2 Physical structure of a comet

2.2.1 Nucleus

At the heart of every comet lies its nucleus: a solid core composed of a mixture of dust and volatile ices. Though typically only a few kilometers across, the nucleus governs the comet's behavior and is the source of all emitted material. Cometary nuclei are a mix of rock, dust, water ice, and materials such as carbon monoxide, carbon dioxide, methane, and ammonia. They are described as "dirty snowballs" [7] according to the model by Fred Whipple.

The surface of the nuclei is typically dry, dusty or rocky. Nuclei can contain a variety of organic compounds, such as methanol, hydrogen cyanide, formaldehyde, ethanol or ethane, and the amino acid glycine was found in the dust of comet 67P/Churyumov–Gerasimenko. The composition of a cometary nucleus should reflect the chemical makeup of the midplane of the protoplanetary disk where (and when) they formed [8].

Cometary nuclei are relatively small, spanning from a few hundred meters to dozens of kilometers. The biggest comet observed to this day, C/2014 UN_{271} (Bernardinelli-Bernstein),

has a nucleus of about 137 kilometers [9]. It is likely that comets with nuclei even smaller than a hundred meters exist, but have not been observed yet simply due to being too small to be detected. For this same reason, cometary nuclei tend not to be spherical: because of their low masses, unlike planets, nuclei do not have enough self-gravity to reach hydrostatic equilibrium. They also have a dark surface, with a very low albedo. For example, Halley's comet was found to reflect only about 4 percent of the light [10], which is the albedo of coal. This low reflectivity allows cometary surfaces to absorb heat, driving their outgassing processes.

2.2.2 Coma

As comets enter the inner solar system, increasing radiation from the Sun causes the ices of the nuclei to sublimate and release primary volatiles into a freely expanding atmosphere, or exosphere: the coma. This diffuse halo grows and brightens as the comet nears the Sun, and unlike the nucleus, which is relatively small, it can grow to tremendous sizes, up to 100,000 km in diameter, which is almost as large as Saturn or Jupiter [11]. About a month after an outburst in October 2007, comet 17P/Holmes even briefly had a tenuous dust atmosphere larger than the Sun [12]. Once the coma has appeared, the comet is said to be active.

The coma is generally made of cometary dust and the ices that escaped the nucleus. The most abundant volatile to escape the nucleus is water, which sublimates when a comet is within roughly 3 AU from the Sun. It, along with other parent molecules, is destroyed through photodissociation and to a smaller extent photoionization, leading to the creation of daughter molecules. Other hyper-volatile materials, such as CO and CO_2 [13], sublimate even further away from the Sun, allowing some comets to exhibit activity well before 3 AU.

Spectroscopy can be used to characterize the composition of the coma and, by inference, the nucleus. In the visible domain, this characterization leads to two taxonomic classes: carbon-typical and carbon-depleted, based on the measured abundance ratios of C_2 relative to CN [14]. In addition, near-infrared spectroscopy of fluorescent emission can be used to characterize the primary volatile composition of the coma. This characterization in turn leads to (at least) three taxonomic classes: organics-depleted, organics-normal, and organics-enriched [8], based on the measured abundance ratios of their primary volatiles relative to H_2O, the most abundant ice in comets. The composition of some comets does not fit into any of these classes, however, requiring expansion of the classification system.

Engulfing the coma is an invisible hydrogen envelope, usually distorted by the solar wind, that stretches across millions of kilometers of space. The envelope is made up of neutral hydrogen atoms, which most likely come from water vapor molecules dissociated by solar radiation [11]. Because these atoms are much lighter than the other atoms and molecules present in the coma, they are much more mobile and can thus travel longer distances before being ionized by photons and carried away by the solar wind. This is how they form a cloud of hydrogen around the coma. It is only observable by space observatories, however, as it

emits ultraviolet light, which is absorbed by the terrestrial atmosphere.

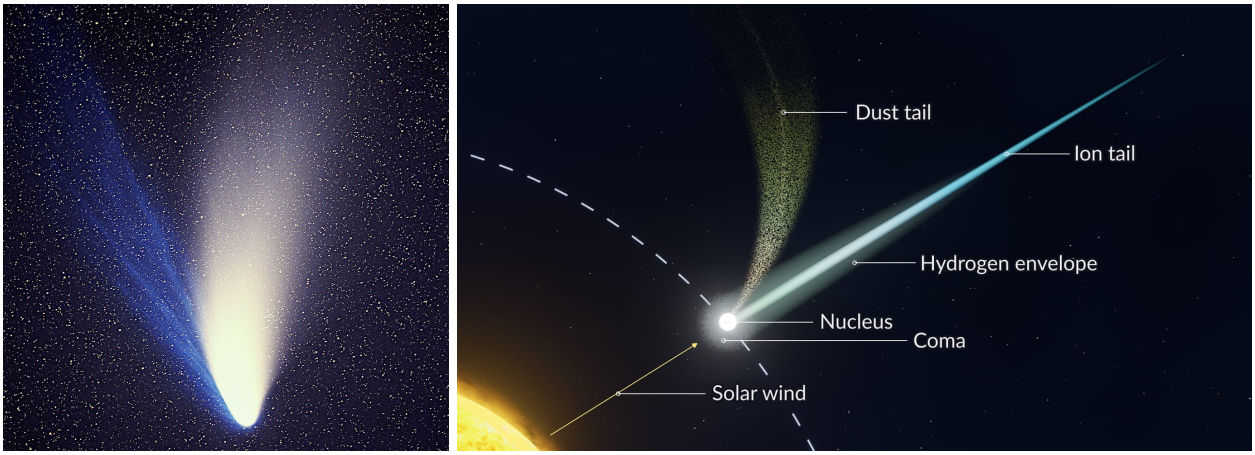

(a) Image of comet C/1995 O1 (Hale-Bopp), taken on 1997 April 04, with a 225mm f/2.0 Schmidt Camera with an exposure time of 10 minutes. Image taken from [15]

(b) Artist's view of the anatomy of a comet. Image not to scale with the actual dimensions of a comet. Image taken from [16]

Figure 2.1

2.2.3 Tails

In addition to the coma, solar radiation also causes comets to form several tails. When a comet is active, the force exerted by the Sun's radiation pressure on the coma, as well as the solar wind, pushes away particles emitted by the nuclei, including the gas of sublimated ice but also dust that got carried alongside. The dust and the gas form two distinct tails, with different properties. The *ion tail* is made of ionized gases and is strongly affected by the solar wind, following magnetic lines rather than orbital trajectory. It always points directly away from the Sun. The color of the ion tail depends on its composition. For example, the ion tail of Hale-Bopp is blue, as shown in Figure 2.1a, due to the presence of CO+ ions [17].

On the other hand, the *dust tail* is made of heavier dust particles. Unlike the ion tail, which is influenced by the solar wind due to its charged particles, this tail is largely unaffected by it. As a result, the effect of gravity is also apparent in the shape of the dust tail, making it partially trail along the orbit of the comet in addition to being pushed outward by solar radiation pressure. The result is usually a curved white tail even bigger than the coma, extending up to 10^7 km. An interesting visual feature of dust tails is that they can have striae, as seen, for example, in Figure 2.1a. These striae are generally believed to be generated by fragmentation of larger grains somewhere along their trajectories from the nucleus into the tail [18].

Tails are the most emblematic parts of a comet. In fact, the very word "comet" comes from the Greek word "$\kappa\mu\acute{\eta}\tau\eta\varsigma$" ("kometes"), which literally signifies "long hair", as a reference to the long and elegant way a comet's tails trail behind its core. The reason these tails are so visible, compared to other cometary features, lies in both their size and their reflectivity. Like the coma, the dust reflects sunlight more effectively than the darker nucleus, making active comets observable even from Earth. However, the tails and the coma also hide the nucleus, making remote determination of the composition and size more difficult. Nevertheless, the nucleus composition can still be inferred from spectroscopic analysis of the gas composition of the coma.

Figure 2.1b depicts a schematic representation of the ion and dust tails of a comet, as well as its coma, hydrogen envelope, and nucleus.

2.3 Types of comets

Comets can be classified in several ways. The first method of classification is through their periodicity. The first astronomer to identify a comet's periodicity was Edmond Halley. In 1705, Halley identified three comet passages in 1531, 1607, and 1682, and proposed the hypothesis that these comet passages were all the same object. It must be, according to him, an object on an eccentric orbit, passing at perihelion with a periodicity of roughly 75 years. He predicted the return of the comet in 1758. He was posthumously proven correct by the apparition of the comet in December 1758, which is now known as Halley's Comet. Ever since this discovery, astronomers have been able to predict the apparitions of comets in the inner solar system.

2.3.1 Periodicity

Comets are classified according to the length of their orbital period. Those with a period shorter than 200 years are referred to as *short-period comets*, or periodic comets. Comets with a period above 200 years are known as *long-period comets* (LPCs). These long-period comets tend to have highly eccentric orbits.

The threshold of 200 years is arbitrary and has been chosen mostly for historical reasons: Modern instrumental astronomy is roughly two centuries old, so long-period comets observed today are unlikely to have been observed in past observations [19].
Finally, comets that are entering the inner solar system for the first time are referred to as *dynamically new comets* (DNCs).

Tisserand parameter

Another widely used method to classify comets is the Tisserand parameter with respect to Jupiter. It is defined as:

$$T = \frac{a_J}{a} + \frac{2\sqrt{(1-e^2)a_J}}{a}\cos i, \tag{2.1}$$

where a_J is Jupiter's semi-major axis, and a, e and i respectively refer to an object's semi-major axis, eccentricity and inclination.
Comets have different orbital properties depending on the value of their Tisserand parameter, and can be grouped into families according to it. Comets with $T < 2$ are designated nearly isotropic comets, and tend to have a wider semi-major axis and therefore a longer period, and can have bigger inclinations. These comets are believed to come mainly from the Oort cloud [20]. On the other hand, comets with $T > 2$ are designated as ecliptic comets, because most members have a small inclination. They likely originate in the Kuiper belt or the scattered disk [21].

Ecliptic comets can be further divided into three groups:

- Comets with $2 < T < 3$ are known as Jupiter-family comets and are dynamically dominated by Jupiter.
- Comets with $T > 3$ are not considered members of the Jupiter family. A comet with $T > 3$ and $a < a_J$ is designated as an Encke-type, and has an orbit entirely interior to Jupiter.
- a comet with $T > 3$ and $a > a_J$ has an orbit exterior to Jupiter, and is referred to as a Chiron-type or a Centaur.

2.3.1.1 Jupiter-family comets

Comets whose aphelia are near a major planet's orbit are called its "family". Such families are thought to arise from the planet capturing formerly long-period comets into shorter orbits.

The most prominent examples of this are the Jupiter-family comets. As illustrated in Figure 2.2, they are short-period comets with orbital periods below 20 years, and low inclinations (up to 30°). Jupiter, being twice as massive as all other planets of the solar system combined, is the biggest source of gravitational perturbation for comets.

2.4 Cometary reservoirs

Gravitational interactions with the giant planets during the final phases of planet formation ejected many comets either in the Kuiper Belt or the Oort Cloud. The Kuiper Belt is a circumstellar disk beyond the orbit of Neptune, while the Oort Cloud is a spherical cloud

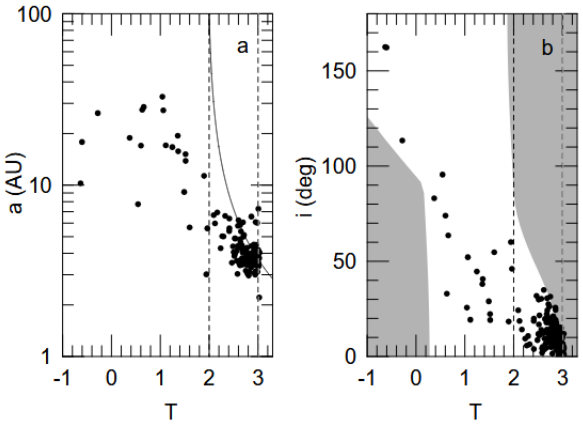

Figure 2.2: A) The semi-major axes a of observed comets with periods less than 200 years as a function of their Tisserand parameter T. B) The inclination i of the same sets of comets as a function of T. In both cases, the dashed vertical line represents the boundaries of the Jupiter family at $T = 2$ and $T = 3$. Figure taken from [21].

of icy bodies extending from outside the Kuiper Belt to halfway to the nearest star. The outer limit of the Oort cloud marks the cosmographic boundary of the outer solar system. These two regions make up the major dynamical reservoirs of the solar system for comets [8]. The Oort Cloud replenishes the reservoir of long-period comets, while the Kuiper Belt replenishes the reservoir of short-period comets.
Since entering the Oort cloud (or the Kuiper disk), the interior composition of cometary nuclei has remained largely unchanged: most processes thought to alter nuclei properties during the comet's residence in the Oort cloud (typically around 4.5 billion years) are only expected to affect a thin layer near the surface, only a few meters deep. This layer is probably lost at the first passage in the inner solar system.

The processes that placed comets in the Oort Cloud and the Kuiper Belt resulted in reservoirs that contain comets originating from different formation regions. Determining the composition of the nuclei can provide insight into these formation regions and formation pathways.

The Kuiper Belt

Comets coming from the Kuiper Belt are the remnants of the protoplanetary disk that once surrounded the Sun.

One of the most important events in the history of the solar system is the Late Heavy Bombardment, which occurred between 4.1 and 3.9 billion years ago. During this period, there was a marked increase in cometary and meteoroidal impacts on telluric planets. This bombardment is particularly notable because the surface of the Moon, at only 4 billion years old, is several hundred million years younger than the Moon itself [19].

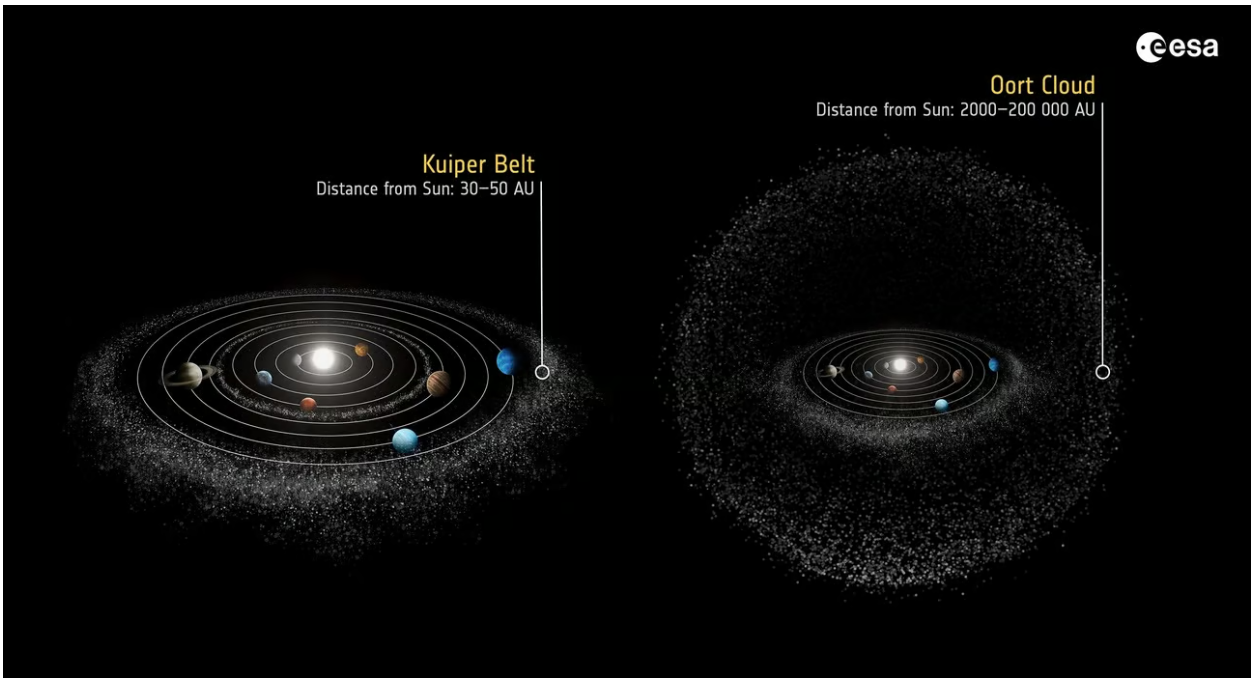

Figure 2.3: An artist's view of the Oort cloud and the Kuiper belt. This picture is not to scale with the actual dimensions of the Kuiper Belt and the Oort Cloud. Figure taken from [22].

The question arises: why was there a period of bombardment after a relative calm? The Nice model presents an explanation. According to this model, the Late Heavy Bombardment was caused by the migration of giant planets, which destabilized the existing asteroid belt.

The early solar system used to have a different configuration than its current one. It used to be more compact, and the very order of the planets was different: the two giant planets farther away from the Sun, Neptune and Uranus, had a much tighter orbit, and Neptune was closer to the Sun than Uranus. Jupiter and Saturn were relatively close to their current configuration, with a difference: Saturn was closer to the Sun than now, and Jupiter farther away from it.
At this time, Jupiter's orbital period was slightly less than half of Saturn's, meaning it completed a revolution around the Sun over twice as fast. This configuration was relatively stable, and the process of planetary formation had already cleared the inner solar system of planetesimals. The only source of debris remaining was a massive trans-Neptunian disk, containing 30 to 50 terrestrial masses, located beyond the orbits of Uranus and Neptune.

However, the system underwent a dramatic change when Saturn and Jupiter entered a 2:1 resonance. This caused Saturn's orbit to grow more eccentric, destabilizing the orbits of Uranus and Neptune as Saturn's aphelion allowed it to reach the far regions of the solar system. Neptune, as a consequence, saw its orbit doubled, growing even bigger than that of Uranus, which also increased. This increase in Neptune's orbit in turn affected the trans-

Neptunian disk. A major part of it was expelled from the solar system, and another migrated inside of the solar system, giving birth to the Kuiper belt. One last part of this debris migrated even more inward of the solar system until it collided with the terrestrial planets. This influx of material was the Late Heavy Bombardment.

The Oort Cloud

The Oort cloud occupies a vast zone between the external limit of the Kuiper belt, which ends around 50 astronomical units (AU) from the Sun. It may extend as far as a quarter to halfway toward the next nearest star, more than 150,000 AU away. Sunlight takes over 10 days to reach the Oort cloud and more than a year to reach its outer boundary. This remote region is home to hundreds of billions of icy bodies slowly orbiting around the Sun. Occasionally, the orbit of one of these bodies is disturbed, and it comes to a long fall toward the Sun.

Unlike the Kuiper Belt, comets residing within the Oort Cloud were not born there. The most widely accepted hypothesis regarding the Oort cloud formation suggests that the objects that compose it originally formed much closer to the Sun, in the gas giant region, through the same accretion process that created planets and asteroids. However, the gravitational interactions with giant planets that caused the Late Heavy Bombardment and depleted the Kuiper Belt ejected these materials into distant orbits. Some planetesimals were expelled from the solar system entirely, while others were flung into eccentric orbits, remaining bound to the Sun but far enough away that they were no longer influenced by planetary forces.

Over time, galactic tidal effects and the gravitational influence of nearby stars gradually circularized these orbits, shaping the outer Oort cloud into a sphere. Due to that spherical distribution, comets originating from the Oort cloud can come from all directions, unlike comets from the Kuiper Belt, which tend to have orbits aligned with the plane of the solar system [19].

Chapter 3

Observations and data reduction

This chapter describes how observations of the two comets were made. It begins with a description of the observatory and instruments used for data collection, followed by a presentation of the targets and the procedure used for data collection. Finally, the chapter covers the different calibration and image correction processes applied to obtain the final images.

3.1 Observatory

The observations were conducted using the TRAPPIST-South observatory. TRAPPIST-South was installed in April 2010 at the ESO LA Silla Observatory [23]. This observatory is located in the Atacama Desert, at an altitude of 2315 m. Not only does it have very good stability in the atmosphere and a low humidity level, the observatory also benefits from 300 clear nights a year.

The telescope is a 60-cm f/8 Ritchey-Chrétien design built by the German ASTELCO company, and it is equipped with a CCD broadband camera made of 2048x2048 15 μm pixels, providing a field of view of 22x22 arcminutes with a plate scale of 0.64 arcseconds per pixel. The signal-to-noise ratio of images generated with the telescope can be improved through the process of *binning*, where adjacent pixel signals are combined into larger pixels. Binning improves the signal-to-noise ratio (per shot), at the sacrifice of a reduced image resolution.

The camera has optimal efficiency at cool temperatures, which is why it is equipped with thermo-electric cooling that allows it to be kept at -35° for observations. Moreover, the telescope is also equipped with an equatorial mount, allowing for tracking and pointing of a target in the sky.

TRAPPIST-South, or TS, is a robotic observatory: the observation programme is prepared in advance and submitted to the computer controlling the telescope through software. The benefit of this method is that the telescope can be used remotely from any location

worldwide. The dome opens at sunset, and the weather is monitored constantly with a weather station, ensuring it closes under bad weather conditions, such as rain or strong winds.

A summary of the characteristics of TS can be found in Table 3.1.

(a) Close up of the 60 cm TRAPPIST-South telescope.

(b) The TRAPPIST-South telescope in its 5 metre enclosure at the La Silla Observatory, Chile.

Figure 3.1: The TS telescope. [23]

3.1.1 Filters

TS's camera is equipped with many optical filters to study astrophysical targets in a given spectral band. The filter selectively transmits only photons within the desired wavelength range, effectively isolating the band of interest and minimizing contamination from other wavelengths.

At the time of observations, the camera of TS was equipped with a double filter wheel (2x8), allowing for 14 different filter slots and one clear position per filter wheel. The first filter wheel is loaded with the broadband filters, four of which were used for this analysis: the Johnson-Cousins filters B, V, RC (hereinafter referred to as R), and Ic (hereinafter I), which cover visible and near-infrared light. The transmission profiles of the B, V, R, and I filters are shown in Figure 3.2.

The second wheel is loaded with narrowband cometary filters. Four permanently mounted filters are dedicated to isolating the main emission lines of cometary spectra: OH (310 nm),

CN (385 nm), C_3 (405 nm), and C_2 (515 nm) [24].

In addition, four narrowband dust filters, BC (445 nm), GC (526 nm), UC (334 nm) and RC (713 nm) [25] are available to estimate the solar spectrum reflected by the dust of the comet, as will be discussed in Chapter 4. The transmission profiles of these filters are shown in Figure 3.3.

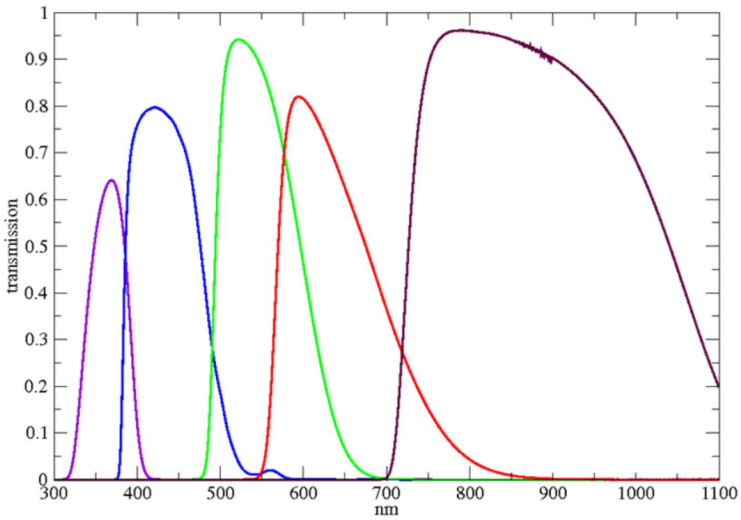

Figure 3.2: Transmission profiles for the Johnson-Cousins filters. From left to right: U, B, V, R and I.

.

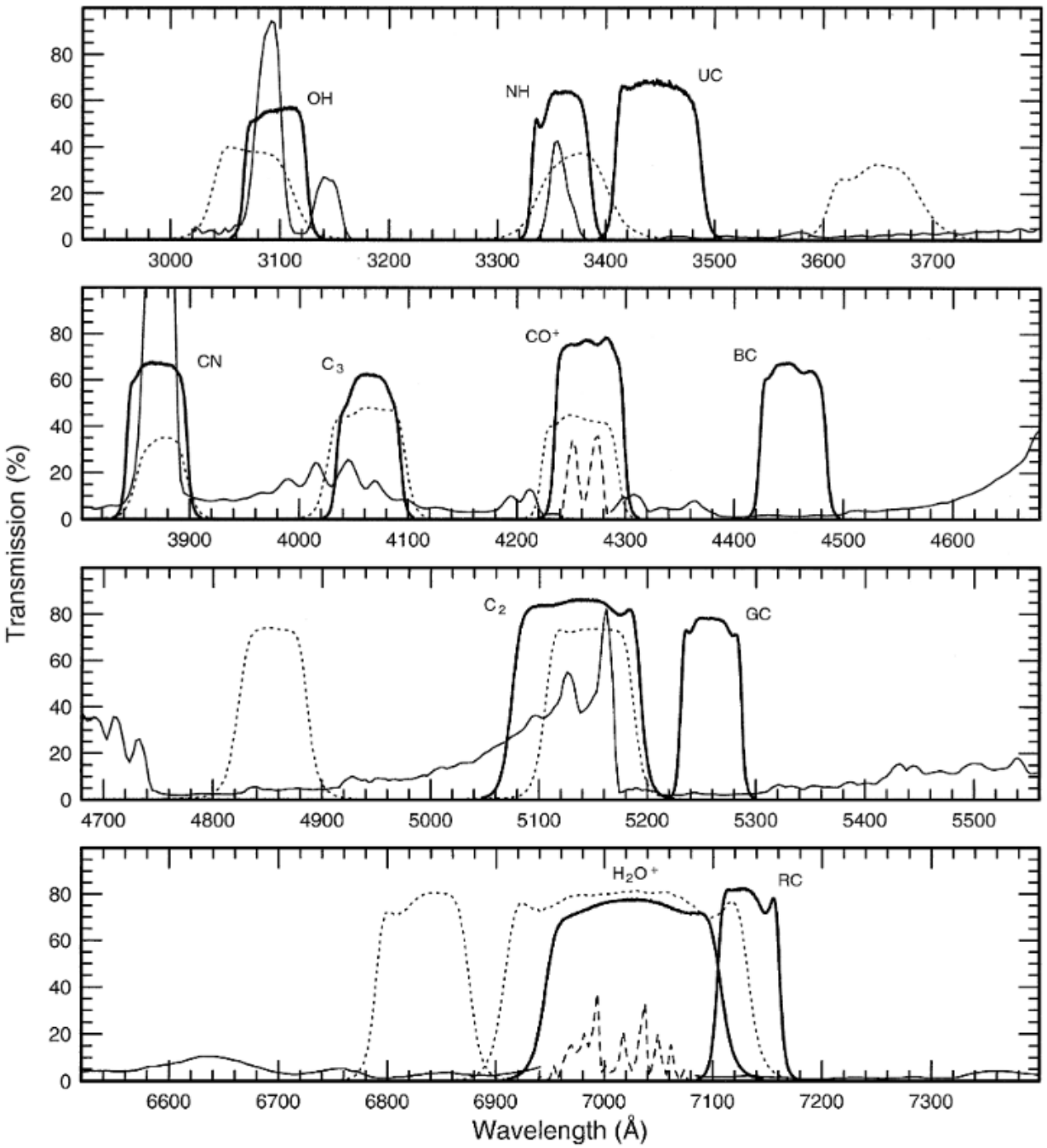

Figure 3.3: Transmission profiles for the HB filters (thick lines). For comparison, measured cometary spectra illustrate the locations of the different emission bands (thin solid lines). [24]

.

Site	La Silla Observatory (140)
Altitude (m)	2315
Latitude	29°15'16.6" (S) / 29.2546°(S)
Longitude	70 °44'121.8"(W)/ 70.7394°(W)
Telescope	Astelco RC Lightweight Telescope - Ritchey-Chretien - F/8 - 0.6 m - 75kg
Mount	Model: Astelco NTM-500 - Type: German equatorial Motors: direct drive systems - Drive accuracy: no periodic error Speed: up to 50°/s - Pointing accuracy: 5" Differential positioning accuracy: <1" RMS Tracking accuracy without autoguider: 1"/4 min
Camera model	FLI ProLine PL3041-BB
CCD type	Back-illuminated
Array size (pixels)	2048 ×2048
Pixel size (μ m)	15
Pixel scale (arcsecs/pixels)	0.64
Field of view	22'× 22'
Full well (e)	100,000
Gain (e/ADU)	1.1
Peak QE (%)	96
Read-out modes (MHz)	1 × 1 / 1 × 2/ 2 × 2
Read-out noise (e)	9.5 / 14 / 14
Read-out time (s)	6/4/2
Dark current (e/s)	0.1
Cooling below ambient (°C)	-55.0 ± 0.1
Filter Wheel model	Double Apogee AI-FW50-10S
Filters (wheel 1)	B, V, Rc, Ic, Sloan z, I+z', Exo (cut blue), NaI, H_2O^+
Filters (wheel 2)	OH, NH, CN, C_3, CO^+, BC, C_2, GC, RC

Table 3.1: Characteristics of TRAPPIST-South

3.2 Targets

The aim of this work is to analyze the light curves, molecular activity and dust activity of two comets as they pass near their point of perihelion. For this purpose, two comets were selected: C/2012 K1 (PanSTARRS) and C/2013 R1 (Lovejoy). A short description of these comets and their orbital properties is provided in this section.

3.2.1 C/2012 K1 (PanSTARRS)

The first target of this analysis is C/2012 K1 (PanSTARRS), hereinafter referred to as PanSTARRS. This comet is a retrograde Oort cloud comet. It is dynamically new and on its first journey to the inner solar system. It was originally discovered 8.7 AU from the Sun at a very feeble magnitude of 19.7 in May 2012 by the telescope Pan-STARSS (Panoramic Survey Telescope And Rapid Response System) located near the summit of Haleakalā, on the island of Maui, Hawaii [26].

The brightness of the comet continuously increased from then on as it came closer and closer to the Sun. PanSTARRS came to perihelion on 2014 August 27 at a distance of 1.05 AU from the Sun and came closest to Earth (0.95 AU) on 2014 October 21[8]. It was first a Northern Hemisphere object, then crossed the celestial equator on 15 September 2014, becoming a Southern Hemisphere object. This comet has a peculiar orbit: not only is it on a hyperbolic trajectory, meaning this passage was TS's only chance to observe it, but it is also on a retrograde and highly elliptic orbit. A list of the orbital parameters of PanSTARRS is provided in 3.2.

This comet was observed by TS during a total of 137 different nights, spanning from March 27th, 2013, to December 13th, 2015. The number of images obtained in each filter during each night of the observation period is given in Figure 3.5.

Orbital parameters	Values and uncertainties at 1-σ
Eccentricity	1.00015291 ± 0.0000008
Semi-major axis a	-6896 ± 37.74 AU
Perihelion distance q	1.05459709 ± 0.0000009 AU
Inclination with respect to ecliptic plane i	$142.4282581 \pm 0.0000049°$
Time of perihelion passage (JD)	$2456897.160363 \pm 0.000037$
Time of perihelion passage (date)	2014-Aug-27.660363 ± 0.000037
Longitude of the ascending node Ω	$317.737649 \pm 0.000017°$
Argument of perihelion ω	$203.106601 \pm 0.0000.67°$

Table 3.2: Main orbital parameters of PanSTARRS [28].

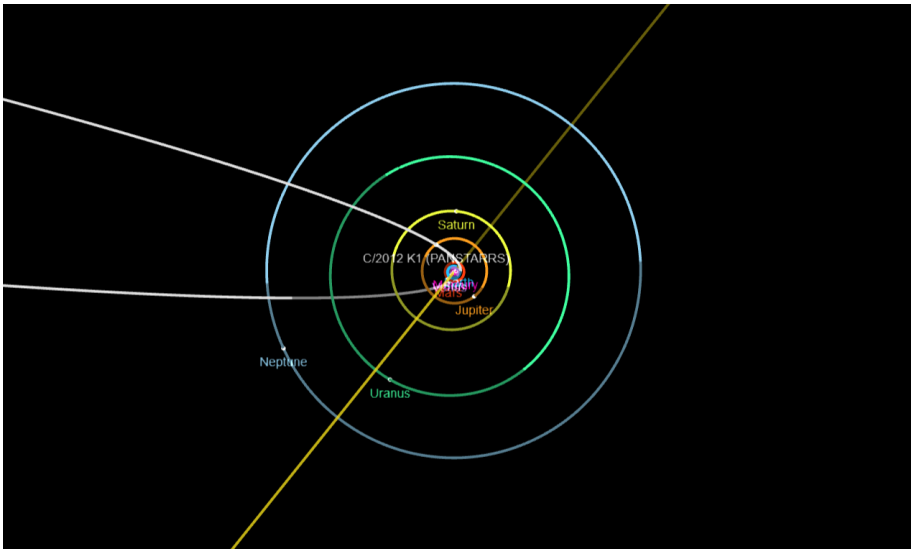

Figure 3.4: Simulation of the orbit of PanSTARRS (white) around the Sun. The location of the comet and planets is taken on the first day of observations, March 27th 2013. [27]

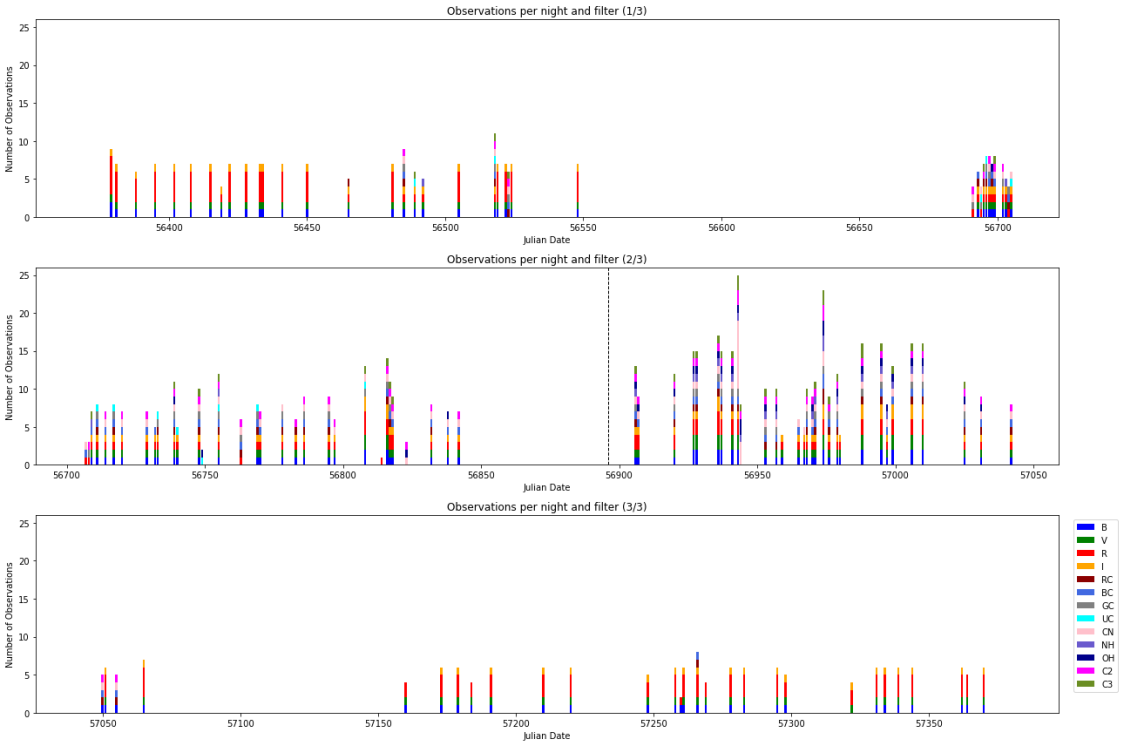

Figure 3.5: Number of observations performed on comet PanSTARRS with the different filters during each observation night, as a function of Modified Julian Day. The dashed black line indicates the date of perihelion.

3.2.2 C/2013 R1 (Lovejoy)

C/2013 R1 (Lovejoy), hereinafter referred to as Lovejoy [28], is a Long-Period Comet first discovered by Terry Lovejoy on September 7th, 2013 in Australia, using a 0.2-meter Schmidt–Cassegrain telescope [26]. It is the second target of this analysis. Much like its sister PanSTARRS, Lovejoy's relatively recent discovery is due to its increase in brightness as it reaches closer and closer to the Sun. By 1 November, 2013, Lovejoy was even visible to the naked eye, appearing with a tail and a bright, greenish coma. It reached its closest approach to Earth on 19 November 2013 at a distance of 0.3967 AU, where it had a bright apparent magnitude of about 4.5.

Unlike PanSTARSS however, Lovejoy is not on its first journey to the inner solar system. It is on an elliptical orbit, with a period of 11704 years. This sets it firmly in the category of Long-Period Comets (LPC). Lovejoy reached its most recent perihelion on December 22nd, 2013, coming as close as 0.81 AU from the Sun. An occasion that was seized by TS to observe its passage.

This comet was observed by TS during a total of 67 different nights, spanning from December 10th, 2013 to October 13th, 2014. The number of images obtained in each filter during each night of the observation period is given in Figure 3.7, and its orbital parameters are summarised in Table 3.3.

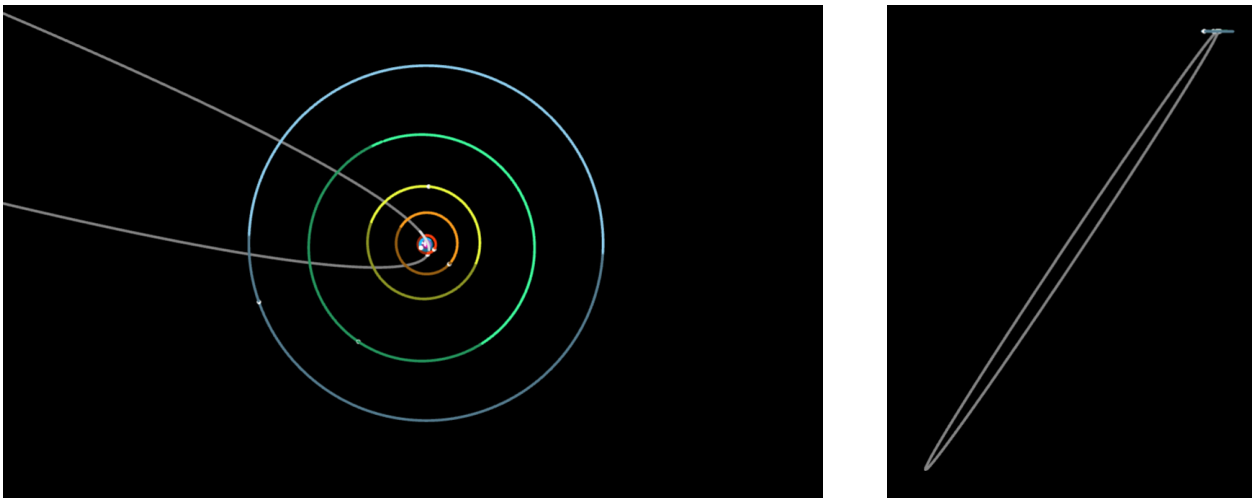

(a) (b)

Figure 3.6: Simulation of the orbit of Lovejoy (white) around the Sun at various angles. The location of the comet and planets is taken on the first day of observations, December 10th, 2013. [27]

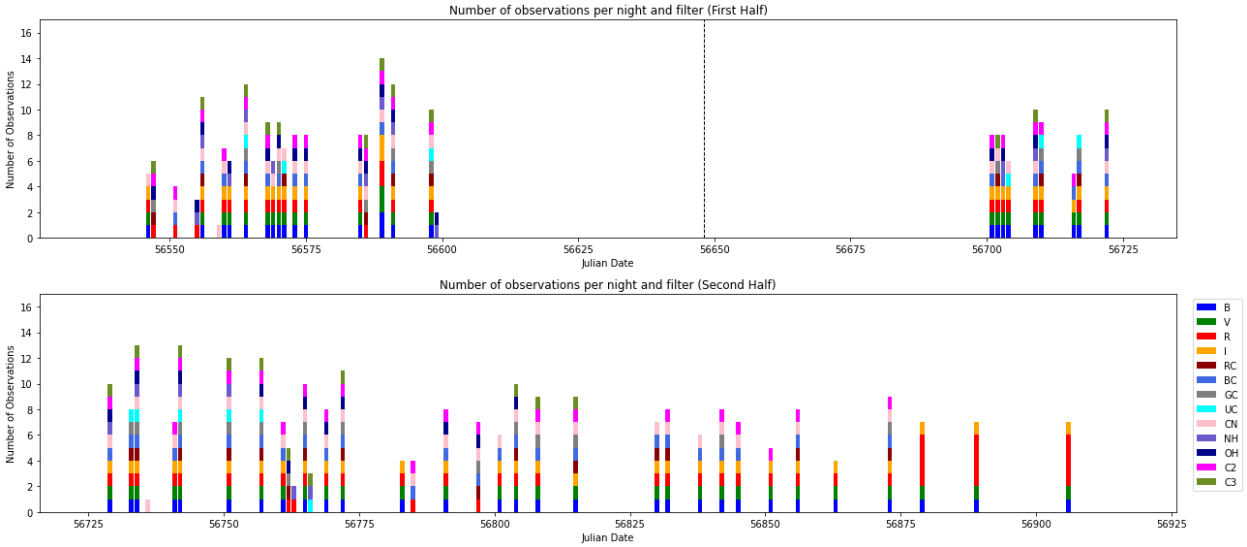

Figure 3.7: Number of observations performed on comet Lovejoy with the different filters during each observation night, as a function of Modified Julian Day. The dashed black line indicates the date of perihelion.

Figure 3.8: Comet Lovejoy. Image taken with a three-minutes exposure using a 6" Takahashi refractor located in New Mexico, on November 26 [29]. Image credit: NASA/MSFC/MEO/Aaron Kingery

.

Orbital parameters	Values and uncertainties at 1-σ
Eccentricity	0.998425 ± 0.00000053
Semi-major axis a	$515.5059403693225 \pm 0.17395$ AU
Perihelion distance q	$0.81182557 \pm 0.000000086\pm$ AU
Inclination with respect to ecliptic plane i	$64.04095258556559 \pm 0.000015°$
Time of perihelion passage (JD)	$2456649.23312175 \pm 0.0000076$
Time of perihelion passage (date)	2013-Dec-22.73312175 $\pm$0.0000076
Longitude of the ascending node Ω	$70.71117523072714 \pm 0.0000072°$
Argument of perihelion ω	$67.1664487 \pm 0.0000065°$
Orbital Period P	$11704.65759671769 \pm 5.9244$ years

Table 3.3: Main orbital parameters of comet Lovejoy [28].

3.3 Data processing

3.3.1 Calibration

Generating an image through a telescope does not immediately yield a scientific image. In order to a generate scientific image where precise flux measurement can be performed, the raw images must first be processed to get rid of unwanted signals. These include light differences caused by inequalities in the quality of different camera pixels, shadowing from dust particles on the filters or CCD window, dark currents from the CCD chip, and optical patterns of the telescope. Image calibration is therefore essential. It is performed in three steps: bias, dark and flat-fielding. This process must be repeated on every image, and the calibration images must be generated every night. If one of the calibration sets of images is missing for a given observation night, the corresponding calibration image taken from the closest available night will be used instead.

Given the large number of images, the calibration process was automated, using custom Python codes in addition to the IRAF (Image Reduction and Analysis Facility) software system. IRAF is a system developed by astronomers and programmers from the National Optical Astronomy Observatory (NOAO) in the United States that is used for the reduction and analysis of astronomical data. It allows for the automation of data reduction processes, making it useful for handling large datasets.

3.3.1.1 Bias

The first step of calibration is the bias calibration. To have a final image that represents the data only from the target, one must first remove the level zero of the CCD camera electronics, also called the offset. Bias frames are obtained by taking zero-length exposure with the shutter closed. [30] Several of these images are taken, usually 7, and then median-combined to form a so-called master bias frame. Bias images must be obtained in the same temperature and binning as the target image.

3.3.1.2 Dark

The second step is the removal of the thermal signal of the CCD chip, caused by randomly generated electrons due to the non-zero K temperature of the chip. This signal is referred to as the dark current. Its removal is done through the generation of dark frames. They are taken at the same temperature as the target image, as well as the same binning and exposure time. Several dark frames are generated, bias-subtracted and then median-combined into a single, final dark frame: the MasterDark. An example of a MasterDark is shown in Figure 3.9b.

The signal caused by thermal agitation of the electrons is proportional to the temperature and exposure time. If, for one reason or another, a dark frame wasn't made with the same

exposure time as the target image, darks can be scaled. This is called the optimisation of the dark.

3.3.1.3 Flat-Fielding

The final calibration step, called flat-fielding, aims to correct the spatial non-uniformity of the signal on the detector due to two main origins:

- Neither the filters, mirrors, nor the window of the detector have a homogeneous opacity/reflectance, due to dust or other imperfections.
- Due to manufacturing differences, the size and quantum efficiency of the CCD camera pixels vary from pixel to pixel.

These effects lead to the detector-telescope system not having a spatially uniform response. To correct for this instrumental effect, one usually takes several images of a uniform source of light, hence the term "flat-fielding." In practice, one can use the morning or evening sky as such a flat field. However, in order to avoid the effect of point sources (stars, galaxies, satellites, cosmic rays) mimicking a particularly flawed detector at the pixels hit by the stars, the telescope makes small offsets between each flat field image. Then, in most of the images, each pixel is not hit by the light of any of these sources, but only by that of the homogeneous sky background. After subtracting the bias and dark of each of these flat images, the median of these images is taken to get completely rid of the point sources. The resulting image is called a MasterFlat. An example of a MasterFlat is shown in Figure 3.9c.

These MasterFlats are used to divide the scientific images, pixel by pixel, as a pixel with a very low response to a flat field needs to be corrected by artificially increasing the flux it receives by a factor corresponding to dividing by its normalized response. Flats are taken with the same temperature, binning and importantly the same filter as the scientific images.

3.3.2 Comet Centering and identification

TS has an integrated tracker that will identify the comet based on its ephemerids and then "follow" it from image to image. However, this tracker can sometimes make mistakes, specifically by mistakenly identifying a nearby star as the comet. This is solved by manually entering the pixel coordinates of the comet for a given image, as is illustrated in Figure 3.11. The option *imcntr* of the IRAF software lets one enter a set of coordinates in the coordinate system of the image, and will then search for the brightest light source within a given box that has this coordinate as a center.

3.3.3 Removal of the sky contribution

After calibrating the science images to remove the systematic effects, another correction has to be applied to the images: the removal of the sky contribution. In addition to the light

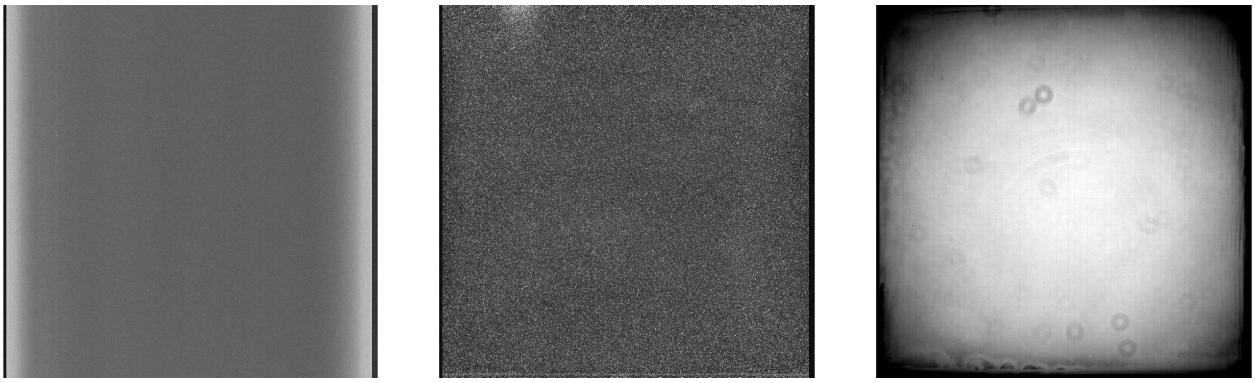

(a) Master Bias (b) Master Dark (c) Master Flat

Figure 3.9: Examples of Master Bias, Master Dark (obtained at an exposure time of 240s) and Master Flat (obtained for the I filter) frames obtained with TS and used for the calibration of an image of comet PanSTARRS collected on July 3, 2014.

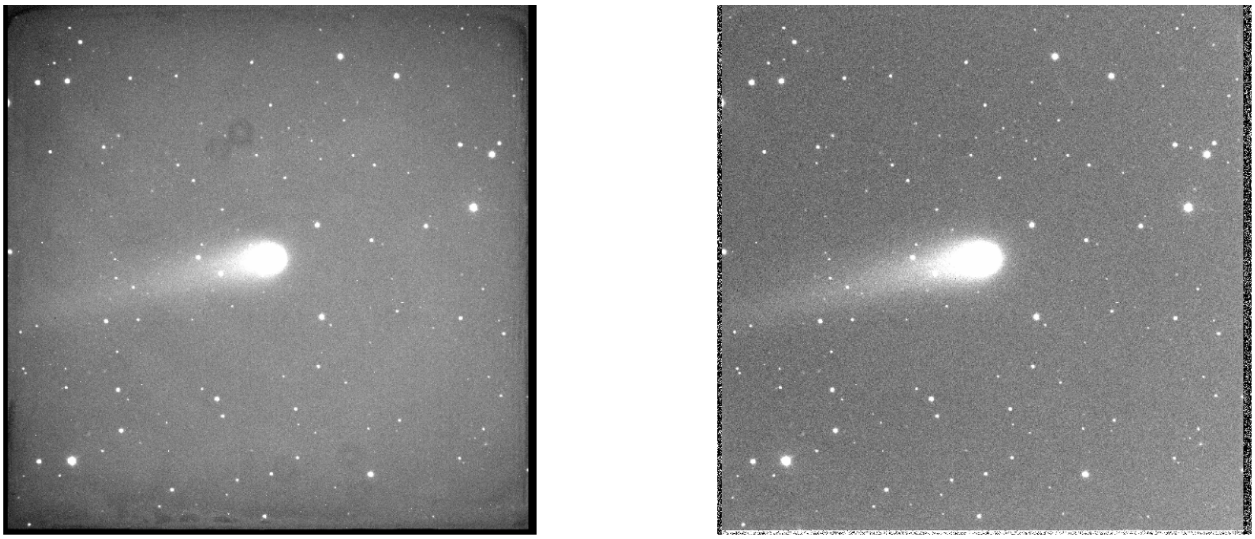

(a) Comet PanSTARRS, before calibration (b) Comet PanSTARRS, after calibration

Figure 3.10: An image of comet PanSTARRS taken on the 2nd of August, 2014 in the R filter, before and after calibration

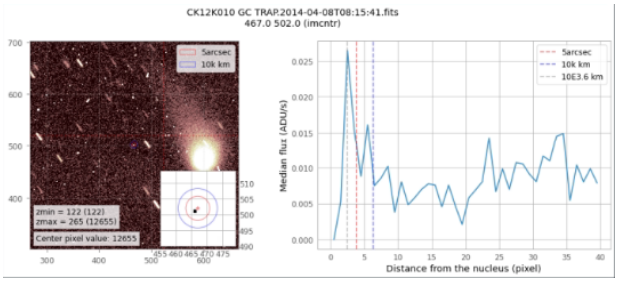

(a) Comet PanSTARRS, before calibration

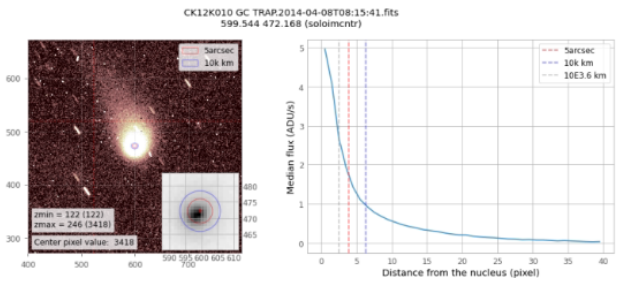

(b) Comet PanSTARRS, after calibration

Figure 3.11: A picture of comet PanSTARRS taken on the 2nd of August, 2014. In the first picture, the astrocentering was not sufficient to identify the comet, leading to poor computing of the radial profile. In the second picture, manual centering was used to correctly identify the comet, leading to a much better radial profile. For further explanation on radial profiles, see Chapter 4.

of the comet, the images may be contaminated by light emitted by the sky: this light has several possible sources, such as reflection of sunlight by the Moon, atmospheric activity, or light pollution.

How was this accounted for? We need an "average light from the sky" that we can remove from the image. For this, we need a portion of the sky that is far enough in the image from the cometary center that it is not contaminated by the comet's coma, but is nonetheless sufficiently close to it that the background sky in the area is the same as the background sky in the comet. One thus has to carefully select the area for the background sky, as, since comets are extended objects, it may be difficult to draw a limit between what is or isn't contaminated by the comet's coma.

Thankfully, the field of view of TS is quite large (20x20 arcmin), so we are usually able to select an uncontaminated area from the same image. It was done numerically: for every image, the code determines the brightest point of the coma, through IRAF's *imcntr* method. After a verification of the coordinates (and manual correction if needed), the code searched for the closest area in the image that did not contain any contamination from the coma or background star. It then computes the median flux in that area, as well as its standard deviation, before finally subtracting the obtained median flux from the whole image. The standard deviation is used for uncertainties of the sky background subtraction.

3.4 Removing outlier frames

Once the aforementioned calibration steps have been performed, photometry can in principle be conducted. However, specific parasitic events may occur that can considerably reduce the quality of a sequence of images, making it preferable to discard them.

3.4.1 Outliers due to a star passage

The first of these possible events is when our comet passes over a star. We manually check our images for possible flyovers of stars by our comet. At these moments, the flux seem to increase significantly due to the combined light of both the observed object and the star behind it. To deal with this issue, all images taken when such a contaminating star is within the observational aperture of our targets, or creates evident outliers in our light curves, are manually removed. For instance, in Figure 3.12, we see that the comet passes very close to a background star. This star will contaminate about 50% of the images generated at this date, and they will therefore need to be manually removed from the data.

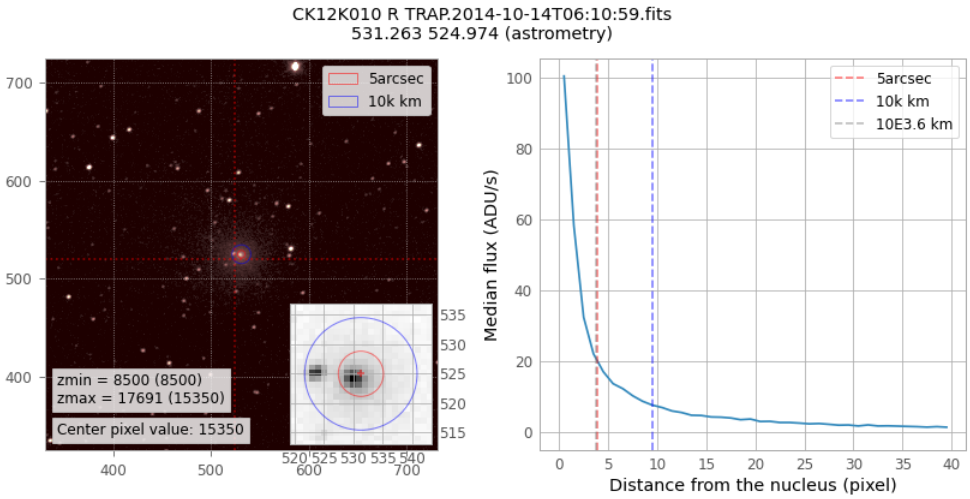

Figure 3.12: A star contaminates the flux of PanSTARRS during the night of the 13th October 2014.

3.4.2 Outliers due to poor weather

In our analysis, we do absolute photometry rather than differential photometry, which requires us to capture all the photons to correctly measure the flux from the comet. However, this method is prone to contamination by weather-related factors. For instance, a cloud passing in front of the comet during the generation of an image may cause the comet to appear fainter in the image. While such effects can be corrected in differential photometry (as the nearby stars will be similarly affected by the passing cloud, resulting in little to no change in the observed difference between the observed object and the nearby star), it will have a stronger effect in absolute photometry. As a result, most of the time we must discard the affected image as the flux will definitively be affected, and the data will not be usable. Identifying such images is not always straightforward, so it is crucial to check the status of the observation night in the observation log or the record of the weather station to ensure that weather-related anomalies are taken into account.

Chapter 4

Cometary light curves

Now that we have generated the data and undergone the various calibration and image correction processes, we are ready to analyze the data. The first result that we are going to present is the light flux of the comets in the various broadband filters. We will first compute and study the radial profiles of the flux, that is to say, the way the influx of light varies as a function of distance to the cometary center. We will then provide an analysis of the light curves of PanSTARRS and Lovejoy with respect to both time and heliocentric distance, as well as a computation and analysis of their color indices. These results will then be useful for the retrieval of molecular production ratios, as we shall see in Chapter 5.

4.1 Radial brightness profiles

We shall first study the evolution of the comet's brightness as a function of distance to its center. In other words, this section covers the generation of radial brightness profiles.

To generate a radial brightness profile for a calibrated image, we take concentric annuli of increasing radius, starting from the optocenter and extending outward toward the image's edge. Each annulus has a radial width of 1 pixel. For each annulus, the median flux of all the pixels within the annulus is calculated. This median value represents the flux at a given nucleocentric distance, in pixels. While an average could be used instead of the median, the median is preferred as it mitigates the influence of outliers, unlike the average. Iterating this process over each successive annulus allows us to construct the radial profile of the flux with respect to nucleocentric distance. The flux is expressed in ADU s^{-1}.

As an example, Figures 4.1, 4.2 and 4.3 show the radial brightness profiles of comet PanSTARRS in broadband filters B, V, R and I, as well as narrowband dust filters RC and BC, and narrowband gas filters C_2, C_3, CN and NH, during the night of April 7th, 2014. The radial profile of the gas filter OH is also present, but was selected from a later date, during the night of June 29th, 2014.

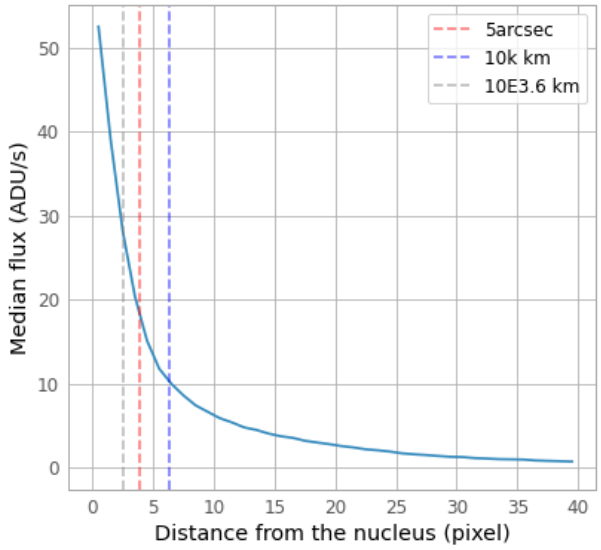

(a) B filter

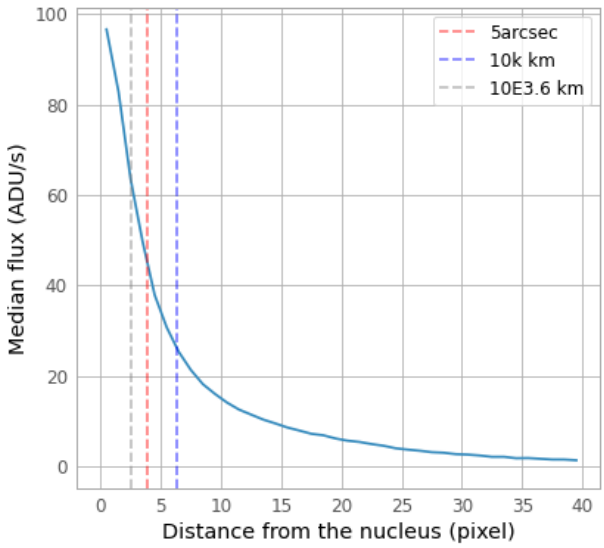

(b) V filter

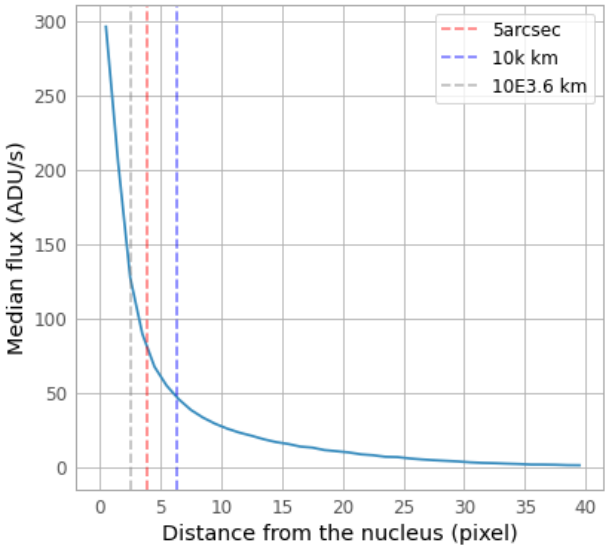

(c) R filter

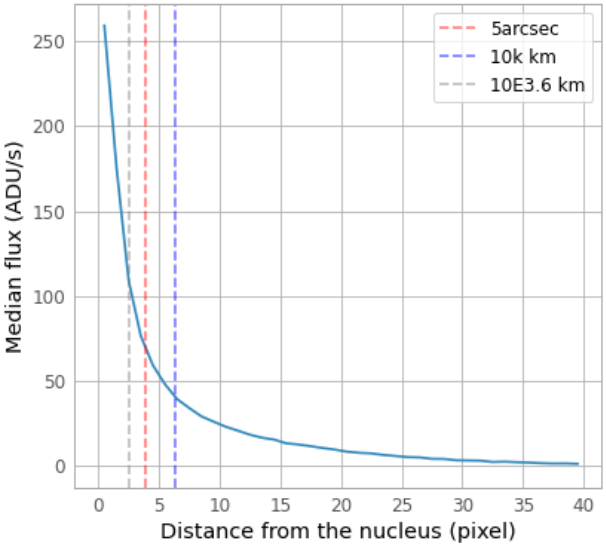

(d) I filter

Figure 4.1: Radial brightness profiles of comet PanSTARRS in the broadband filters B, V, R and I, during the night of the April 7th, 2014.

Note that the blue dotted line represents the flux at a distance of 10 000 km from the nucleus, while the red dotted line represents the flux at a distance of 5 arcseconds. These are, respectively, the radii of the nucleus-centered apertures we will use in our analysis of the evolution of the magnitude, dust, and chemical activity with respect to time (see Chapters 5 and 6.)

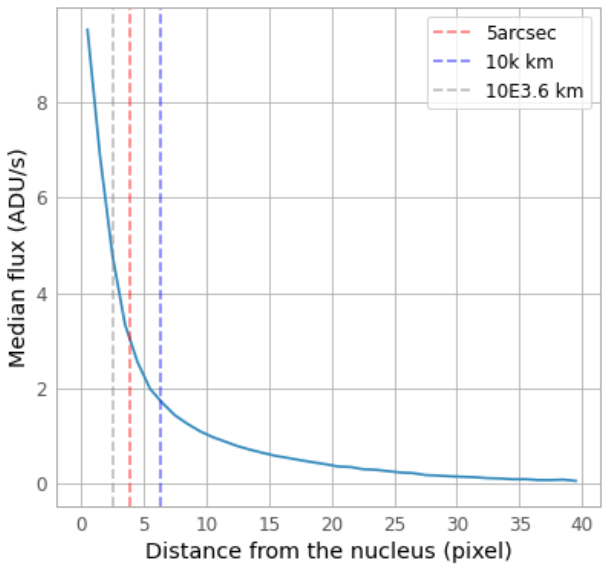

(a) RC filter

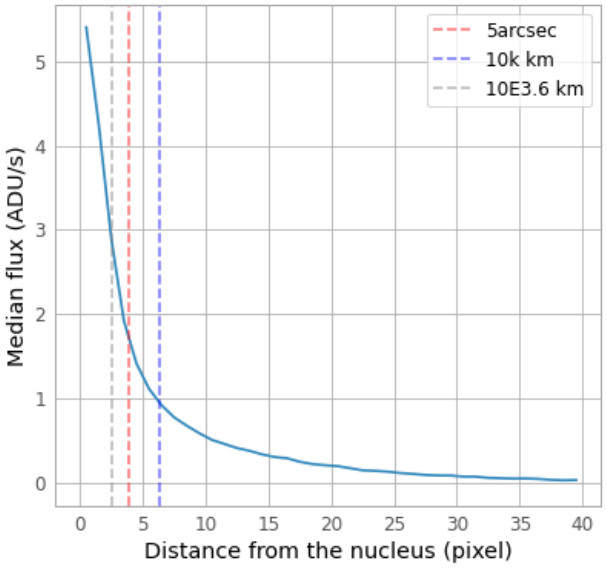

(b) GC filter

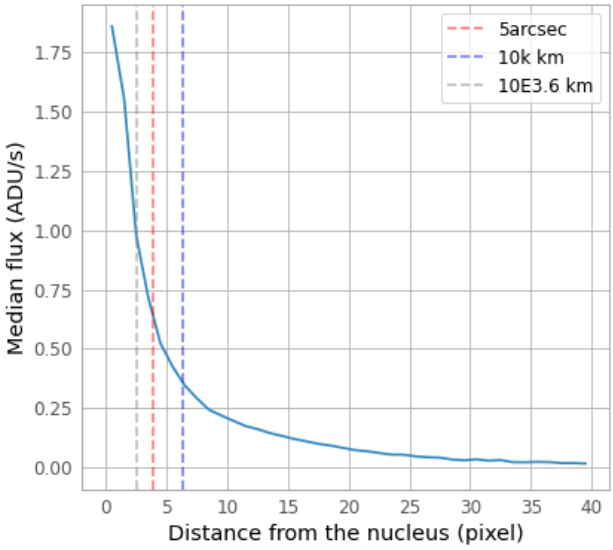

(c) BC filter

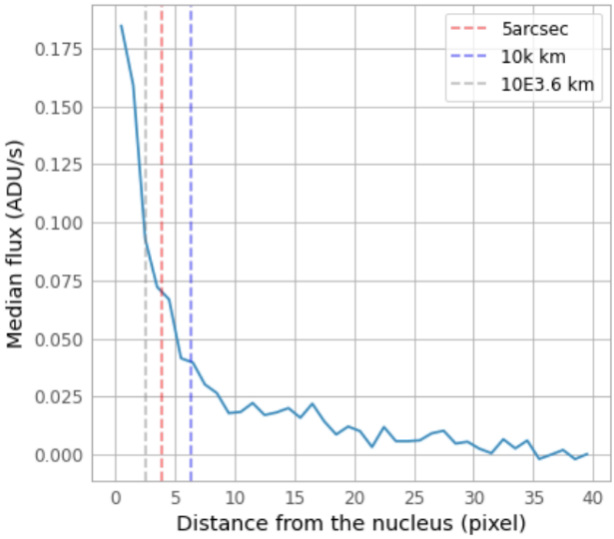

(d) UC filter

Figure 4.2: Radial brightness profiles of comet PanSTARRS in the narrowband dust filters RC, BC, GC and UC, during the night of the April 7th, 2014.

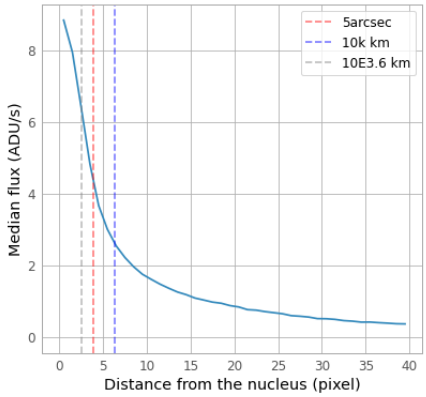

(a) C_2 filter

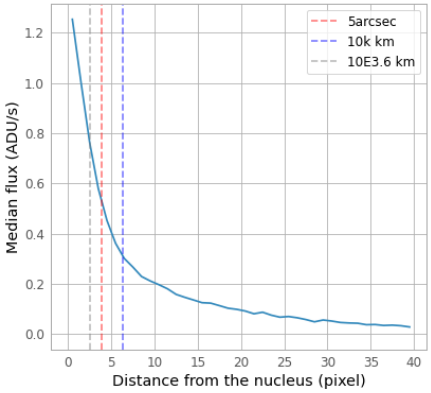

(b) C_3 filter

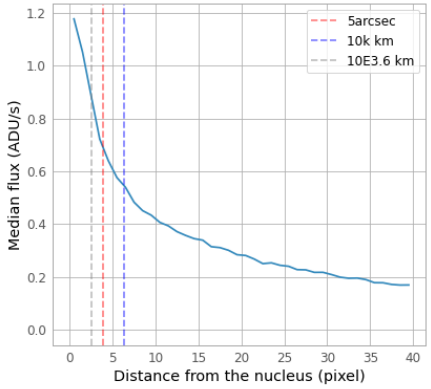

(c) CN filter

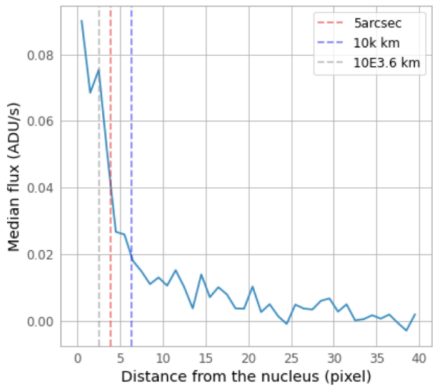

(d) NH filter

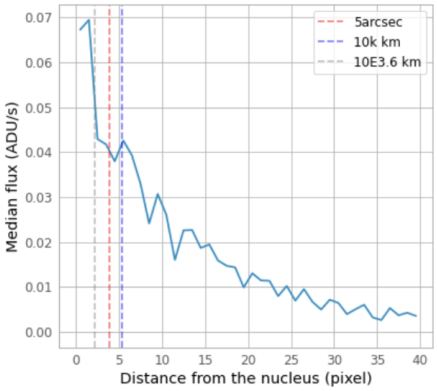

(e) OH filter

Figure 4.3: Radial brightness profiles of comet PanSTARRS in the narrowband gas filters C_2, C_3, CN and NH during the night of the April 7th, 2014, as well as OH during the night of June 29th, 2014.

The radial profiles have shapes that vary depending on the filter. For the broadband BVRI filters, we observe a sharp decrease in flux from the center until the 5 arcsec distance line, then the decrease slows down and the flux eventually evens out at zero far away from the nucleus. The exact curve varies a little, but the curve is mostly the same from one BVRI filter to another. In contrast, the profiles obtained from the gas filters show much greater variation from one filter to another, reflecting the different spatial distribution of each species. For example, the CN coma differs in shape from the dust coma or the C_2 coma. In general, gas filter profiles have a larger FWHM than those of the dust filters, as the gas coma is more extended.

Moreover, there is contamination of the gas filters by solar light from the dust and cometary grains. This is especially the case for C_2 and C_3 images, although the OH, NH, and CN images are also slightly contaminated. A correction on the radial profile of the gas filters is required to account for this effect. This is where the dust filters come into play: every night when a radial profile in a gas filter is computed, a radial profile is also computed in the BC filter, which we remind is the blue continuum filter. This filter has the advantage of being purely contaminated by dust, and not by gas emissions. This radial profile is used as a proxy for the dust contribution. It is then scaled depending on what gas filter it will be applied on, with a scale factor f_c that accounts for the "strength" of the contamination by solar light: for example, C_2 will have a big scale factor, because it is expected to be strongly contaminated by dust. A table of the scale factor in each filter can be found in 4.1. Finally, the scaled dust profile is subtracted from the gas profile.

For nights when data was available for the gas filter but not the BC filter, the BC values from the closest available night were used instead. It is worth noting that the RC filter would also have been an option as a proxy for dust contamination, but the fact that it is further away in the spectrum makes the estimation for the dust contribution less reliable, as it is farther away from the main gas emissions like CN and C_2 (see Figure 3.3).

Gas filter	Corresponding scale factor f_c
C_2	170
C_3	248
CN	30
NH	24
OH	19

Table 4.1: Scale factors f_c for the different gas filters

4.2 Flux calibration

Now that the radial profiles are adequately corrected for dust contamination, the next step is to convert said radial profiles into the correct unit. Presently, the profiles are in telescope

units ADU s^{-1}, where ADU (Analog-to-Digital Units) represents the number of detected counts per pixel. These need to be converted to physical units (erg cm^{-2} s^{-1} $Å^{-1}$).

First of all, we convert the flux from telescope units to ADU per second and $arcsec^2$. For TS, the resolution is 0.65 arcsec/pixel for a binning of 1x1 and 1.3 arcsec/pixel for a binning of 2x2.

The flux is then converted from ADU $s^{-1}arcsec^2$ to erg cm^{-2} s^{-1} $Å^{-1}$ using a formula developed by [24]. In this work, the authors used the HB filter set, a set of narrowband comet filters. They observed stars whose flux and magnitude properties were already known in the concerned spectral bands and measured their flux in ADU s^{-1}, allowing them to establish a relationship between the two quantities. We use the calibration coefficients established in this article to convert our measured flux values accordingly.
The formula is the following:

$$F_c = F_0 \cdot F \cdot 10^{0.4(K \cdot am - 25 + ZP)}. \tag{4.1}$$

Here, F_c is the cometary flux measured in a given filter, in erg cm^{-2} $s^{-1}Å^{-1}$, whereas F_0 is the flux of a zero-magnitude star (in erg cm^{-2} s^{-1}), F is the cometary flux in ADU $arcsec^{-2}s^{-1}$, am is the airmass coefficient, K is the extinction coefficient of the atmosphere, and ZP is the zero point. Let us see what these variables are and how they relate to flux calibration.

Airmass and extinction coefficient

As light traverses the atmosphere, a consequent part of it is absorbed. There is thus light extinction that depends on the wavelength (and thus on the filter) used for the observation: the smaller the wavelength, the more important the extinction. This effect needs to be accounted for in the computation of the real cometary flux. It is represented by two factors: the *airmass* (am), and the *extinction coefficient* (K). The airmass is, essentially, the quantity of atmosphere that a ray of light traverses before it reaches the detector. It is a function of the zenith angle, through the relation $am = \frac{1}{\cos(z)}$. The closer the comet is to the horizon, the more atmosphere its light has to cross to reach the detector. The airmass coefficient am is present in the header of every TS-generated image. This parameter must be as small as possible to ensure accurate data, as consequent airmass means a stronger likelihood for cometary photons to be absorbed or scattered by the atmosphere.

On the other hand, K is the extinction coefficient of the atmosphere for a given filter. Since extinction depends on wavelength, different filters will have different values of K. These values are given in Table 4.2.

Finally, The zero point of the filter ZP is a reference value corresponding to the flux of a theoretical star of magnitude zero, which would be measured with the considered filter. It

Filter	Flux at magnitude 0	Solar colors	Extinction coefficient K	ZP
OH	$10.56 \cdot 10^{-9}$	1.791	1.60	6.493
NH	$8.42 \cdot 10^{-9}$	1.188	0.65	6.183
UC	$7.802 \cdot 10^{-9}$	1.0	0.59	5.596
CN	$8.6 \cdot 10^{-9}$	1.031	0.36	5.743
C_3	$8.16 \cdot 10^{-9}$	0.497	0.29	5.693
BC	$6.21 \cdot 10^{-9}$	0.0	0.25	5.890
C_2	$3.887 \cdot 10^{-9}$	-0.423	0.15	5.010
GC	$3.616 \cdot 10^{-9}$	-0.507	0.14	5.931
RC	$1.316 \cdot 10^{-9}$	-1.276	0.05	6.447
B	$6.4 \cdot 10^{-9}$	0.0	0.25	2.452
V	$3.67 \cdot 10^{-9}$	-0.649	0.14	2.545
R	$1.92 \cdot 10^{-9}$	-1.019	0.098	2.357
I	$9.39 \cdot 10^{-9}$	-1.375	0.043	3.039

Table 4.2: For each filter, the extinction coefficient K, the flux at magnitude zero (in erg/cm^2/s/Å, taken from [24]), the magnitude of solar colors, the extinction coefficient K, and the zero point ZP of the telescope TS associated with this filter.

is different for each filter and telescope. It is provided by the TS team, which measures it using standard stars as a reference. Its value may change a bit from one night to another, and in general, a median value computed over a month is used. As an example, the median values of ZP in July 2012 are given in Table 4.2.

4.3 Light curves

With the fluxes now correctly calibrated and expressed in physical units, we can proceed to analyze the resulting light curves. This section focuses on the light curves of PanSTARRS and Lovejoy in the BVRI filters. For each observation night and each filter, we computed the integrated flux inside a 5-arcsecond circular aperture (see the dashed, red lines in Figure 4.1), and then converted it into a magnitude scale.

The resulting light curves are analyzed as a function of both time and heliocentric distance, enabling us to study the evolution of cometary brightness throughout their respective perihelion passages.

PanSTARRS

The light curve of comet PanSTARRS as a function of observation time and heliocentric distance can be found in Figure 4.4. The former is expressed in Modified Julian Day (MJD = JD - 2400000.5).

It is important to note that no observations of PanSTARRS with TS were available right before perihelion, specifically between July 3rd and September 5th, 2014, due to the comet

not being visible by TS during this period. Similarly, no observations with TS were available between September 30th, 2013 and January 19th, 2014, as well as between March 3rd, 2015 and May 10th, 2015 for the same visibility reasons.

The maximum magnitude was observed at the perihelion. Before this, the magnitude increased pre-perihelion passage with solar insulation and decreased afterward as the comet moved away from the Sun. No outbursts (brief and sharp increases in magnitude due to outgassing) were observed.

We observe different types of slopes on Figure 4.4: before 3 AU, the increase in brightness is slow. The brightness then increases more rapidly after 3 AU. A similar trend is visible post-perihelion: there are distinct regimes before and after 3 AU, with brightness decreasing more rapidly within 3 AU than beyond it. Finally, there is a steeper decrease starting at 4.7 AU post-perihelion. The feature at 3 AU is likely because at that distance, water sublimates, which causes a visible increase in activity and dust ejection. It could also be due to geometric effects, such as the varying distance between the Earth and the comet. The influence of geometric effects on the apparent light curve of PanSTARRS will be investigated further in Section 4.4.

Moreover, we can study the asymmetry of the light curve of PanSTARRS through plots comparing the evolution of magnitude as a function of heliocentric distance, before and after perihelion passage. This is done in Figure 4.3, where pre- and post-perihelion data are presented in different colors. Each phase has been fitted separately with a straight line, and the resulting slopes have been retrieved in Table 4.3. The slopes are mostly constant from one filter to another, indicating that the behavior of the magnitude does not drastically change depending on color. Notably, in each of the BVRI filters, the decline in brightness after perihelion passage is faster than its increase before perihelion passage, as evidenced by the steeper slope of the post-perihelion fit compared to its pre-perihelion counterpart. This behavior has been observed for most DNCs, where the flux tends to decline more rapidly after perihelion than it rises before [31]. However, the cause for it remains unclear.

Filter	Slope before perihelion	Slope after perihelion
B	0.90 ± 0.02	1.40 ± 0.03
V	0.89 ± 0.02	1.38 ± 0.03
R	0.86 ± 0.01	1.32 ± 0.02
I	0.89 ± 0.02	1.34 ± 0.03

Table 4.3: Slopes derived from the linear fits applied on the pre- and post-perihelion light curve of comet PanSTARRS

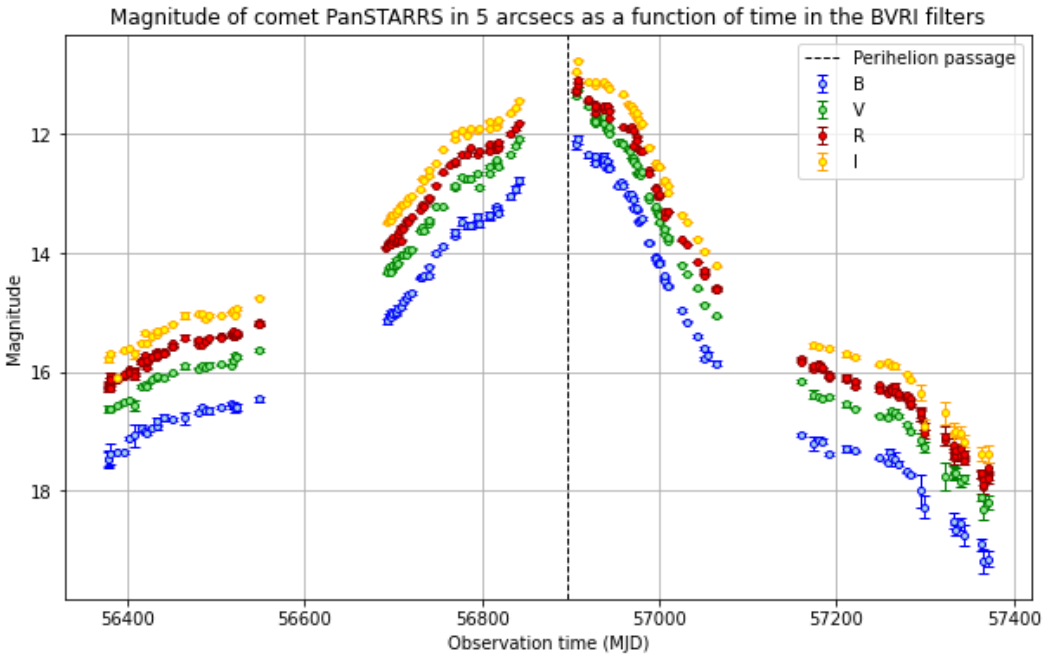

(a) Light curve of comet PanSTARRS as a function of observation time.

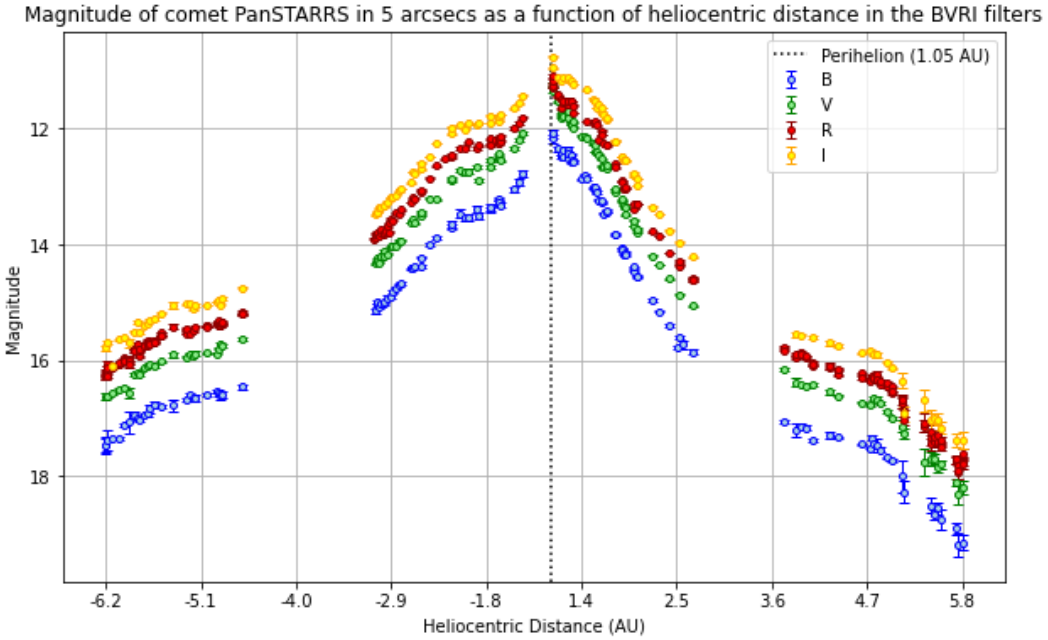

(b) Light curve of PanSTARRS as a function of heliocentric distance. The left part of the graph presents the data gathered before heliocentric passage (dotted line) and the right part presents data after perihelion passage.

Figure 4.4: Light curve of comet PanSTARRS in the BVRI filters, from March 27th, 2013 to December 13th, 2015. The magnitude at 5 arcseconds for the cometary center is displayed as a function of observation time and heliocentric distance, respectively.

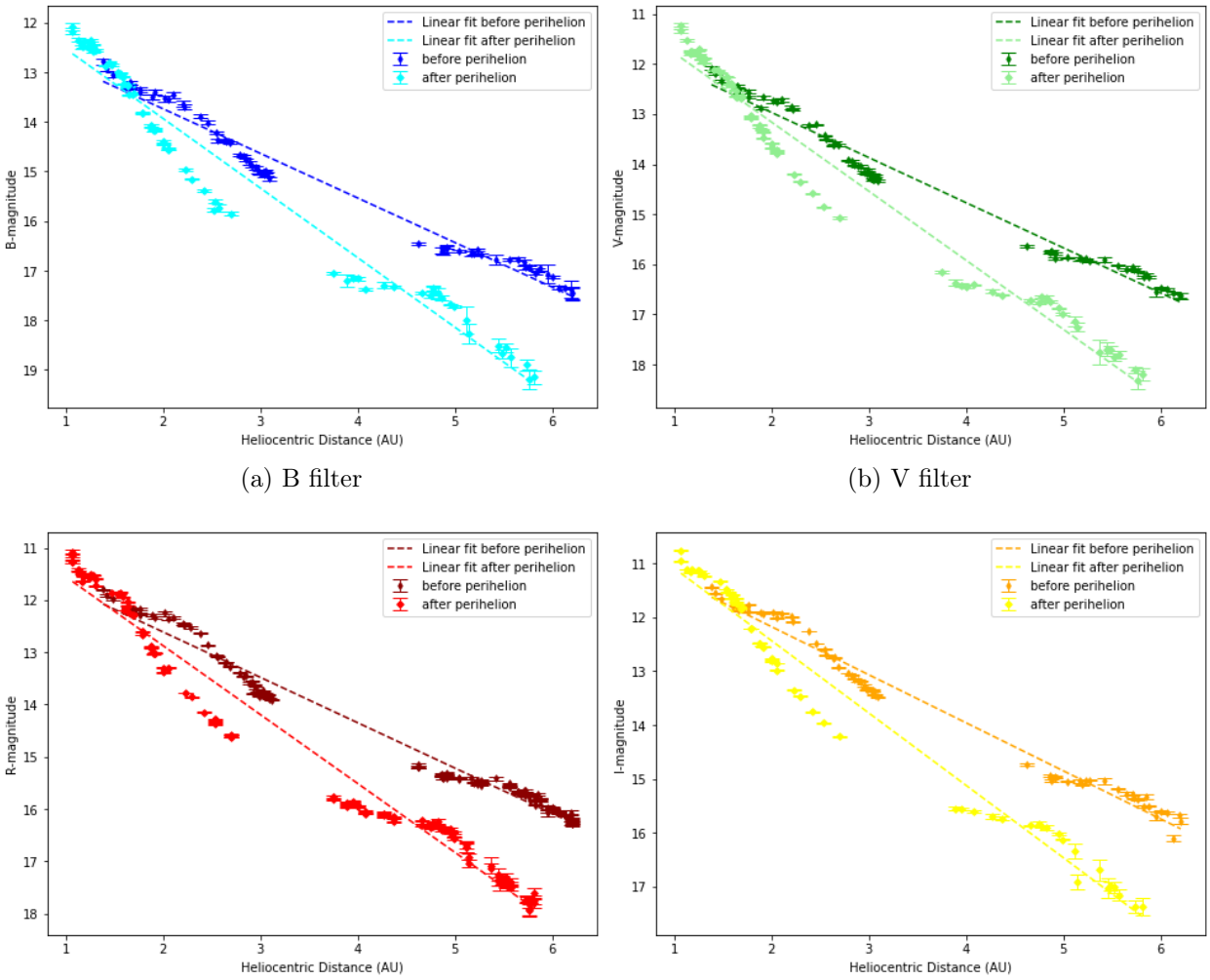

(a) B filter

(b) V filter

(c) R filter

(d) I filter

Figure 4.5: Comparison of light curves of comet PanSTARRS in the BVRI filters, before and after perihelion passage. Pre-perihelion data is presented in darker colors, while post-perihelion data is in lighter colors. Both the pre- and post-perihelion data are fitted to a straight line, represented in the respective color.

Lovejoy

The light curve of the apparent magnitude of comet Lovejoy as a function of time and heliocentric distance is shown in Figure 4.6.
As before, the magnitude increases pre-perihelion passage with solar insulation and decreases afterward. Two peaks in magnitude were observed on the nights of November 1st, 2013 (JD 56598) and February 13th, 2014 (JD 6701), at heliocentric distances of 1.228 AU and 1.256 AU, respectively. There was an observational gap around perihelion, during which no observations of Lovejoy with TS were available due to the comet not being visible by TS during this period, specifically between November 2nd, 2013 and February 13th, 2014. Given this gap, these peaks in magnitude correlate with preexisting findings that the perihelion passage occurred on December 2th, 2013, at a heliocentric distance of 0.81 AU.

As with the first comet, the asymmetry of the light curve of Lovejoy can be studied by comparing the evolution of apparent magnitude as a function of heliocentric distance, both before and after perihelion passage. This is done in Figure 4.7, and the slopes of the fit of each phase to a straight line are provided in Table 4.4. As before, the slopes remain relatively consistent across the different filters. However, unlike PanSTARRS, Lovejoy displays slopes that are steeper before perihelion than after. Moreover, both values are significantly greater for comet Lovejoy than for PanSTARRS. The pre-perihelion slopes of Lovejoy are notably more than five times higher than those of PanSTARRS. At first glance, this suggests that Lovejoy exhibited greater variability in its activity with changing heliocentric distance than PanSTARRS during the observation period.

Moreover, around 56800 MJD, the brightness rises again, displaying as a magnitude minimum of 14.8 in the R filter on the night of May 30th, 2014 (JD 56808.16), at 2.656 AU. The brightness then lowers again.

However, apparent magnitude does not solely reflect the intrinsic brightness of a comet: it is also dependent on factors related to observational geometry, such as phase angle or the comet's distance from Earth. A comet approaching Earth will appear brighter even without increased activity. In the following section, we will investigate whether these features are indeed a sign of increased activity, or if they can be attributed to these external factors.

filter	Slope before perihelion	Slope after perihelion
B	5.28 ± 0.21	2.52 ± 0.06
V	5.40 ± 0.19	2.45 ± 0.06
R	5.25 ± 0.16	2.32 ± 0.05
I	5.32 ± 0.19	2.35 ± 0.06

Table 4.4: Slopes derived from the linear fits applied on the pre- and post-perihelion light curve of comet Lovejoy.

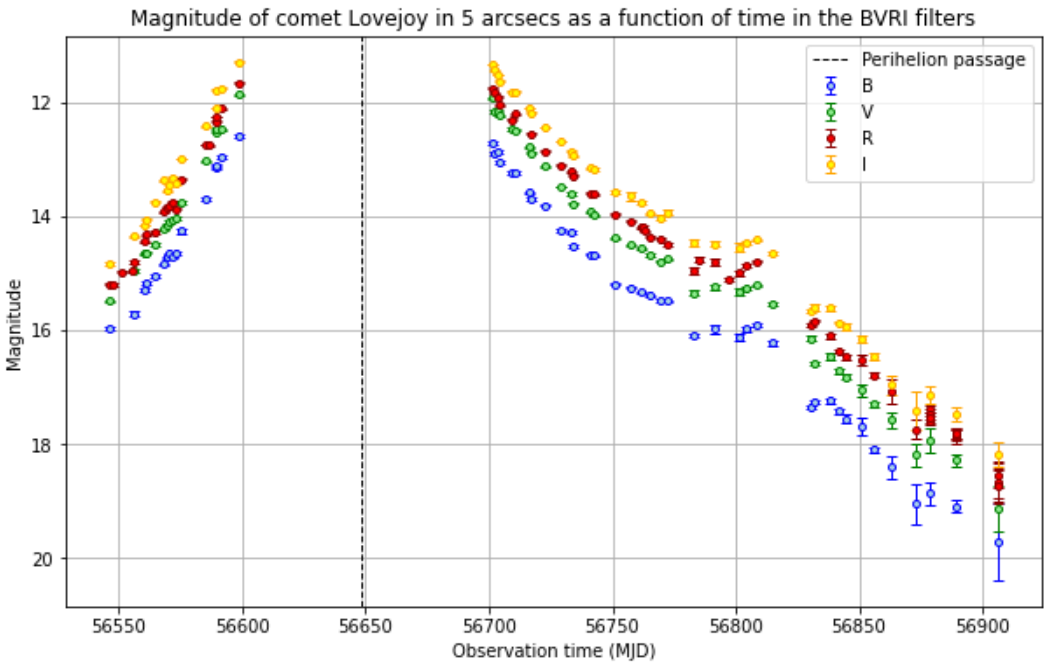

(a) Light curve of comet Lovejoy as a function of observation time

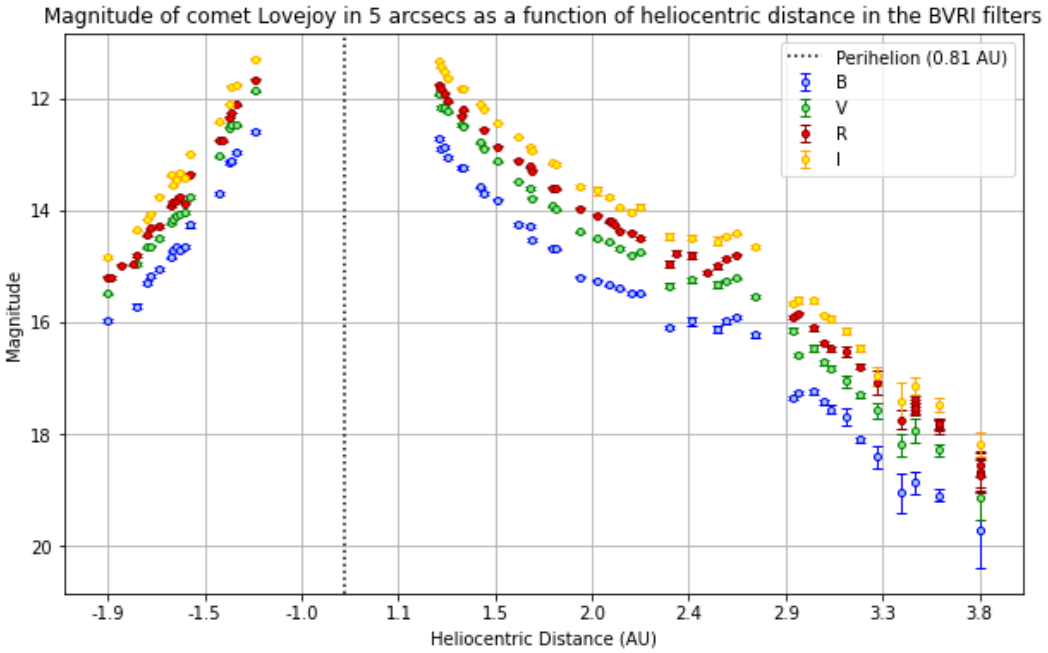

(b) Light curve of comet Lovejoy as a function of heliocentric distance

Figure 4.6: Light curve of comet Lovejoy in the BVRI filters, from the nights of September 10th, 2013 to to September 6th, 2014. The magnitude inside 5 arcseconds for the cometary center is displayed as a function of modified Julian time and heliocentric distance, respectively. In both cases, the dotted line marks the time of perihelion passage.

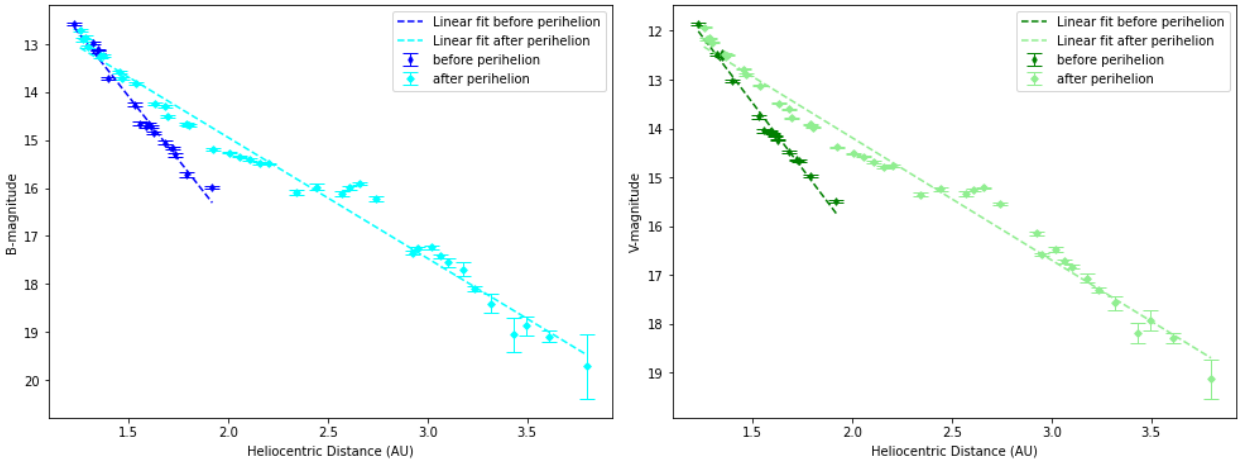

(a) B filter

(b) V filter

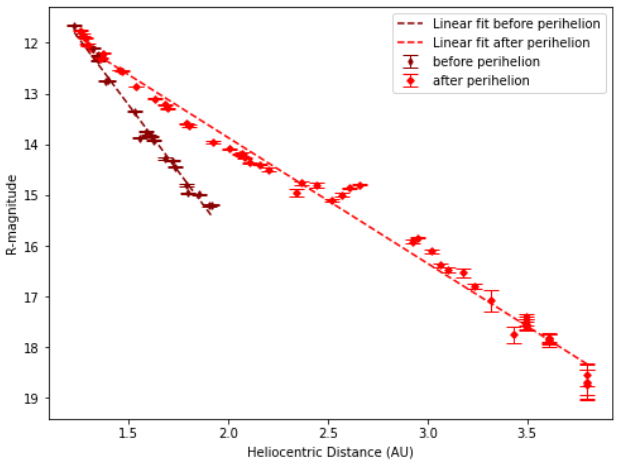

(c) R filter

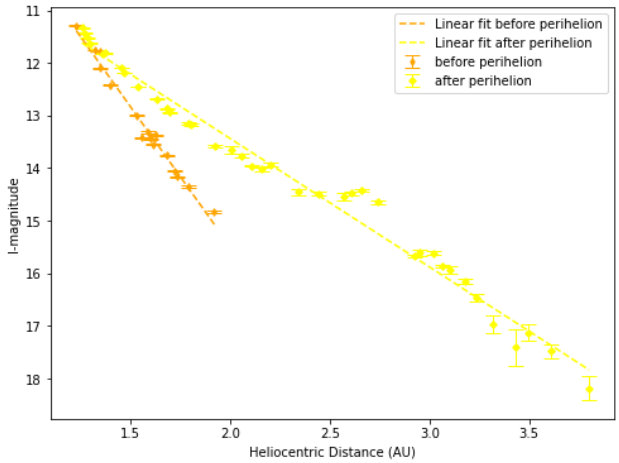

(d) I filter

Figure 4.7: comparison of light curves of comet Lovejoy in the BVRI filters, before and after perihelion passage. Pre-perihelion data is presented in darker colors, while post-perihelion data is in lighter colors. Both the pre- and post-perihelion data are fitted to a straight line, represented in the respective color.

4.4 Geometric effects: heliocentric magnitude and phase angle

As stated previously, apparent magnitude does not solely reflect variation in intrinsic brightness. To determine whether some of the features seen in Figures 4.4 and 4.6 reflect actual activity of the comet or simply an increase in light due to the comet being closer to the Earth, we compute the heliocentric magnitude in the BVRI filters. The apparent magnitude follows the following formula:

$$m = M + 5\log(\Delta) + 2.5n\log(r_h). \tag{4.2}$$

Here, m and M are the apparent and absolute magnitudes, while Δ and r_h are the geocentric and heliocentric distances, and n is the activity index [32]. The factor $5\log\Delta$ accounts for the increase in observed brightness as the comet approaches Earth. By removing this term from the observed magnitudes, as if the comet were constantly placed at Δ=1 AU, we isolate intrinsic brightness variations and present the corrected results.

Additionally, we examine the evolution of the phase angle, or Sun-Target-Observer angle, as a function of time. As will be examined further in Chapter 6, the phase angle can affect the comet's total brightness. The phase angle changes the diffraction properties of the dust in the coma: dust particles exhibit differing scattering efficiencies with phase angle. Specifically, there is a strong increase in scattering efficiency in the forward scattering direction (at a phase angle of 0°) and a smaller peak in the backward direction (180°). This dependence of the scattering properties on the phase angle causes the albedo of dust grains in the coma to change with phase angle, which in turns affects the comet's total brightness [33].

4.4.1 Heliocentric magnitude of PanSTARRS

The heliocentric magnitude of PanSTARRS is displayed as a function of time and heliocentric distance in Figures 4.8a and 4.8b, respectively. Figure 4.8a also shows the evolution of the phase angle. A fit to the parameters of Equation 4.2 was also performed, and the resulting parameters n and M are provided in Table 4.5. The parameters M and n were both computed before and after perihelion.

As expected, the behavior of M and n is consistent across all filters. For all filters, the value of the absolute magnitude M is a little bit higher after perihelion, as well as the activity index n, implying that the brightness of the comet post-perihelion is lower and decreases faster with heliocentric distance than it increased in its pre-perihelion phase.

Moreover, a new feature has appeared: the heliocentric magnitude seems to reach a minimum at 56769 MJD (2.21 AU) and 56971 MDJ (1.59 AU). However, the phase angle also reaches a maximum at both these dates; therefore, this is likely only a geometric effect, caused by the dust in the coma having a smaller albedo at that angle. Additionally, the steeper

decrease in the post-perihelion apparent magnitude beyond 4.7 AU, observed previously in Figure 4.4, has disappeared, indicating that it was only a geometric effect due to the comet's geocentric distance during that period.

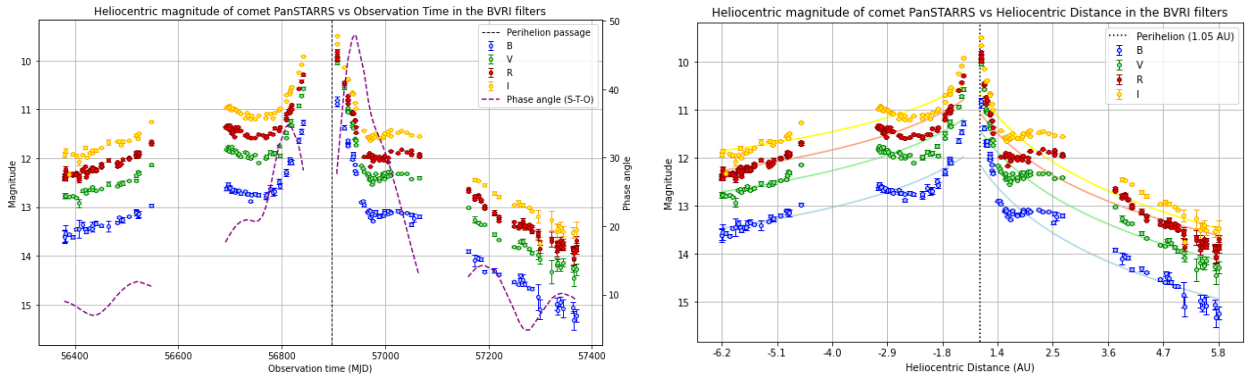

(a) Heliocentric magnitude with respect to time

(b) Heliocentric magnitude with respect to heliocentric distance

Figure 4.8: Heliocentric magnitude of comet PanSTARRS with respect to time and heliocentric distance

	M		n	
Filter	Before perihelion	After perihelion	Before perihelion	After perihelion
B	11.657 ± 0.014	12.060 $\pm$0.006	-0.364 $\pm$0.004	-0.601 $\pm$0.003
V	10.864 ± 0.008	11.342 $\pm$0.004	-0.371 $\pm$0.003	-0.583 $\pm$0.002
R	10.471 ± 0.005	10.981 $\pm$0.002	-0.361 $\pm$0.002	-0.55$\pm$0.002
I	10.191 ± 0.004	10.569 $\pm$0.003	-0.335 $\pm$0.002	-0.606 $\pm$0.002

Table 4.5: Absolute magnitude M and activity index n of the equation of magnitude fitted for comet PanSTARRS.

4.4.2 Heliocentric magnitude of Lovejoy

The heliocentric magnitude of Lovejoy is displayed in Figure 4.9. A fit to the parameters of equation 4.2 was performed, and the resulting parameters n and M are found in Table 4.6. The parameters M and n were derived separately for the pre- and post-perihelion phases.

Again, the behavior of the M and n parameters described in Table 4.6 remains consistent across all filters. The absolute magnitude M is greater before perihelion than after, indicating that the comet was more active after perihelion. In Section 4.3, when discussing the evolution of the apparent magnitude of Lovejoy, we found that the pre-perihelion slope

was steeper than that post-perihelion (see Table 4.4). However, when examining the evolution of the heliocentric magnitude, we see the opposite trend: the activity index n nearly doubles after perihelion. The steeper pre-perihelion slope observed on Lovejoy's apparent magnitude was therefore only a geometric artifact due to the target appearing brighter as it moved closer to Earth, rather than reflecting an actual property of the comet's activity. The activity of the comet post-perihelion actually decreases with heliocentric distance faster than it increased in its pre-perihelion phase.

Such asymmetry is often observed in comets, and can have several causes. One explanation is thermal inertia: cometary nuclei can accumulate heat as they get closer to the Sun, and re-emit this heat progressively as the insulation starts decreasing. This effect can explain why cometary activity can be stronger after perihelion than before it.

Another possible explanation is seasonal effects. Cometary nuclei are generally not symmetrical: they are not shaped like a sphere, and will have regions that are more active than others. As the comet orbits the Sun, changes in which surface is exposed to the Sun can lead to the activation of new regions. Some regions may also need more heat to be activated, or do so with a time delay: if the volatile material is found at a large depth, the activity of that species will be delayed due to the thermal wave needing time to reach the layer containing the volatile ice. If the number of illuminated active regions rises, this will impact the evolution of the coma [34].

Finally, the feature observed in the apparent magnitude of Lovejoy in Figure 4.6 around 56800 MJD does not disappear in heliocentric magnitude and is even more prominent. However, as indicated in Figure 4.9a, this feature also coincides with a local minimum in the phase angle, which would artificially brighten the light curve. This suggests that the feature reflects simply a geometric effect rather than a variation in intrinsic brightness. Interestingly, the date coincides exactly with the period during which Lovejoy crossed the plane of the ecliptic. In order to determine whether this peak corresponds to a genuine increase in activity or simply a geometric effect due to the phase angle, we will study in Chapter 6 whether this peak in brightness was accompanied by a corresponding increase in dust production, and in Chapter 7 whether it was accompanied by a change in the morphology of the coma.

To compare the evolution in activity of Lovejoy and PanSTARRS, we average the parameters M and n across all filters (see Table 4.7). Before perihelion, Lovejoy exhibits a larger absolute magnitude M and a steeper slope than PanSTARRS (higher absolute value of the activity index n), indicating that although PanSTARRS is initially brighter, Lovejoy's brightness increases more rapidly with decreasing heliocentric distance. After perihelion, Lovejoy maintains its steeper slope, while PanSTARRS displays a higher absolute magnitude. This increase in absolute magnitude suggests that PanSTARRS experienced a decrease in intrinsic brightness following perihelion, resulting in Lovejoy becoming the brighter comet thereafter.

Moreover, Lovejoy's consistently higher activity indices both pre- and post-perihelion indicate that it is the one whose activity is the more strongly modulated by heliocentric distance of the two. This could be due to a greater abundance of surface ice, which would enhance the comet's response to solar heating.

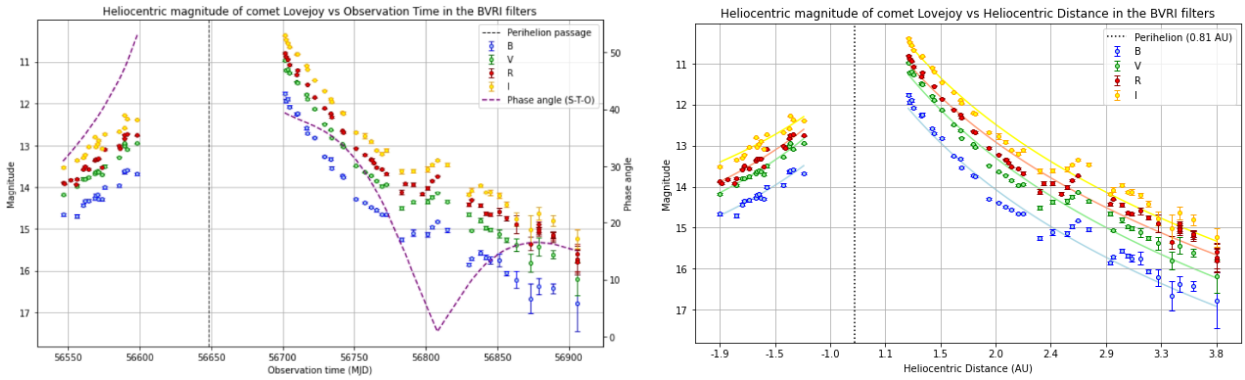

(a) Heliocentric magnitude with respect to time

(b) Heliocentric magnitude with respect to heliocentric distance

Figure 4.9: Heliocentric magnitude of comet Lovejoy with respect to time and heliocentric distance

	M		n	
Filter	Before perihelion	After perihelion	Before perihelion	After perihelion
B	12.929 ± 0.025	11.096 ±0.014	-1.002 ±0.022	-1.606 ±0.007
V	12.223 ± 0.016	10.239 ±0.009	-1.090 ±0.014	-1.650 ±0.005
R	12.013 ± 0.010	10.036 ±0.007	-1.056 ±0.008	-1.553 ±0.004
I	11.782 ± 0.007	9.509 ±0.006	-0.912 ±0.007	-1.605 ±0.008

Table 4.6: Absolute magnitude M and activity index n of the equation of magnitude fitted for comet Lovejoy.

	M		n	
Comet	Before perihelion	After perihelion	Before perihelion	After perihelion
PanSTARRS	10.795 ± 0.009	11.238 ±0.004	-0.358 ±0.004	-0.585±0.002
Lovejoy	12.237 ± 0.016	10.220 ±0.010	-1.014 ±0.007	-1.604 ±0.004

Table 4.7: Recapitulatory table: average of the absolute magnitude M and activity indices n of the equation of magnitude fitted for comets PanSTARRS and Lovejoy, across all BVRI filters.

4.5 Color indices

Color indices are commonly used to characterize the color of astronomical objects. In the case of comets, analyzing the color indices of a coma provides insight into the properties of the dust: by measuring colors, what is effectively being measured is the reflection and scattering of sunlight due to dust grains within the coma. As a result, color analysis can reveal valuable information regarding the dust grains.

In this analysis, the indices B-V, V-R, V-I and B-R of comets PanSTARRS and Lovejoy are computed. We analyze the evolution of these indices with heliocentric distance, using the following equations:

$$B - V = m_B - m_V \tag{4.3}$$
$$V - R = m_V - m_R \tag{4.4}$$
$$V - I = m_V - m_I \tag{4.5}$$
$$B - R = m_B - m_R \tag{4.6}$$

Colors of PanSTARRS

Figure 4.10 shows the evolution of the color indices of PanSTARRS with respect to heliocentric distance. The average of each index was also calculated, and is provided in Table 4.8.

First of all, a small variation of the color indices is observed with changing heliocentric distance. Notably, the index V-R decreases sharply around perihelion, reaching a minimum of 0.07 at 1.07 AU before settling around its average of 0.41 at greater distances. Similarly, the index B-R has a mean value of 1.17, but it takes a dive at low Sun-comet distances, yielding its lowest value of 0.86 at 1.25 AU. On the other hand, the other indices, B-V and R-I, do not appear to undergo significant time variations. These changes at shorter heliocentric distances are likely due to gas contamination in the B and V filters, and do not reflect a change in dust color. By comparing the bands of the B and V filters in Figure 3.2 with the gas filters in Figure 3.3, we notice that the bands of C_2, C_3 and CN overlap with the B and V bands. When the emission of these gas species is strong, such as when the comet is

close to the Sun, their emission will contribute to the flux collected in the B and V filters, causing a change in the observed color of the coma.

When compared to solar colors in Table 4.8, the mean B-R and B-V indices of PanSTARRS are slightly lower. Magnitude being an inverted scale, these lower color indices indicate that the comet is bluer and less red than solar colors.

To interpret these values, we now compare them to those commonly found in different categories of comets described in Figure 4.12, taken from [35]. PanSTARRS being a DNC, we should expect it to have a similar composition to LPCs as both originate from the Oort cloud. DNCs are first-time visitors of the inner Solar System, whereas LPCs have undergone previous perihelion passages, potentially altering their surfaces. After its first passage, a DNC can either become a returning comet, because its orbit will be altered after passing near Jupiter, or be expelled from the Solar System. Comparing the color indices of DNCs and LPCs can thus offer insight into whether such differences in dynamical history are also reflected in surface composition.

We find that the mean B-V index of 0.77 ± 0.07 is closest to that of active LPCs, which is 0.78 ± 0.02, perfectly within the margin of error. The V-R index, measured at 0.40 ± 0.04, is slightly lower but comparable to those of Jupiter Trojans (0.44 ± 0.02), JFCs (0.47 ± 0.02) and LPCs (0.47 ± 0.02). Similarly, the R-I index of 0.40 ± 0.04 aligns most closely with LPCs (0.42 ± 0.03), but could also be a JFC or a slightly redder Jupiter Trojan, both at 0.43 ± 0.02. Lastly, the B-R index of 1.17 ± 0.11 is far too low to be anything but a JFC (1.22 ± 0.02), a Trojan (1.18 ± 0.02) or a LPC (1.24 ± 0.02).

Overall, we conclude that PanSTARRS's color indices closely match that of LPCs, as well as Trojans and JFCs, while clearly differing from Centaurs, KBOs, Damocloids and Plutinos.

Index type	Index value	Solar colors [36]
B-V	0.77 ± 0.07	0.64 ± 0.02
V-R	0.41 ± 0.04	0.35 ± 0.01
R-I	0.40 ± 0.04	0.33 ± 0.01
B-R	1.17 ± 0.11	1.00 ± 0.02

Table 4.8: Mean color index values of PanSTARRS in the BVRI filters, as well as solar colors

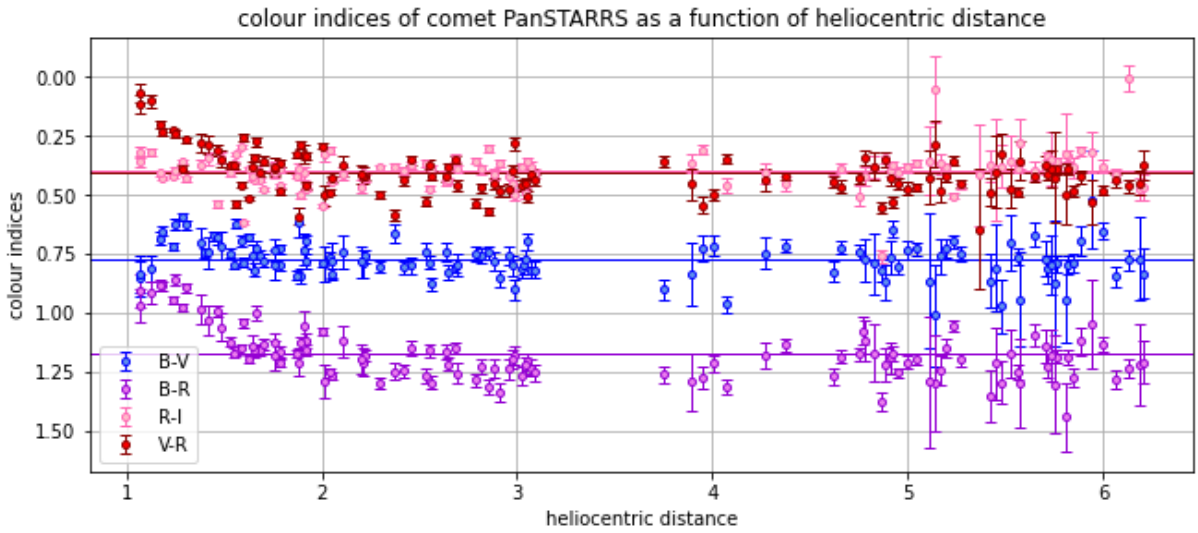

Figure 4.10: color indices of comet PanSTARRS

Colors of Lovejoy

Let us now compare the colors of PanSTARRS to those of its LPC counterpart, Lovejoy. The evolution of the color indices of Lovejoy with respect to heliocentric distance is showcased in Figure 4.11, and the average of each index is provided in Table 4.9.

Unlike PanSTARRS, Lovejoy's color indices do not display any particular evolution with respect to heliocentric distance. Comparing the mean indices to solar colors (see Table 4.9), we find that the B–R and V–R indices are relatively close to solar colors, whereas B–V and R–I are slightly elevated.

Again, let us compare those indices to those of existing categories of comets, described in Figure 4.12. As Lovejoy is a long-period comet (LPC), its color indices are expected to be consistent with those typical of this population. This holds true for the B-V indices, which closely match the average values found in LPCs, as well as JFC and Jupiter Trojans. However, the V–R index for Lovejoy (0.34 ± 0.05) is notably lower than the LPC average of 0.47 ± 0.02. Interestingly, this value remains lower than that of any other comparative comet groups. The R–I index falls well within the typical margin of error for LPCs, showing no significant deviation. As for B–R, Lovejoy's value (1.05 ± 0.15) is somewhat lower than the LPC average (1.24 ± 0.02), although still below the even higher values observed in other cometary populations.

Overall, comet Lovejoy exhibits color indices that are broadly consistent with expectations for a long-period comet, particularly in the B–V and R–I ranges. While some indices, such as V–R and B–R, deviate slightly from the typical LPC values, they nonetheless remain closer to LPC values than to those of other small body populations.

Finally, let us directly compare Lovejoy's color indices to those of PanSTARRS. To facilitate comparison, a summary table containing the color indices of both comets, along with the mean values for LPCs, is provided in Table 4.10. While their R-I indices are equal within uncertainties, Lovejoy exhibits lower B-V, V-R and B-R indices than PanSTARRS. Interestingly, despite being a DNC, it is PanSTARRS whose color indices align more closely with typical LPC values.

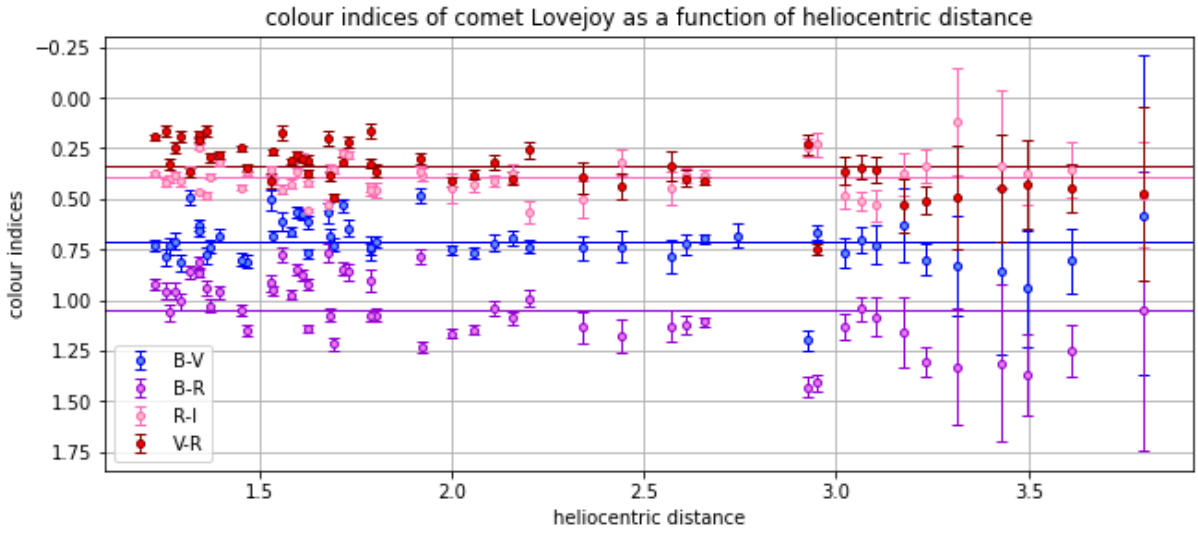

Figure 4.11: Color indices of comet Lovejoy

Index type	Index value	Solar colors [36]
B-V	0.71 ± 0.10	0.64 ± 0.02
V-R	0.34 ± 0.05	0.35 ± 0.01
R-I	0.39 ± 0.06	0.33 ± 0.01
B-R	1.05 ± 0.15	1.00 ± 0.02

Table 4.9: Mean color index values of Lovejoy in the BVRI filters, as well as solar colors

Object	$B-V$	$V-R$	$R-I$	$B-R$	Source
Cold Classical KBOs (Cold CKBO)	1.09, 1.06 ± 0.02(13)	0.64, 0.66 ± 0.02(13)	N/A	1.73, 1.72 ± 0.02(13)	Tegler online
Mean KBO Colors	0.93, 0.92 ± 0.02(85)	0.57, 0.57 ± 0.02(85)	N/A	1.52, 1.49 ± 0.03(85)	Tegler online
Plutinos	0.94, 0.93 ± 0.04(25)	0.58, 0.56 ± 0.03(25)	N/A	1.52, 1.49 ± 0.06(25)	Tegler online
Inactive Centaurs	0.85, 0.93 ± 0.04(29)	0.51, 0.55 ± 0.03(29)	0.44, 0.45 ± 0.02(3)	1.30, 1.47 ± 0.06(32)	Table 9 + Peixinho et al. (2003, 2012)
Hot Classical KBOs (Hot CKBO)	0.95, 0.89 ± 0.05(14)	0.57, 0.54 ± 0.04(14)	N/A	1.52, 1.44 ± 0.08(14)	Tegler online
Scattered KBOs (SKBO)	0.82, 0.84 ± 0.03(20)	0.54, 0.53 ± 0.02(20)	N/A	1.38, 1.37 ± 0.05(20)	Tegler online
JFC Nuclei	0.80, 0.87 ± 0.05(16)	0.49, 0.50 ± 0.03(16)	0.47, 0.46 ± 0.03(12)	1.31, 1.37 ± 0.08(12)	Lamy & Toth (2009)
Damocloids	0.79, 0.80 ± 0.02(20)	0.51, 0.51 ± 0.02(21)	0.48, 0.47 ± 0.02(15)	1.31, 1.31 ± 0.02(20)	Table 6 + Jewitt (2005)
Active Centaurs	0.80, 0.80 ± 0.03(12)	0.51, 0.50 ± 0.03(13)	0.57, 0.57 ± 0.03(8)	1.29, 1.30 ± 0.05(12)	Table 9 + Jewitt (2009)
Active LPC	0.77, 0.78 ± 0.02(25)	0.46, 0.47 ± 0.02(24)	0.41, 0.42 ± 0.03(7)	1.23, 1.24 ± 0.02(25)	Table 3
Active JFC	0.74, 0.75 ± 0.02(26)	0.46, 0.47 ± 0.02(26)	0.44, 0.43 ± 0.02(26)	1.21, 1.22 ± 0.02(26)	Solontoi et al. (2012)
LPC Nuclei	0.76, 0.77 ± 0.02(5)	0.45, 0.44 ± 0.02(5)	0.43, 0.44 ± 0.02(5)	1.22, 1.22 ± 0.03(5)	Lamy & Toth (2009)
Jupiter Trojans[c]	0.73 ± 0.02(∼1000)	0.45 ± 0.02(∼1000)	0.43 ± 0.02(∼1000)	1.18 ± 0.02(∼1000)	Szabó et al. (2007)
Sun	0.64 ± 0.02	0.35 ± 0.01	0.33 ± 0.01	0.99 ± 0.02	Holmberg et al. (2006)

Figure 4.12: Color indices of various types of comets, from [35].For each object group, the median color, the mean color with its $\pm 1\sigma$ standard error, and the number of measurements are listed.

Index type	PanSTARRS	Lovejoy	Active LPCs
B-V	0.77 ± 0.07	0.71 ± 0.10	0.78 ± 0.02
V-R	0.41 ± 0.04	0.34 ± 0.05	0.47 ± 0.02
R-I	0.40 ± 0.04	0.39 ± 0.06	0.42 ± 0.03
B-R	1.17 ± 0.11	1.05 ± 0.15	1.24 ± 0.02

Table 4.10: Recapitulatory table of the color indices of PanSTARRS, Lovejoy, and the average color indices of LPCs, taken from [35].

Chapter 5

Molecular activity

This chapter covers the computation of the gas production rates of comets PanSTARRS and Lovejoy. The production rates of OH, CN, NH, C_2 and C_3 are covered. Production ratios of OH, C_2 and C_3 with respect to CN are also computed in order to infer information about the comets' taxonomy. Finally, the water production rate is inferred from the production rate of OH.

5.1 The Haser model

The model used to calculate gas production rates in this thesis is the Haser model [37]. It is a model developed in 1957 by Leo Haser. The Haser model considers two types of molecules: parent molecules and daughter molecules. Parent molecules are directly produced by outgassing of the cometary nucleus due to solar radiation. They are then photodissociated to generate the daughter molecules, such as OH, NH, and CN. These daughter molecules emit in the visible domain and can be detected by TS through the use of cometary filters.

This model is based on the following assumptions:

- The comet has a spherical nucleus of radius r_0. Its substance is evaporated by solar radiation absorption. The molecules leave the surface in every direction, with a radial velocity v_0.
- Excited by solar light, the molecules emit their system of resonance.
- The molecules are disintegrated by photodissociation, following the law

$$n = n_0 e^{-t/\tau_0}, \tag{5.1}$$

  with n_0 being the number of molecules present at time $t = 0$, and τ_0 the average lifetime of a parent molecule.

Using these assumptions, the number of particles in a given distance ρ from the nucleus can be derived by [38]

$$n(\rho) = \frac{Q}{4\pi v \rho^2}\left(\frac{l_d}{l_p - l_d}\right)\left(e^{-\frac{\rho_n}{l_p}} - e^{-\frac{\rho_n}{l_d}}\right) \tag{5.2}$$

ρ	nucleocentric distance
$\rho_n = \rho - r_n$	reduced nucleocentric distance (r_n radius of the nucleus)
l_p, l_d	scale lengths for parent and daughter species
Q	production rate
v	gas velocity

This model is used to derive the production rates Q by fitting this equation to observation and variation of the parameters Q, l_p and l_d.

It is important to note that the Haser model is not physically accurate: cometary nuclei are not actually spherical, and the dissociation process from a parent molecule to a daughter molecule is non-radial and may happen in various steps and with various parents. Moreover, photodissociation is not the only chemical process occurring within the coma. However, despite the development of newer models since its introduction in 1957, the Haser model remains the most widely used. This is due to its simplicity of use, the similarity of its results compared to more evolved models, and its compatibility with results by different authors and in different settings. As it has been used predominantly for the past 50 years, adopting a newer model, would prevent comparison with earlier results.

Moreover, the empirical calculation of the scale length partly compensates for the simplicity of this model. In simple cases, where a parent species produces a daughter molecule through a single step, and if the parent molecule sublimes off the nucleus and expands at constant speed, the scale length can be written as $l = \tau \cdot v$ [38]. Real-life processes are usually more complex, however, with multi-step production of daughter molecules that come from several parent molecules.

5.2 Mathematical development of the Haser model

Below is the mathematical development for the Haser model, as given by [37].

Let $N(r_0)$ be the number of molecules escaping the nucleus per second and cm^2, and $N(X)$ is the same quantity at a distance X. The total number of molecules crossing a sphere of radius X is thus

$$4\pi X^2 N(X) = 4\pi r_0^2 N(r_0) \exp\left[-\frac{1}{v_0 \tau_0}(X - r_0)\right]. \tag{5.3}$$

The formation rate of the disintegration products is the number of molecules at a moment $dt + t$ that weren't there at a moment t. In terms of radius, it is all the molecules that cross a

sphere of radius $X + dX$, but that weren't there before (i.e., when the molecules crossed the sphere of radius X). The formation rate of disintegration products can thus be expressed like this:

$$-\frac{d}{dX}[4\pi X^2 N(X)] = 4\pi r_0^2 N(r_0) \cdot \frac{1}{v_0\tau_0} \exp\left[-\frac{1}{v_0\tau_0}(X - r_0)\right] \tag{5.4}$$

Assuming that the molecules are produced by successive disintegration of parent molecules, then when the molecules produced at a distance X of the nucleus reach a distance r, their number has dwindled by a factor $\exp\left[-\frac{r-X}{v_1\tau_1}\right]$, and we have

$$4\pi r_0^2 N(r_0) \cdot \frac{1}{v_0\tau_0} \exp\left[-\frac{1}{v_0\tau_0}(X - r_0)\right] \cdot \exp\left[-\frac{r - X}{v_1\tau_1}\right] \tag{5.5}$$

molecules arriving at distance r and generated in a shell of thickness dX at a distance X from the nucleus.
Therefore, the total number of daughter molecules at a distance r (per second and unit area) is obtained by integrating over X:

$$N_1(r) = N(r_0) \cdot \left[\frac{r_0}{r}^2\right] \frac{1}{v_0\tau_0} \cdot \exp\left[\frac{r_0}{v_0\tau_0}\right] \int_{r_0}^{r} \exp\left[-\frac{X}{v_0\tau_0} - \frac{r - X}{v_1\tau_1}\right] dX \tag{5.6}$$

The molecular density in the coma is

$$N(r_0) = v_0 D(r_0) \tag{5.7}$$
$$N_1(r) = v_1 D_1(r) \tag{5.8}$$

The characteristic scale length of the parent and daughter molecules in the coma, β_0 and β_1, can also be defined by:

$$\beta_0 = \frac{1}{v_0\tau_0} \tag{5.9}$$
$$\beta_1 = \frac{1}{v_1\tau_1} \tag{5.10}$$

So we obtain

$$D_1(r) = D(r_0) \cdot \frac{v_0}{v_1}\beta_0 \left[\frac{r_0}{r}^2\right] \cdot \frac{\exp(-\beta_0(r - r_0)] - \exp[-\beta_1(r - r_0)]}{\beta_1 - \beta_0} \tag{5.11}$$

We can now introduce the definition of the molecular production rate Q:

$$Q = 4\pi v_0 r_0^2 D(r_0). \tag{5.12}$$

Using equations 5.11 and 5.12, we find the following expression for the density distribution D_1 of the daughter molecules in the coma:

$$D_1(r) = \frac{Q}{4\pi v_1 r^2}\beta_0 \cdot \frac{\exp(-\beta_0(r - r_0)] - \exp[-\beta_1(r - r_0)]}{\beta_1 - \beta_0} \tag{5.13}$$

This is the Haser formula. Integrating it along the line of sight allows for finding the column density $N(r)$ of the daughter specie. This integration can be done numerically or analytically. In this work, we do it numerically, by directly integrating the molecular density along the line of sight.
Defining the emissivity $e(r)$ as

$$e(r) = \frac{1}{r^2} \cdot \frac{\beta_0}{\beta_1 - \beta_0} \cdot [\exp(-\beta_0(r)] - \exp[-\beta_1(r)]], \tag{5.14}$$

the column density can be expressed as

$$N(r) = \frac{Q}{4\pi v_1} \int_{-z}^{z} e(r) \mathrm{d}z. \tag{5.15}$$

The final step is to establish the relation between the column density of the molecules and the flux they emit. Since the emission is due to a mechanism of resonance-fluorescence, where the molecules in the coma are excited by absorbing the solar radiation and de-excite by emitting one or several photons through fluorescence, a relation exists between these two quantities in an optically thin medium [39].

$$N(r) = \frac{4\pi}{g} \frac{F}{\Omega}, \tag{5.16}$$

Here F is the flux, Ω is the solid angle, and g is the fluorescence emissivity of molecules, also called the g-factor. It corresponds to the probability per molecule and unit time of scattering a solar photon. It is expressed as

$$g_\lambda = \left(\frac{\pi e^2}{m_e c^2} \right) \lambda^2 f_\lambda F_\lambda \frac{A_{ik}}{\sum_k A_{ik}}, \tag{5.17}$$

where f_λ is the absorption oscillator strength, F_λ is the solar flux per unit wavelength, and A_{ik} are the Einstein coefficients. The fluorescent efficiency is dependent on the considered molecule, and values of the g factors are available in the literature.

Thus, the flux measured from the comet through a given narrowband gas filter can be converted into the column density of the corresponding molecular species in the coma. This column density can then be used to estimate the gas production rate of molecules.

5.3 Application of the model

In this work, the molecular production rates were computed numerically using a program that implements the Haser model. This program uses comet images obtained with TS's gas filters, subtracts the dust continuum from the radial profile using images taken with dust-only filters, and then calculates the production rates based on the Haser model using the resulting radial profiles. The lifetime, scale lengths and g-factor values necessary for computation are

taken from [14], and the orbital parameters of the comets were obtained from NASA's JPL Horizon website [28]. For each image in a given gas filter, the model was fitted between nucleocentric distances between $10^{3.6}$ km and $10^{4.1}$ km to obtain the production rate Q of the gas. This specific range was chosen because effects such as dust contamination can affect detection at smaller distance ranges, while larger ranges suffer from low SNR.

Filter	l_p (km)	l_d (km)
OH	24000	160000
NH	50000	150000
CN	13000	210000
C_3	2800	27000
C_2	22000	66000

Table 5.1: Parent (l_p) and daughter (l_d) scalelengths used in the Haser model. These values are given for a heliocentric distance of 1 AU and scale by r_h^2 [14].

5.3.1 Subtraction of the dust contamination

Contamination by other gases is negligible in the chosen filters, but not dust, which can in fact contaminate images. So, every time a radial profile is made in a gas filter, a complementary radial profile is made in the dust filter BC during the same night. They have to be made close in time because dust activity varies relatively fast (notably due to the rotation of the nucleus).

Similarly to Section 4.1, the dust profile is multiplied by a factor $\mathbf{f_c}$ and subtracted from the gas profile. This factor puts the continuum to the correct scale and depends on the relative importance of contamination in the various filters. For example, it is very weak in the OH and CN filters, as the solar spectrum is weaker in these wavelengths, but stronger in the C_2 and C_3 filters. The values of the f_c factor in the different filters are shown in the Table 4.1.

5.4 Results

5.4.1 Gas production rates

The production rates of CN, NH, C_2 and C_3 with respect to Julian day and heliocentric distance are presented in this section.

Gas production rate: PanSTARRS

The production rates of comet PanSTARRS with respect to time and heliocentric distance are shown in Figures 5.1 and 5.2. The evolution of these production rates was also fitted with

a power-law, and the resulting slopes are listed in Table 5.2. The behavior of the production rate is consistent across all gas filters: it increases before perihelion and decreases afterward. While the absolute maximum of the production rate coincides with perihelion, a local peak in emission also occurs later, around 56941 MJD, after which the production rate declines again. This secondary peak is particularly prominent in the OH filter. No corresponding peak in brightness is seen in the magnitude light curve shown in Figure 4.4.

Filter	r_h-dependence before perihelion passage	r_h-dependence after perihelion passage
OH	Not enough data	-1.59 ± 0.11
NH	Not enough data	-5.94 ± 0.22
CN	-1.13 ± 0.06	-1.73 ± 0.03
C_3	-4.05 ± 0.46	-2.34 ± 0.07
C_2	-1.43 ± 0.06	-2.48 ± 0.03

Table 5.2: Fitted power-law slopes of the r_h-dependence of the OH, NH, CN, C_3 and C_2 production rates of comet PanSTARRS, before and after perihelion passage.

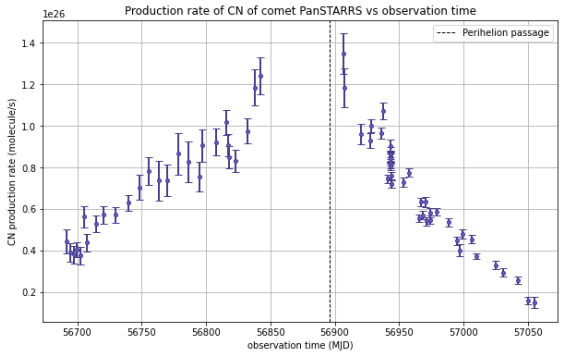

(a) Gas production rates of CN with respect to observation time

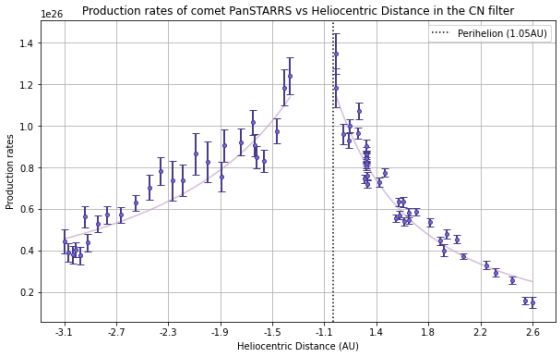

(b) Gas production rates of CN with respect to heliocentric distance

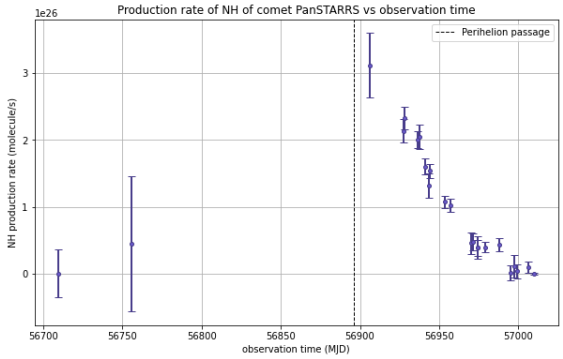

(c) Gas production rates of NH with respect to observation time

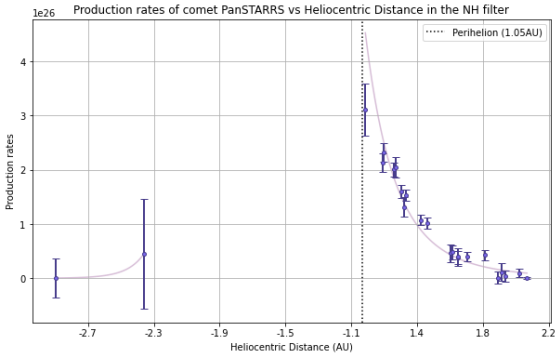

(d) Gas production rates of NH with respect to heliocentric distance

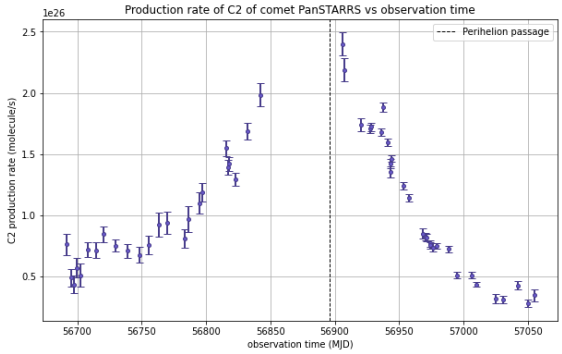

(e) Gas production rates of C_2 with respect to observation time

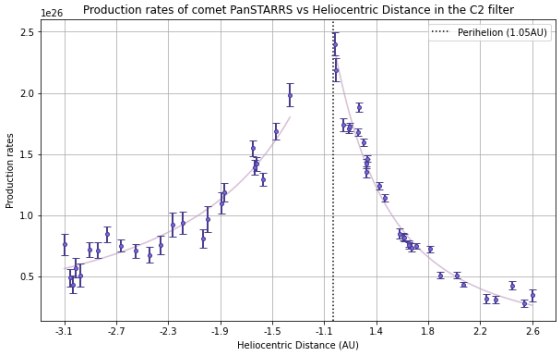

(f) Gas production rates of C_2 with respect to heliocentric distance

Figure 5.1: Evolution of the CN, NH and C_2 production rates in the coma of comet PanSTARRS as a function of time (left) and heliocentric distance (right)

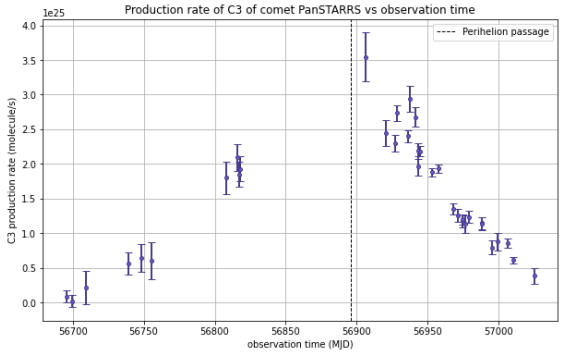

(a) Gas production rates of C_3 with respect to observation time

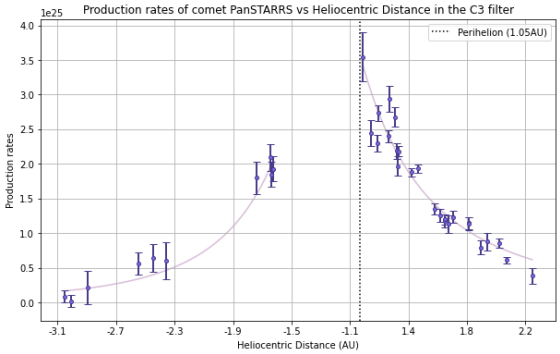

(b) Gas production rates of C_3 with respect to heliocentric distance

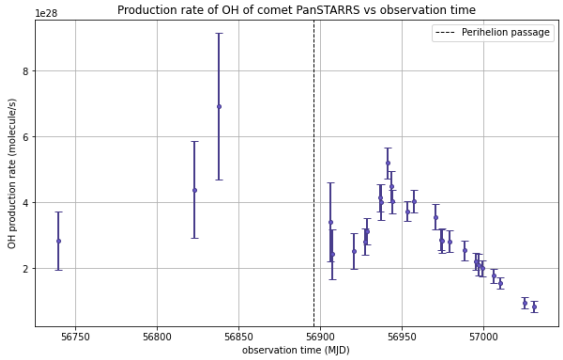

(c) Gas production rates of OH with respect to observation time

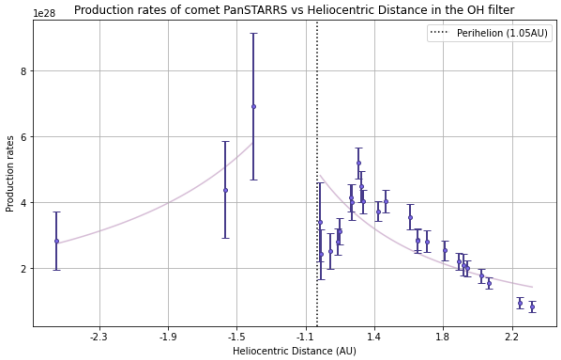

(d) Gas production rates of OH with respect to heliocentric distance

Figure 5.2: Evolution of the C_3 and OH production rates in the coma of comet PanSTARRS as a function of time (left) and heliocentric distance (right)

Gas production rate: Lovejoy

The production rates of comet Lovejoy as a function of time and heliocentric distance are given in Figures 5.3 and 5.5. These rates were also fitted with a power-law, and the resulting slopes are provided in the Table 5.3.
Once again, the behavior is consistent for every gas filter: the production rate increases as the comet approaches perihelion and decreases afterward. Unlike PanSTARRS however, the evolution of Lovejoy's production rate does not display any noticeable emission peak outside of the perihelion.
The pre-perihelion slopes tend to be slightly steeper than those post-perihelion. For example, in the NH filter, the slope before perihelion is -4.33 ± 0.26, compared to only -3.12 ± 0.51 after perihelion.

Filter	r_h-dependence before perihelion passage	r_h-dependence after perihelion passage
OH	-3.90 ± 0.26	-2.92 ± 0.19
NH	-4.33 ± 0.35	-3.12 ± 0.51
CN	-2.46 ± 0.07	-2.15 ± 0.05
C_3	-2.94 ± 0.13	-2.47 ± 0.14
C_2	-3.66 ± 0.08	-2.92 ± 0.07

Table 5.3: Fitted power-law slopes of the r_h-dependence of the OH, NH, CN, C_3 and C_2 production rates of comet Lovejoy, before and after perihelion passage.

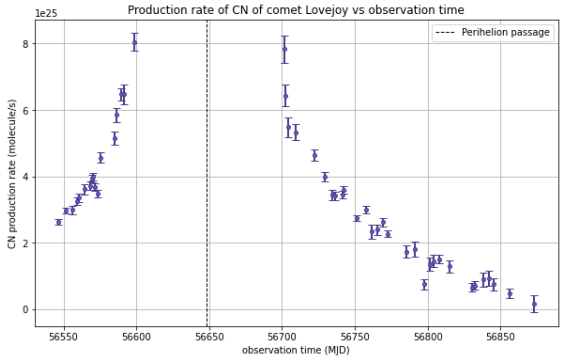

(a) Gas production rates of CN with respect to observation time

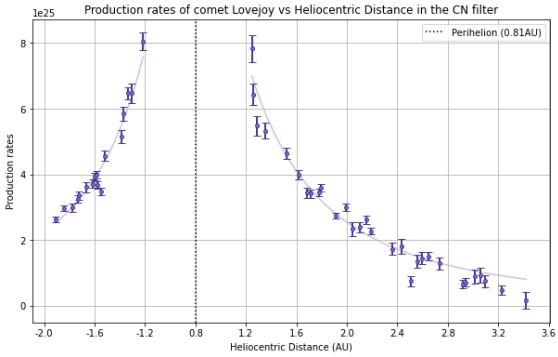

(b) Gas production rates of CN with respect to heliocentric distance

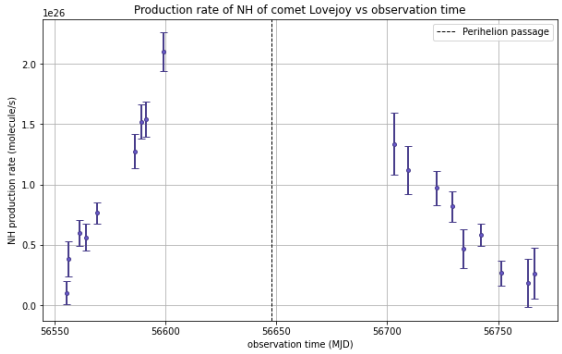

(c) Gas production rates of NH with respect to observation time

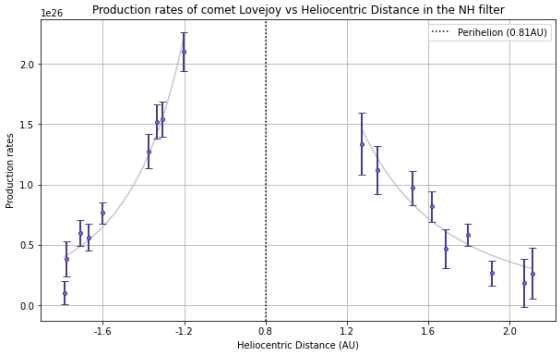

(d) Gas production rates of NH with respect to heliocentric distance

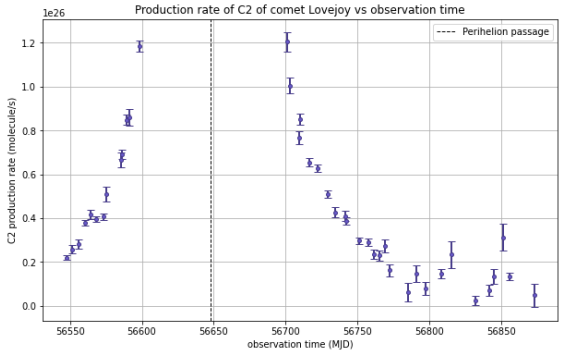

(e) Gas production rates of C_2 with respect to observation time

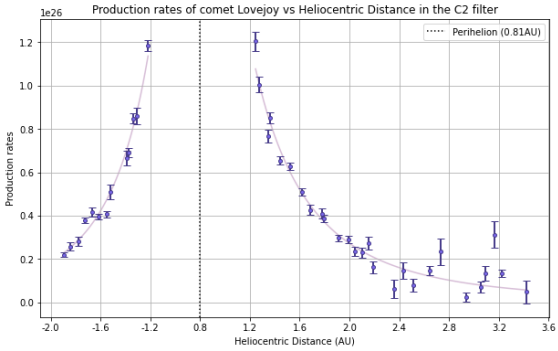

(f) Gas production rates of C_2 with respect to heliocentric distance

Figure 5.3: Evolution of the CN, NH and C_2 production rates in the coma of comet Lovejoy as a function of time (left) and heliocentric distance (right)

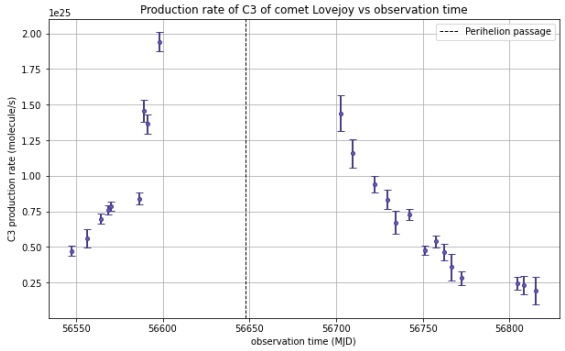

(a) Gas production rates of C_3 with respect to observation time

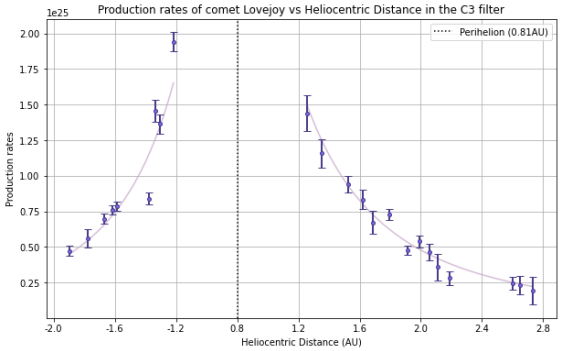

(b) Gas production rates of C_3 with respect to heliocentric distance

Figure 5.4: Evolution of the C_3 production rate in the coma of comet Lovejoy as a function of time (left) and heliocentric distance (right)

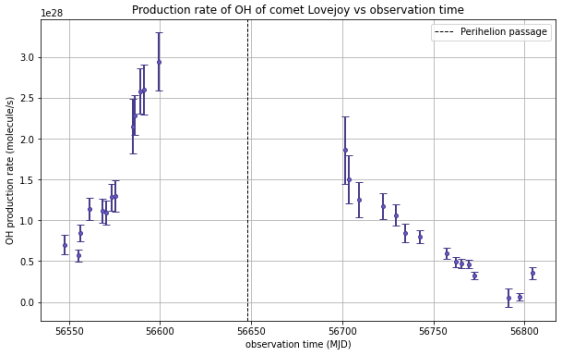

(a) Gas production rates of OH with respect to observation time

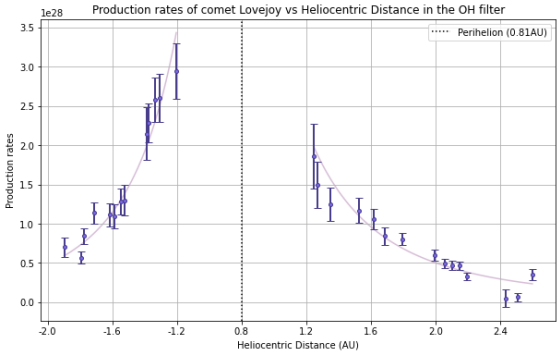

(b) Gas production rates of OH with respect to heliocentric distance

Figure 5.5: Evolution of the C_3 and OH production rates in the coma of comet Lovejoy as a function of time (left) and heliocentric distance (right)

5.4.2 Gas production ratios and comet taxonomy

Comets are categorized depending on their ratios of gas abundance. The interrelationship of abundance ratios allows for comets to be separated into two categories: typical comets and carbon-depleted comets.

The abundance ratio $\log(C_2/CN)$ of typical comets according to [14] ranges between -0.09 and 0.29, with a mean of 0.06. Depleted comets, on the other hand, have a $\log(C_2/CN)$ ratio that ranges from -1.22 to -0.21 with a mean at -0.61. This factor is used as the discriminating factor for cometary taxonomy.

In this section, we study the abundance ratio of C_2 production rates compared to that of CN in order to infer the cometary taxonomy of Lovejoy and PanSTARRS, as well as the abundance ratios of C_3 and OH production rates compared to CN for additional insight into the behavior of the comae.

PanSTARRS

The abundance ratio $\log(Q_{C_2}/Q_{CN})$ of comet PanSTARRS is displayed in Figures 5.6a and 5.6b. The pink and blue zones represent the possible ranges of the abundance ratio for a typical and a depleted comet, respectively. Nearly all values are firmly within the range of a typical comet, with only three data points above it and no data points in the depleted zone, for an average of 0.16 ± 0.01. We therefore conclude that PanSTARRS is a typical comet in terms of carbon production.

Moreover, the ratio appears to decrease with heliocentric distance, so the production of C_2 increases as the comet approaches the Sun faster than the production of CN does. A slight increase in the ratio is also observed around 2.3 AU. However, this is likely not a physical effect but rather an artifact due to low SNR in that region.

On the other hand, the abundance ratio $\log(Q_{C_3}/Q_{CN})$, displayed in Figures 5.6c and 5.6d, has an average of -0.74 ± 0.06 and is mostly constant, but also seems to decrease a bit with heliocentric distance. This trend could suggest that the parent molecule of C_3 stops sublimating at that distance, leading to a decline in C_3 production relative to CN.

Finally, the abundance ratio $\log(Q_{OH}/Q_{CN})$ in Figures 5.6e and 5.6f shows an interesting behavior: the OH seems to drop after the perihelion passage, only to rise again, reaching a peak at 56698 MJD (at 3.0 AU) before declining once more. Overall, the average value of the ratio is 2.62 ± 0.02. This behavior was already noticed in Figure 5.2c: it corresponds to the OH production peak. This feature appears only in the OH/CN abundance ratio, indicating that the increase in OH production was significantly stronger than that of CN. In contrast, the absence of similar features in the abundance ratios $\log(Q_{C_2}/Q_{CN})$ and $\log(Q_{C_3}/Q_{CN})$ means that the peaks in productions of C_2, C_3 and CN at that time all had similar intensities.

Therefore, around 56698 MJD, PanSTARRS had a temporary outburst of C_2, C_3, OH and CN, with OH being produced in comparatively greater amounts than the other species.

Lovejoy

The abundance ratio $\log(Q_{C_2}/Q_{CN})$ of comet Lovejoy is displayed in Figures 5.7a and 5.7b. Again, the pink and blue zones represent, respectively, the possible ranges of the abundance ratio for a typical and a depleted comet. Similarly to PanSTARRS, nearly all data points are firmly within the range of a typical comet, with only two data points in the depleted zone and only four points outside both zones. The average value of the C_2-to-CN ratio is 0.05 ± 0.03. We therefore conclude that Lovejoy is a typical comet in terms of carbon production.

Continuing with the similarities to PanSTARRS, Lovejoy also displays the anticorrelation between the C_2-to-CN ratio and heliocentric distance, as well as an increase in the "far" heliocentric distances, starting at 2.3 AU. The C_3-to-CN ratio has an average of -0.73 ± 0.02 and is displayed in Figures 5.7c and 5.7d. As with PanSTARRS, we see an increase of the ratio as the heliocentric distance decreases.

Finally, the OH-to-CN ratio has an average of 2.36 ± 0.04 and is shown in Figures 5.7e and 5.7f. Interestingly, it seems to have slightly higher values before perihelion than after it, but not enough data is present to properly define a trend.

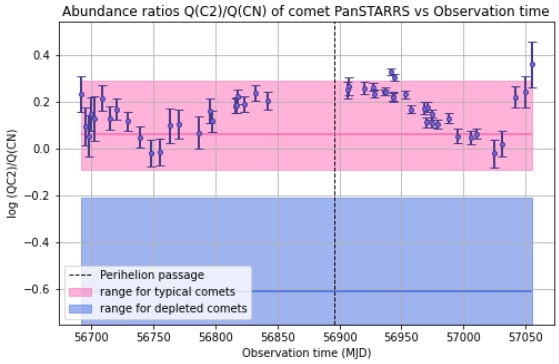

(a) Abundance ratio C_2/CN with respect to time

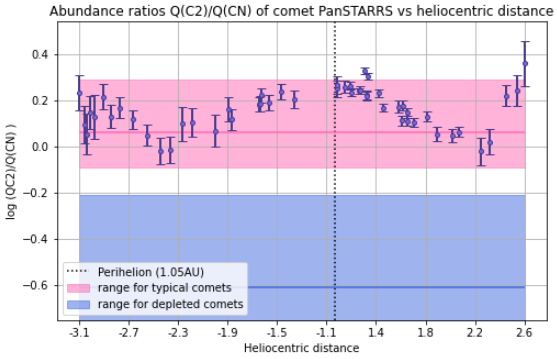

(b) Abundance ratio C_2/CN with respect to heliocentric distance

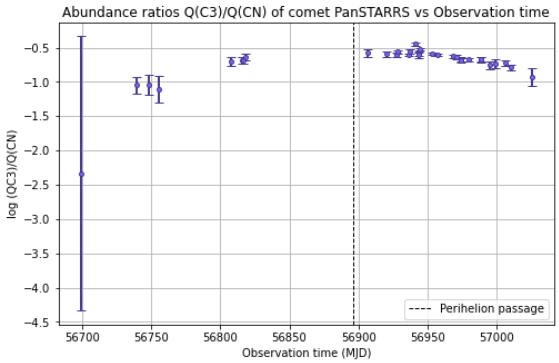

(c) Abundance ratio C_3/CN with respect to time

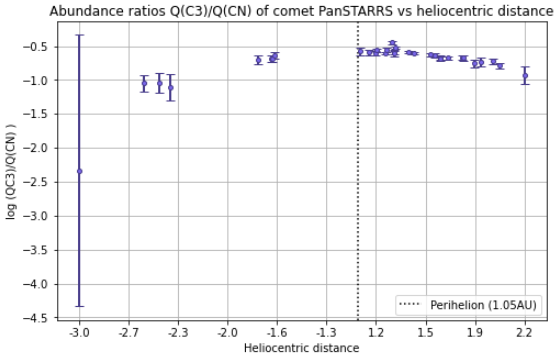

(d) Abundance ratio C_3/CN with respect to heliocentric distance

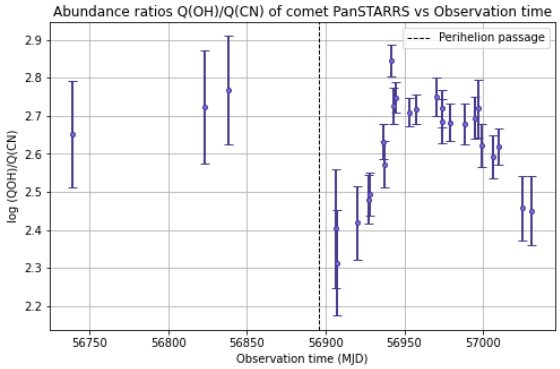

(e) Abundance ratio OH/CN with respect to time

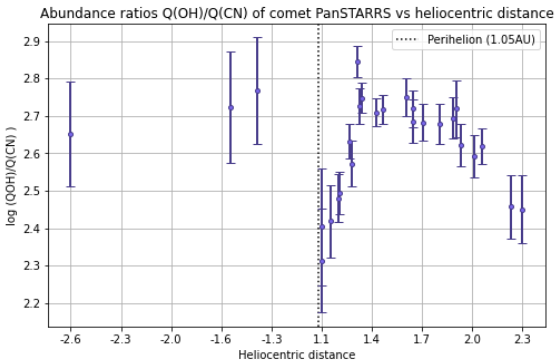

(f) Abundance ratio OH/CN with respect to heliocentric distance

Figure 5.6: Abundance ratioes of C_2, C_3 and OH to CN of PanSTARRS, with respect to time (left) and heliocentric distance (right).

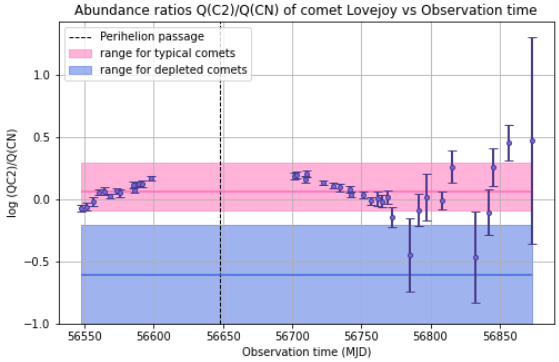

(a) Abundance ratio C_2/CN with respect to time

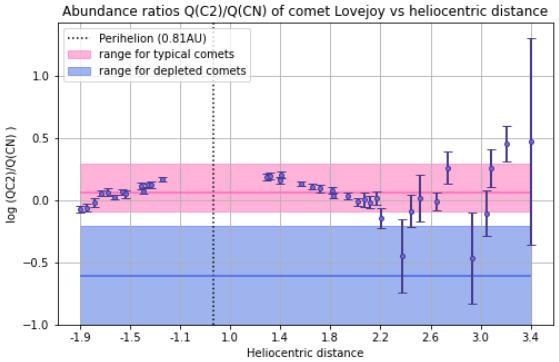

(b) Abundance ratio C_2/CN with respect to heliocentric distance

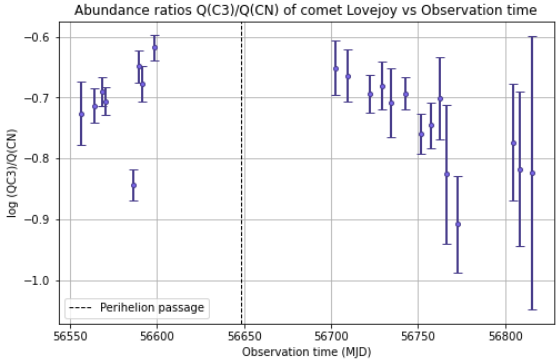

(c) Abundance ratio C_3/CN with respect to time

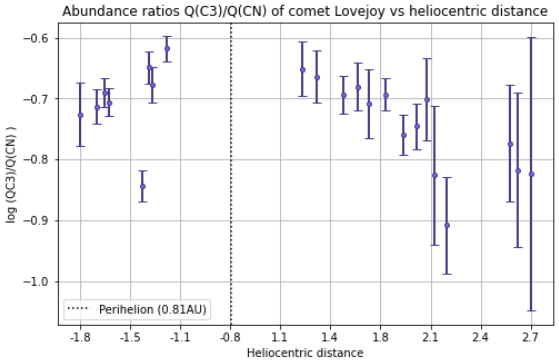

(d) Abundance ratio C_3/CN with respect to heliocentric distance

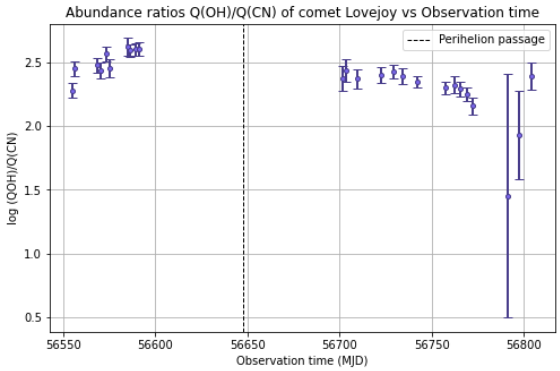

(e) Abundance ratio OH/CN with respect to time

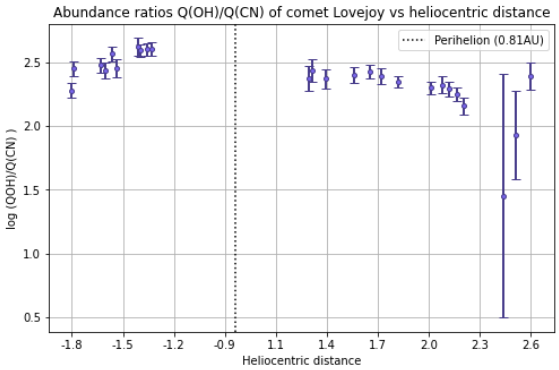

(f) Abundance ratio OH/CN with respect to heliocentric distance

Figure 5.7: Abundance ratioes of C_2, C_3 and OH to CN of Lovejoy, with respect to time (left) and heliocentric distance (right).

5.4.3 Water production rate

Water production is connected to OH production by the following formula [40]:

$$Q_{H_2O} = 1.361 \cdot r_H^{-0.5} \cdot Q_{OH}. \tag{5.18}$$

Using this formula and our previous results regarding the production rate of OH in section 5.4.1 allows for inference of the evolution of the production rate of water with respect to time and heliocentric distance.

Water production rate of PanSTARRS

The evolution of the water production rate of comet PanSTARRS with respect to time and heliocentric distance is presented in Figure 5.8. The evolution of these production rates was also fitted with a power-law, and the resulting slopes are listed in Table 5.4.

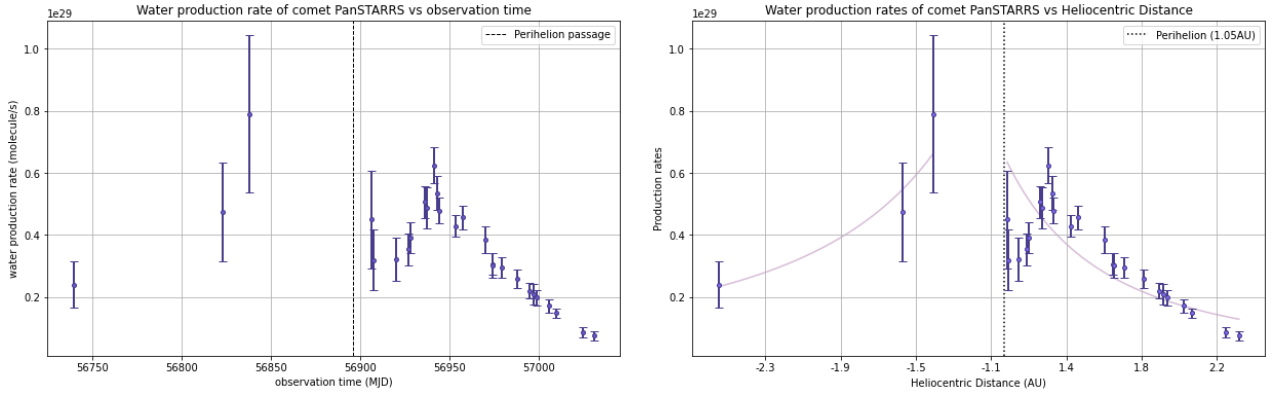

(a) Water production rates with respect to observation time

(b) Water production rates with respect to heliocentric distance

Figure 5.8: Evolution of the water production rates in the coma of comet PanSTARRS as a function of time (left) and heliocentric distance (right)

Filter	r_h-dependence before perihelion passage	r_h-dependence after perihelion passage
Water	Not enough data	-2.09 ± 0.11

Table 5.4: Fitted power-law slopes of the r_h-dependence of the water production rates of comet PanSTARRS, before and after perihelion passage.

Water production rate of Lovejoy

The evolution of the water production rate of comet Lovejoy with respect to time and heliocentric distance is presented in Figure 5.9. The evolution of these production rates was also fitted with a power-law, and the resulting slopes are listed in Table 5.5.

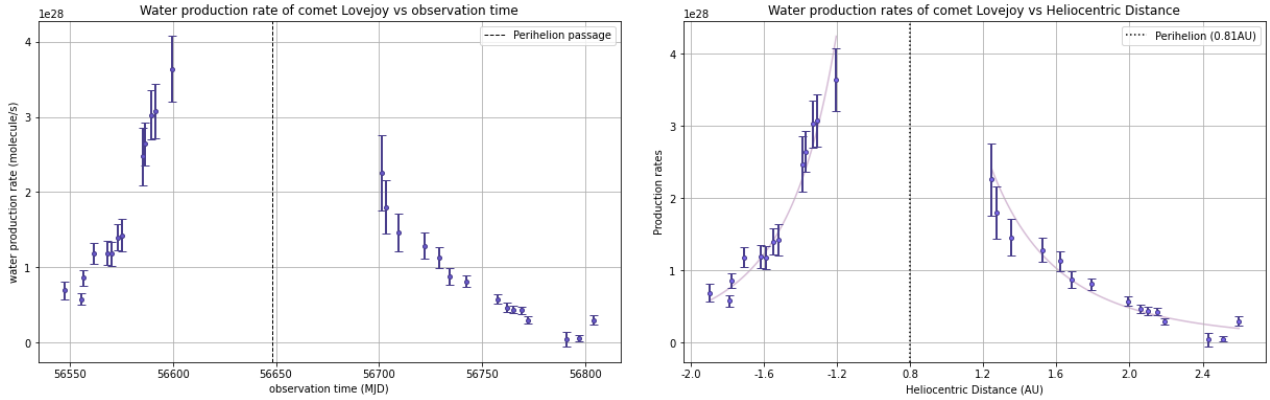

(a) Water production rates with respect to observation time

(b) Water production rates with respect to heliocentric distance

Figure 5.9: Evolution of the water production rates in the coma of comet Lovejoy as a function of time (left) and heliocentric distance (right)

Filter	r_h-dependence before perihelion passage	r_h-dependence after perihelion passage
Water	-4.40 ± 0.26	-3.42 ± 0.20

Table 5.5: Fitted power-law slopes of the r_h-dependence of the water production rate of comet Lovejoy, before and after perihelion passage.

Chapter 6

Dust activity

In addition to gases, comets eject significant amounts of dust. Dust grains are ejected along the gas when the parent molecules are ejected from the nucleus, and become part of the coma. This section focuses on an estimation of the dust production rates of the observed comets.

The quantification of dust activity is realized through the computation of the so-called *Afρ parameter*. This chapter begins with an introduction to the parameter, followed by a presentation of the results.

6.1 Definition: the Afρ parameter

The $Af\rho$ is a quantity that gives an indication of cometary dust activity. It was introduced for the first time in 1984 by A'Hearn et al [41]. It is the product of three different quantities:

- $A(\theta)$, the Bond albedo of cometary dust grains. This is the fraction of incident light that is reflected by dust grains at phase angle θ, θ being the Sun-object-observer angle. It is a value between 0 and 1, 0 corresponding to a black body and 1 to a perfect mirror.
- f, the filling factor. f is the total area filled with dust grains in the field of view (i.e: the number of grains multiplied by their cross-section), divided by the surface of the field of view, $\pi\rho^2$.
- ρ, the radius of the coma, assumed to be circular, within which the dust activity is measured.

In practice, it is not possible to compute these three quantities separately. The filling factor in particular would include counting the number of grains by hand. We can, however, compute their product. The resulting value is called the $Af\rho$ parameter. It follows the following formula:

$$A(\theta)f\rho = \frac{2r_H^2\Delta}{\rho}\frac{F_{comet}}{F_{sun}} \tag{6.1}$$

In this relation, ρ is the radius (in centimeters) inside which the cometary flux F_{comet} is measured. Δ is the geocentric distance to the comet (also in cm), and r_H is the heliocentric distance (in AU). F_{comet} is the solar flux reflected in the field of view by the dust grains present within the nucleocentric sphere of radius ρ and F_{sun} represents the solar flux at 1 AU. Both fluxes depend on the used filter and are expressed in $erg \cdot cm^{-2} \cdot s^{-1} \cdot \text{Å}^{-1}$. The quantity $Af\rho$ is thus expressed in cm. The $Af\rho$ has the advantage of being theoretically independent of distance to the nuclei, and thus the size of the aperture, as long as the radial profile is inversely proportional to ρ. This behavior is illustrated in Figure 6.1, where the $Af\rho$ value stabilizes and becomes approximately constant beyond a distance of 10^4 km from the nucleus (dashed line).

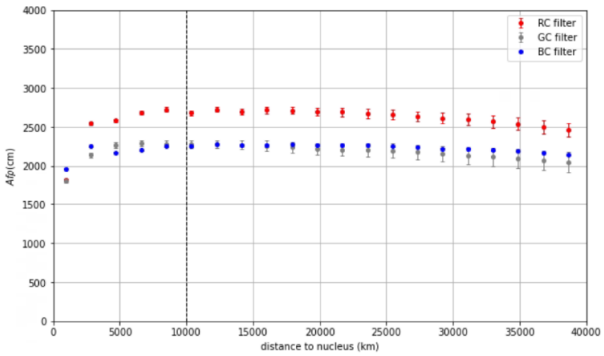

Figure 6.1: Profile of the $Af\rho$ parameter of comet PanSTARRS as a function of distance from the nucleus, measured on the night of March 22nd, 2014 in the RC, GC and BC filters.

There are many assumptions in using $Af\rho$ as a measure of dust production. Since the scattering function of grains is expected to be strongly peaked in the direction of forward scattering and less so in the direction of backward scattering, it should also be expected for the relation between the $AF\rho$ and actual dust production to vary significantly with phase angle. It is also assumed that the contribution of reflected light by the nucleus is negligible. Finally, for many size distributions, the scattered optical light comes largely from grains with sizes similar to the observed wavelength [42]. Therefore, the extrapolation $Af\rho$ => total production of dust assumes that the size distribution and the physical nature of the particles remain the same both with time and from one comet to another. The $Af\rho$ can be used as a proxy for dust production, but its limitations must be kept in mind.

If the grains in the coma are gray, then $Af\rho$ will be the same across all filters. Any variation of $Af\rho$ concerning filter type represents the spectral reflectivity of the grains.

6.2 The phase angle effect

As said before, the albedo and therefore the $Af\rho$ depend on the phase angle, as the part of the comet illuminated by the Sun must be oriented towards Earth for the observer to see the

reflected light. In particular, the scattering is much more efficient if θ is large. This is known as the phase angle effect, and a correction is needed to account for it. This correction consists of a normalization of the obtained values by a dust phase function. We use a composite dust phase function defined by D. Schleicher [33]. This function is a combination of two previously defined functions: the Halley curve, which is better suited for small phase angles, and the Marcus curve, which is more suited for large phase angles. We chose to normalize the $Af\rho$ values at a phase angle θ of 0° (corresponding to a back-scattering of the light).

A pair of plots showing the curve in linear and in log space is provided in 6.2.

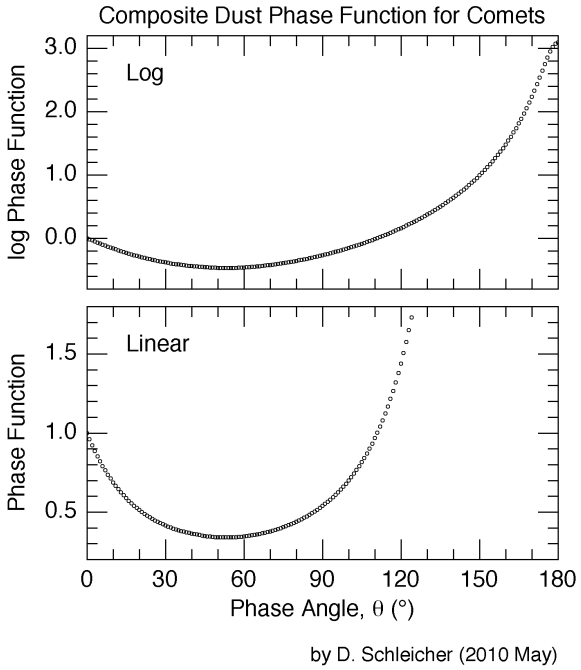

Figure 6.2: Zero-degree-normalized composite dust phase function defined by D. Schleicher and used in this work to correct the obtained $Af\rho$ values for the phase angle effect

6.3 Computation methods

The $Af\rho$ parameter was computed numerically using equation 6.1. For each image obtained in the R, RC, BC and GC filters, an $Af\rho$ value was computed for each annulus of pixels around the comet's center. This way, a profile for the $Af\rho$ as a function of the nucleocentric distance ρ was obtained. An interpolation was then performed on this profile to deduce the $Af\rho$ at a nucleocentric distance of 10000 km.

These values are then normalized to account for the phase angle effect. For this purpose, the Sun-target-observer angle at the time of image generation is retrieved for every image

using the JPL Horizon website [28]. The function provided by D. Schleicher only works for discrete angle values, so an interpolation of the function is to account for non-discrete angle values (i.e., angles with decimals).

Finally, the phase-angle-corrected values are all gathered and plotted to follow their evolution as a function of time.

6.4 Results and discussion: dust activity

In this section, we present the evolution of the $Af\rho$ parameter as a function of observation time and heliocentric distance.

Dust activity of PanSTARRS

The evolution of the $Af\rho$ parameter of comet PanSTARRS with respect to time and heliocentric distance is given in Figures 6.3 and 6.4, respectively. The evolution of the dust activity with respect to heliocentric distance was also fitted with a power-law, and the resulting slopes are listed in Table 6.1.

Across all filters, the behavior of $Af\rho$ displays a strong asymmetry around perihelion. Before perihelion passage, the curve remains almost flat across all filters. After perihelion passage however, the $Af\rho$ drops sharply, with a significantly steeper slope in the fitted power law (see Table 6.1), indicating a much stronger dependence on heliocentric distance.

This asymmetric pattern, characterized by a slow increase in $Af\rho$ before perihelion and a sharp decline after, have been previously observed in DNCs [31]. In contrast, LPCs typically exhibit a more rapid increase in activity approaching perihelion [43]. This sharp drop could be explained by a change in the illumination of active regions on the nucleus. As the comet approaches and passes perihelion, the angle at which sunlight illuminates these active areas may change abruptly, causing a rapid decline in observed dust activity. Lastly, the peak in gas production rate observed in Section 5.4.1 is not reflected in the dust activity, suggesting the event was a gas-only outburst.

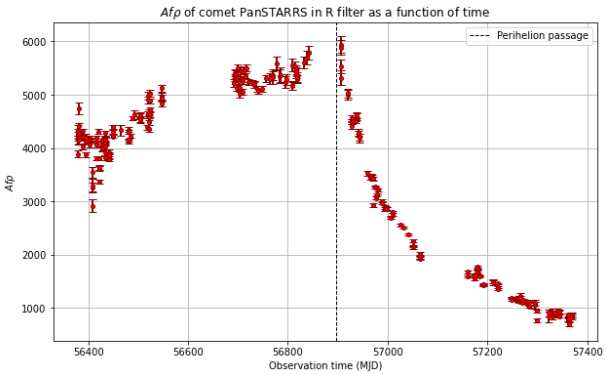

(a) R filter

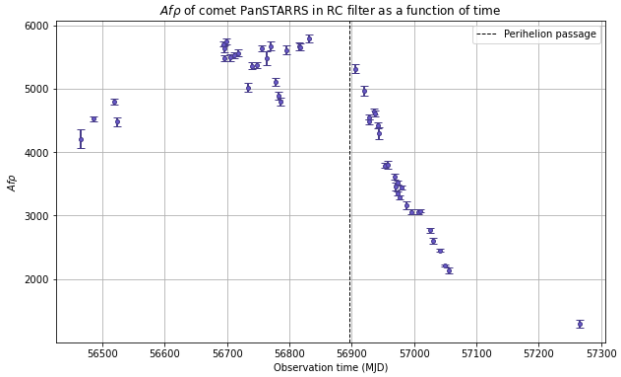

(b) RC filter

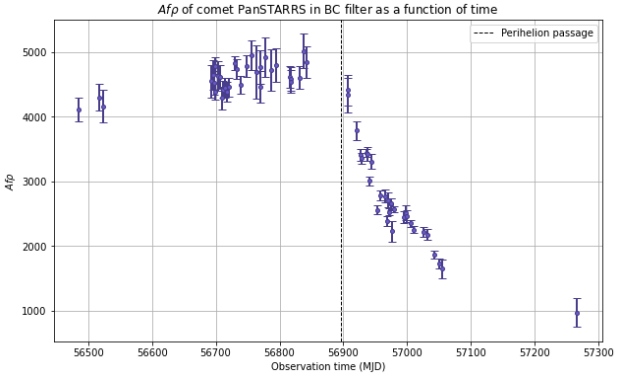

(c) BC filter

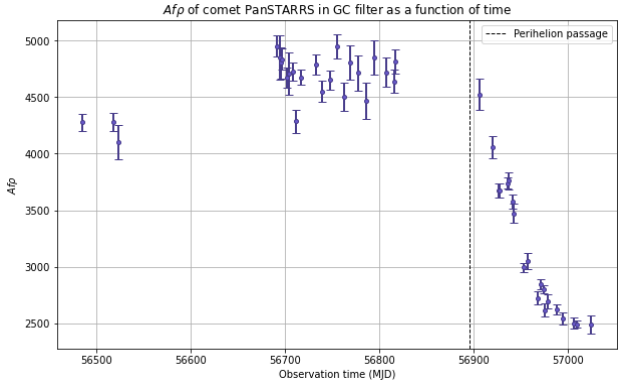

(d) GC filter

Figure 6.3: Evolution of the $Af\rho$ parameter of comet PanSTARRS with respect to time

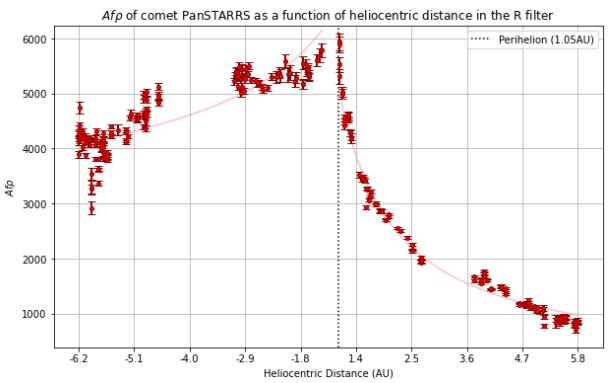

(a) R filter

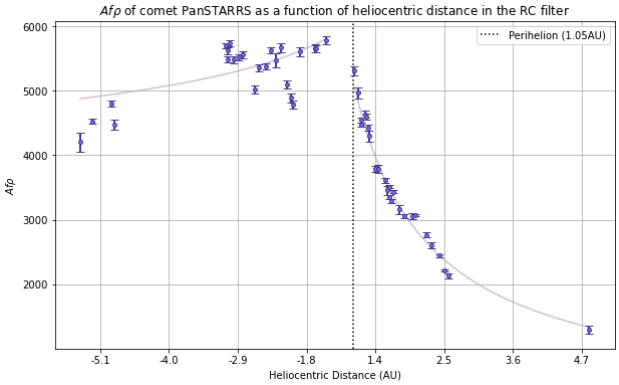

(b) RC filter

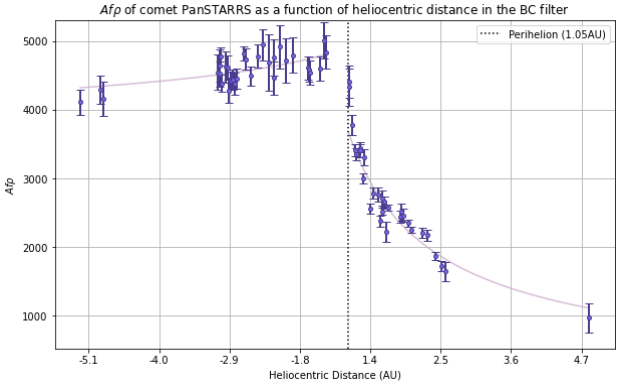

(c) BC filter

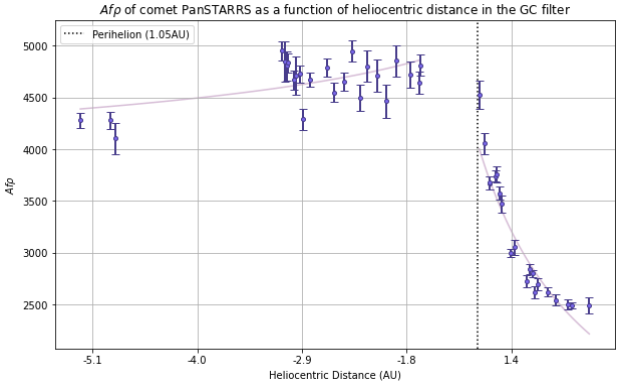

(d) GC filter

Figure 6.4: Evolution of the $Af\rho$ parameter of comet PanSTARRS with respect to heliocentric distance. Data taken before perihelion passage is on the right side of the graph, and data taken after is on the left side.

Filter	r_h-dependence before perihelion passage	r_h-dependence after perihelion passage
R	-0.270 ± 0.003	-0.970 ± 0.002
RC	-0.134 ± 0.006	-0.885 ± 0.008
BC	-0.081 ± 0.024	-0.789 ± 0.025
GC	-0.089 ± 0.015	-0.805 ± 0.021

Table 6.1: Fitted power-law slopes of the r_h-dependence of the $Af\rho$ of comet PanSTARRS, before and after perihelion passage.

Dust activity of Lovejoy

The evolution of the $Af\rho$ parameter of comet Lovejoy with respect to time and heliocentric distance is given in Figures 6.5 and 6.6, respectively. The evolution of the dust activity was also fitted with a power-law, and the resulting slopes are listed in Table 6.2.

Similarly to the case of PanSTARRS, the behavior of the $Af\rho$ parameter does not vary significantly from one filter to another. The dust activity increases as the comet approaches the Sun, then decreases as it moves away. However, in contrast to PanSTARRS, the behavior of the $Af\rho$ is also similar before and after perihelion passage, or at least from what can be inferred from the sparse pre-perihelion data. Averaging the power-law parameters across all filters of Table 6.2 yields -3.58 ± 0.04 before perihelion, compared to a slightly smaller value of -3.06 ± 0.01 post-perihelion. The dust activity therefore increased faster than it decreased, as was the case with Lovejoy's magnitude. The power-law slopes of Lovejoy are in general much steeper than PanSTARRS, indicating that Lovejoy's dust activity is much more variable than that of its DNC counterpart.

On the other hand, the feature observed at 56800 MJD in Figure 4.9 is nowhere to be seen. This suggests that this peak was nothing but an angle-related geometric effect, which thus disappears once the dust activity is normalized to account for this effect.

Filter	r_h-dependence before perihelion passage	r_h-dependence after perihelion passage
R	-3.74 ± 0.03	-3.04 ± 0.01
RC	-3.56 ± 0.05	-3.17 ± 0.03
BC	-3.73 ± 0.12	-3.04 ± 0.04
GC	-3.31 ± 0.08	-3.00 ± 0.03

Table 6.2: Fitted power-law slopes of the r_h-dependence of the $Af\rho$ of comet Lovejoy, before and after perihelion passage.

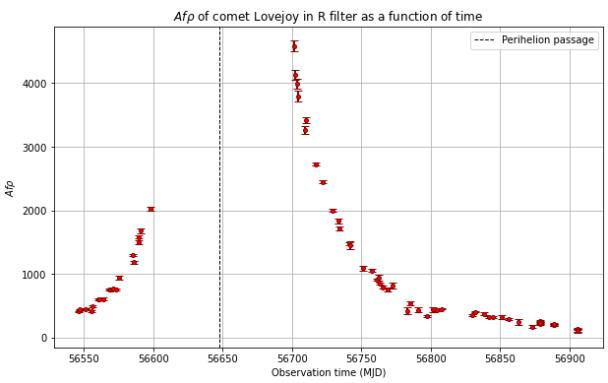

(a) R filter

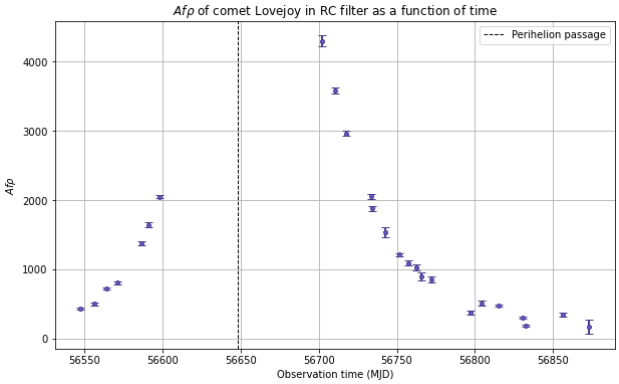

(b) RC filter

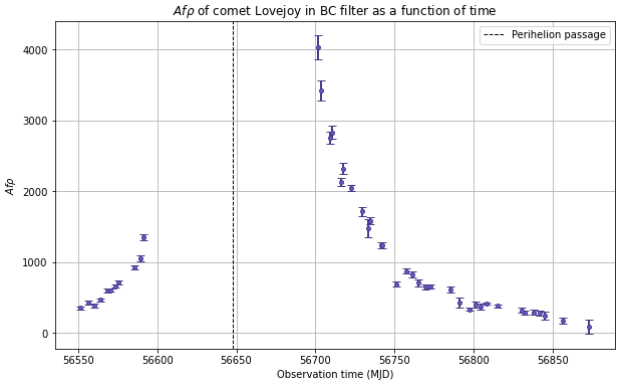

(c) BC filter

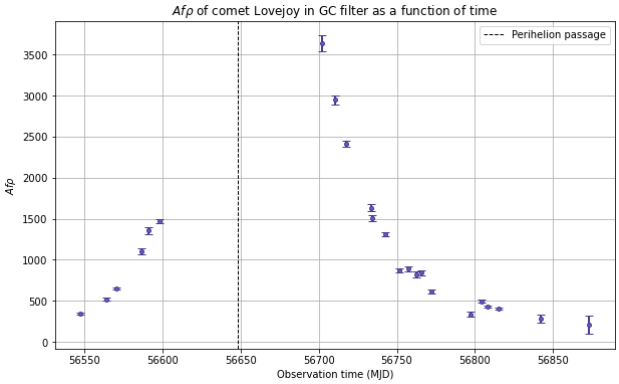

(d) GC filter

Figure 6.5: Evolution of the $Af\rho$ parameter of comet Lovejoy with respect to time

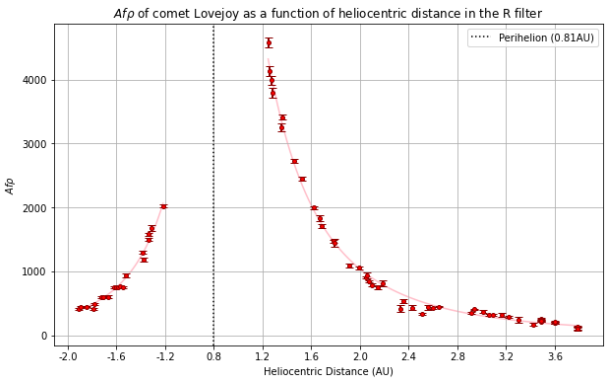

(a) R filter

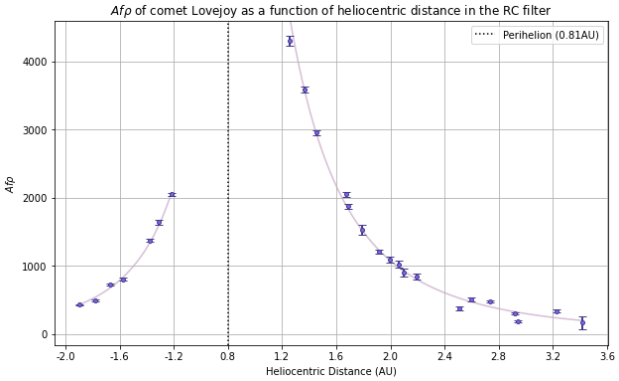

(b) RC filter

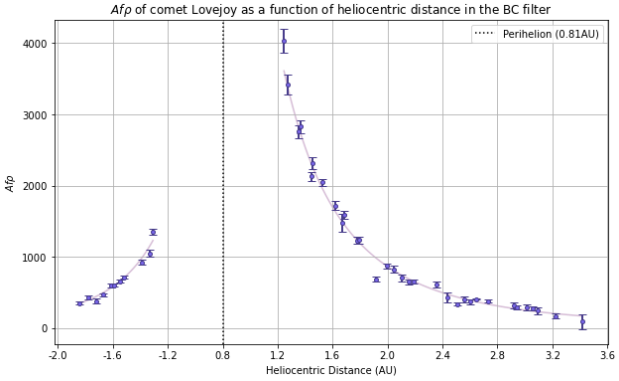

(c) BC filter

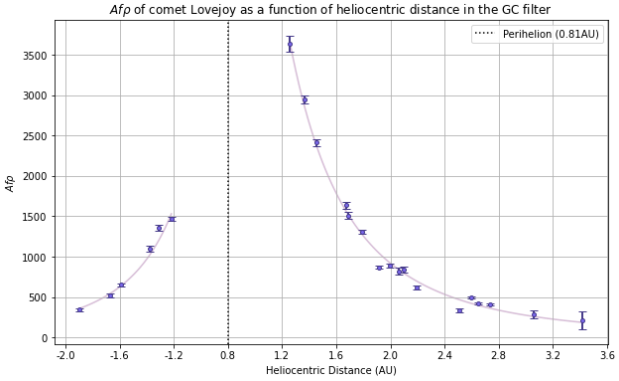

(d) GC filter

Figure 6.6: Evolution of the $Af\rho$ parameter of comet Lovejoy with respect to heliocentric distance. Data taken before perihelion passage is on the right side of the graph, and data taken after is on the left side.

6.5 Dust-to-gas ratios

This section compares the gas activity obtained in Chapter 5 with the dust activity discussed in the previous section. Such a comparison is a straightforward way to assess if a comet is dust-rich or gas-rich. For this purpose, the dust-to-gas ratio with respect to Julian time and heliocentric distance was computed.
The dust-to-gas ratio is the logarithmic ratio between the $Af\rho$ values measured in the R and RC filters, and the production rate of CN and water, the latter being computed by applying the transformation applied in Section 5.4.3 to the production rate of OH. Water serves as a reliable proxy for total cometary gas emission, while CN is one of the brightest and most easily detectable gas species in optical observations.
Below is displayed the evolution of the dust-to-gas ratio for comets PanSTARRS and Lovejoy.

Dust-to-gas ratios of PanSTARRS

The evolutions of the dust-to-gas ratios of comet PanSTARRS are given in Figures 6.7 and 6.8, which respectively compare the evolution of the $Af\rho$ parameter to the CN and water production rates. In both cases, the $Af\rho$ is calculated using both the R and RC filters, and its evolution is presented as a function of both time and heliocentric distance.

In the case of CN, the evolution of the dust-to-gas ratio is essentially identical whether the R or RC filter is used. In both cases, the ratio decreases as the comet approaches the Sun, reaching a minimum at perihelion. The ratio then increases again as the comet moves away from the Sun in a relatively symmetrical manner. This behavior could be explained by the different dynamics of gas and dust: Far from the Sun, outgassing decreases and the CN dissipates away. In contrast, the dust can stay closer to the nucleus as it not as strongly pushed away by the solar radiation pressure as it was at shorter heliocentric distances. This favors more dust in the aperture relative to CN at far distances. As a result, the observed CN production rises and falls more rapidly than that of dust.

The dust-to-water ratio, on the other hand, shows a more puzzling trend. Due to the lack of pre-perihelion data, no conclusion can be drawn about its early behavior. However, post-perihelion, the ratio decreases and reaches a minimum value at 56941 MJD at a distance of 1.286 AU of -25.16 ± 0.04 in the R filter and -25.15 ± 0.04 in the RC filter. It then increases again. This dip coincides with the water outburst observed at that time (see Figure 5.8). Since the gas production increases sharply while the dust does not, the effect on the dust-to-gas ratio appears as a dip rather than a peak. This further confirms that this outburst in gas production is not accompanied by a corresponding increase in dust activity.

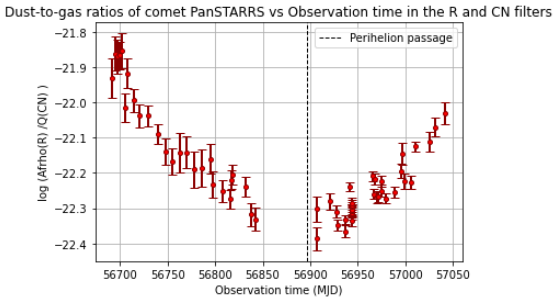

(a) dust-to-gas ratio in the R and CN filters, with respect to observation time

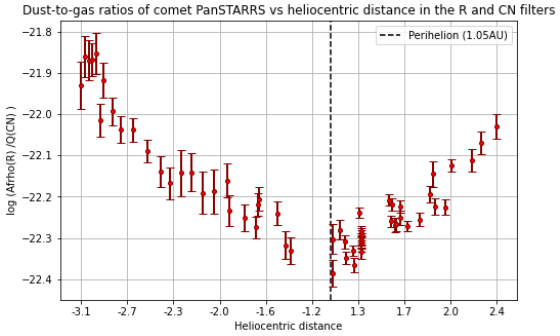

(b) dust-to-gas ratio in the R and CN filters, with respect to heliocentric distance

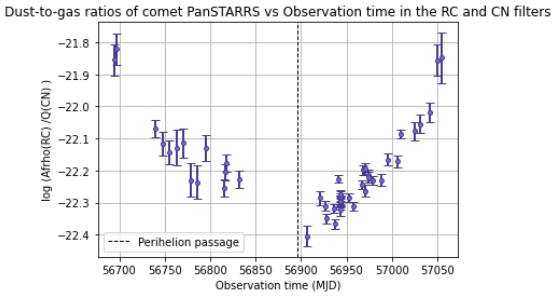

(c) dust-to-gas ratio in the RC and CN filters, with respect to observation time

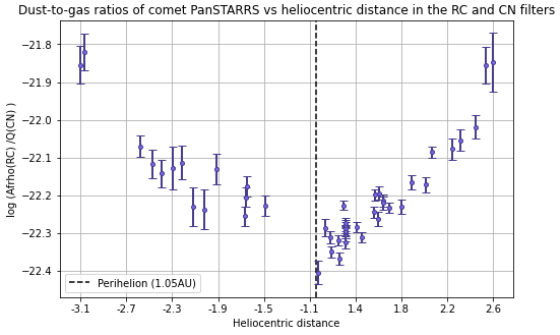

(d) dust-to-gas ratio in the RC and CN filters, with respect to heliocentric distance

Figure 6.7: Dust-to-gas ratios of comet PanSTARRS. The $Af\rho$ parameter is expressed in the R and RC filters, and the gas production is expressed in the CN filter. The ratios are expressed with respect to observation time (left) and heliocentric distance (right).

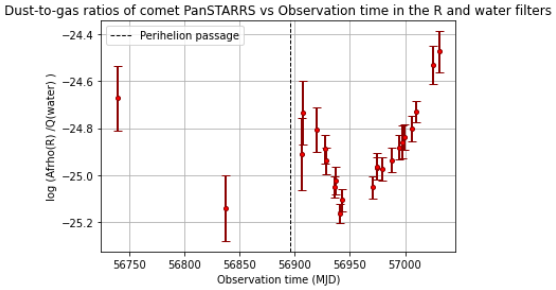

(a) dust-to-gas ratio in the R filter and water production rate, with respect to observation time

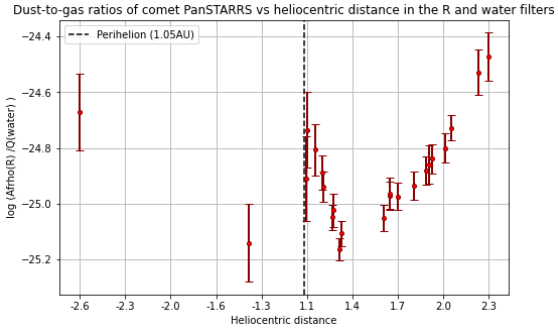

(b) dust-to-gas ratio in the R filter and water production rate, with respect to heliocentric distance

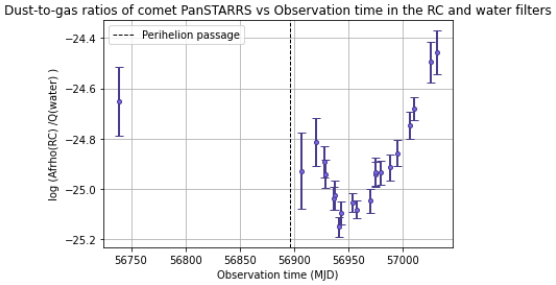

(c) dust-to-gas ratio in the RC filter and water production rate, with respect to observation time

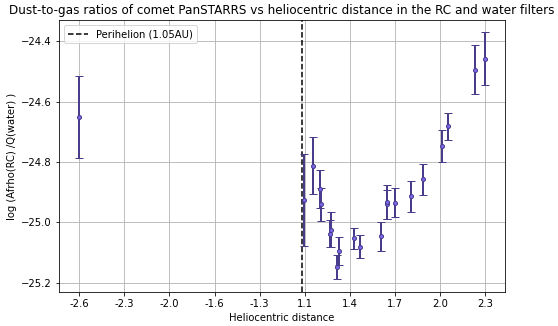

(d) dust-to-gas ratio in the RC and water production rate, with respect to heliocentric distance

Figure 6.8: Dust-to-gas ratios of comet PanSTARRS. The $Af\rho$ parameter is expressed in the R and RC filters, and the water production rate inferred from the OH filter. The ratios are expressed with respect to observation time (left) and heliocentric distance (right).

Dust-to-gas ratio of Lovejoy

The evolution of the dust-to-gas ratio of comet Lovejoy is given in Figures 6.9 and 6.10, corresponding respectively to the evolution of the $Af\rho$ compared to CN and water production rates. In both cases, the $Af\rho$ is expressed using both the R and RC filters, and its evolution is shown with respect to time as well as heliocentric distance.

The dust-to-CN ratio displays the same behavior in every $Af\rho$ filter. Before perihelion, the ratio increases as the comet approaches the Sun, indicating that the dust production rises more rapidly than CN production. This is the opposite of what was observed for comet PanSTARRS, where CN increased more steeply than dust. Overall, the dust-to-CN ratio is higher after perihelion than before. After perihelion, the ratio decreases and reaches a minimum around 56760 MJD, at a heliocentric distance of 2.1 AU, before appearing to rise again.

In contrast, the $Af\rho$-to-water production ratio appears constant, but its average value differs before and after perihelion. Specifically, the post-perihelion values are systematically higher, suggesting that the comet was dustier after perihelion than before.

This asymmetry in the production rate is likely related to seasonal effects, as is the asymmetry in the light curve seen in Section 4.3. As the comet approached the Sun, the latter illuminated a dust-rich region of the nucleus, resulting in increased dust emission. This implies a heterogeneous nucleus, with certain regions more prone to releasing dust than others. The precise mechanism driving this asymmetric behavior, however, remains uncertain.

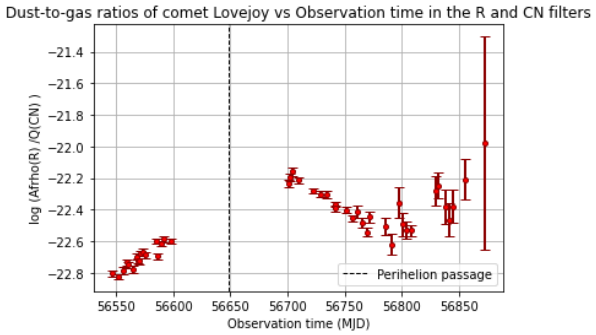

(a) dust-to-gas ratio in the R and CN filters, with respect to observation time

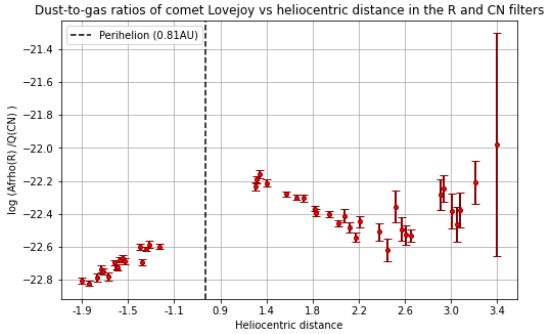

(b) dust-to-gas ratio in the R and CN filters, with respect to heliocentric distance

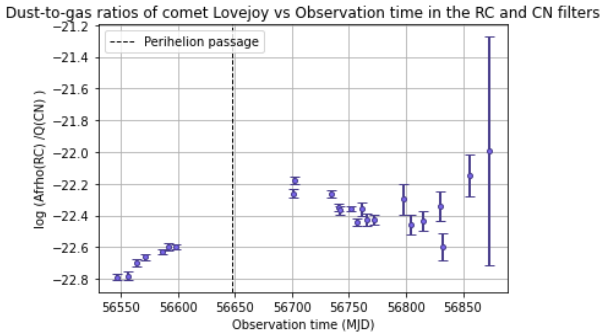

(c) dust-to-gas ratio in the RC and CN filters, with respect to observation time

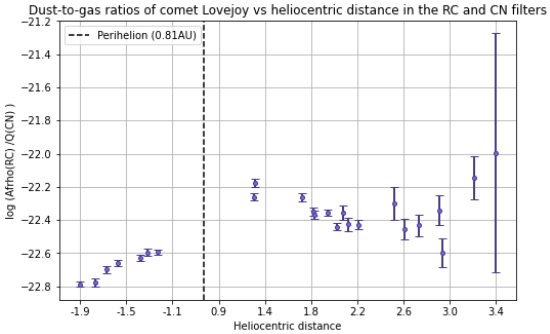

(d) dust-to-gas ratio in the RC and CN filters, with respect to heliocentric distance

Figure 6.9: Dust-to-gas ratios of comet Lovejoy. The $Af\rho$ parameter is expressed in the R and RC filters, and the gas production is expressed in the CN filter. The ratios are expressed with respect to observation time (left) and heliocentric distance (right).

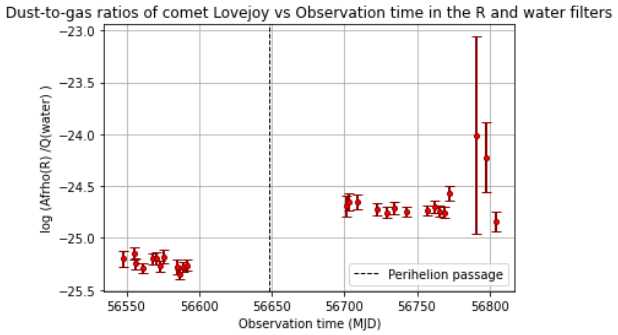

(a) dust-to-gas ratio in the R filter and water production rate, with respect to observation time

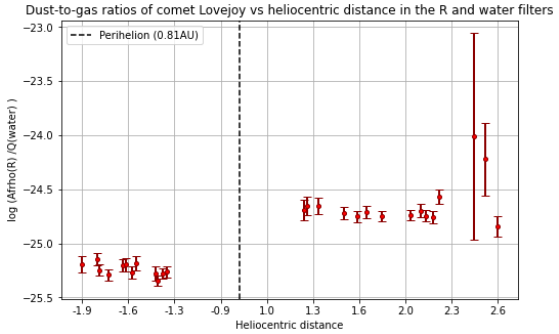

(b) dust-to-gas ratio in the R filter and water production rate, with respect to heliocentric distance

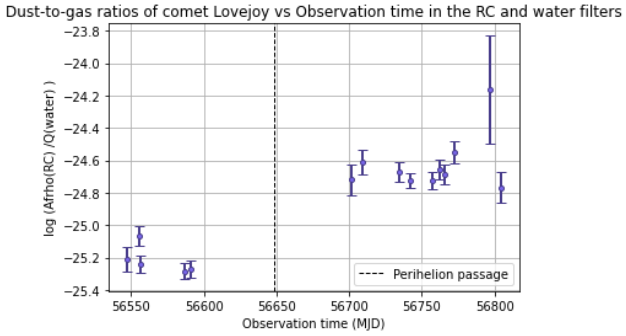

(c) dust-to-gas ratio in the RC filter and water production rate, with respect to observation time

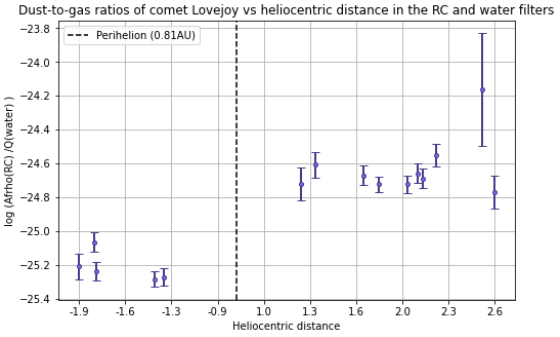

(d) dust-to-gas ratio in the RC filter and water production rate, with respect to heliocentric distance

Figure 6.10: Dust-to-gas ratios of comet Lovejoy. The $Af\rho$ parameter is expressed in the R and RC filters, and the gas production rate is inferred from the OH filter. The ratios are expressed with respect to observation time (left) and heliocentric distance (right).

Chapter 7

Coma morphology

Up to this point, we have focused our analysis on coma composition. In this chapter, we shift our focus to coma morphology. Comae are typically not homogeneous: some regions are more dusty or icy than others and, in turn, more active. This gives rise to features in the coma, such as bright jets, fans, or arcs, that can be observed.

Studying the coma morphology provides indirect insight into the shape of the nucleus, which is concealed from direct observation by the coma itself. For instance, the position of active regions on the comet's surface can be inferred from active zones in the coma. Furthermore, by monitoring the evolution of the coma over time, it is sometimes possible to determine the comet's rotation period based on periodic changes in the coma.

In this chapter, we describe the image processing techniques to enhance our images to detect morphological features, and we present the results of our morphological analysis.

7.1 Image enhancement techniques

Due to the brightness of the coma, features are often difficult to detect on standard images. Therefore, image enhancement techniques are necessary to improve contrast between the internal structures and the surrounding coma, making these features detectable.

The primary enhancement technique used in this thesis is the division by azimuthal median profile. This method, implemented via a Python script developed by Mathieu Vander Donckt, consists of taking a concentric annulus of pixels centered on the comet's optocenter and calculating the median brightness of these pixels. The brightness value of each pixel in the annulus is then divided by this median value. This process is repeated with annuli of varying distances until every pixel in the image is enhanced.

Another method based on image rotation, known as the Larson-Sekanika method, was also applied. This method consists of rotating the original image 10° clockwise, then doing

the same counterclockwise [44]. The average of the two rotated images is then subtracted from the original. While this method yielded no visible features, however, it is included here for completeness.

7.2 Results

We applied the enhancement technique on all CN images of comets PanSTARRS and Lovejoy. Several enhanced images are shown here, and we discuss what structural features are identified in this section. On all images, the directions of North and East are indicated, and an orange arrow shows the direction opposite to the Sun, indicating the direction of the ion tail, and a white arrow shows the projection to the negative of the comet's direction vector, indicating the direction of the dust tail.

Coma morphology of PanSTARRS

Prior to 56816 MJD, no structural feature on the coma of PanSTARRS was observed. Around this date, however, a spiral structure begins to emerge. This feature is likely caused by one or more active regions on the nucleus, with at least one dominant active zone and possibly a smaller one on the opposite side. The emission takes the form of a spiral due to the rotation of the nucleus.

The structure appears particularly strong between MJD 56935 and 56945, a period which coincides with the beginning of the outburst of CN and OH of PanSTARRS discussed in Section 5.4.1. This suggests that the outburst in gas observed around this date was caused by enhanced activity of these active regions. Figure 7.2 also reveals a very faint tail in the antisolar direction during this time. The spiral pattern gradually dissipates and is no longer visible by approximately MJD 56980.

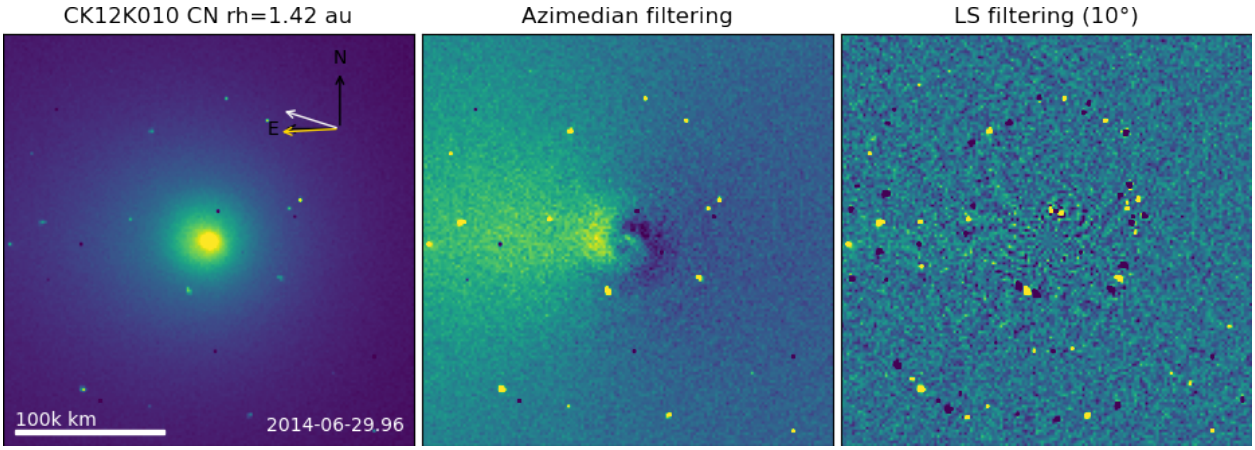

Figure 7.1: 56838 MJD. Spiral structure of CN emission around comet PanSTARRS

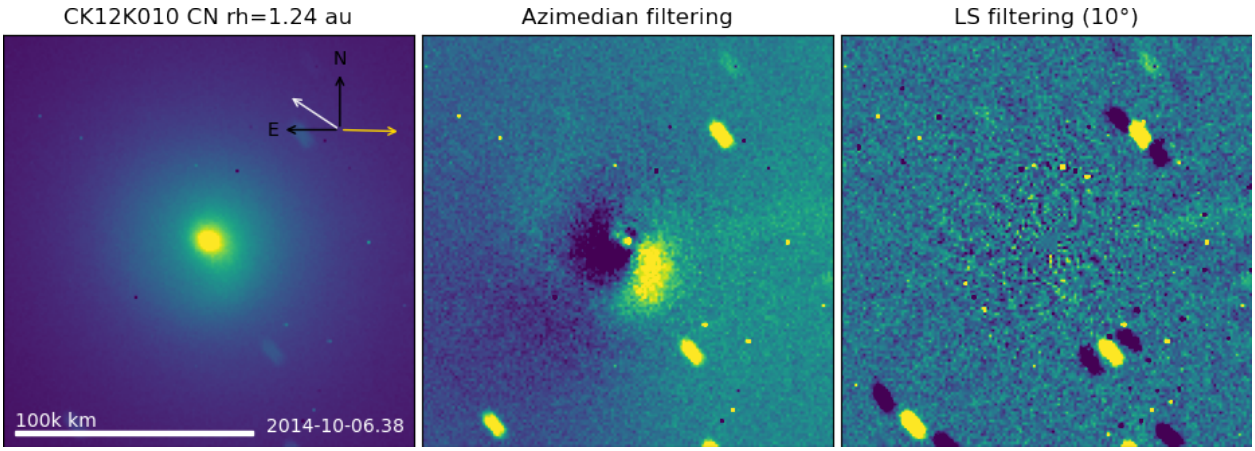

Figure 7.2: 56936 MJD. Spiral structure of CN emission around comet PanSTARRS

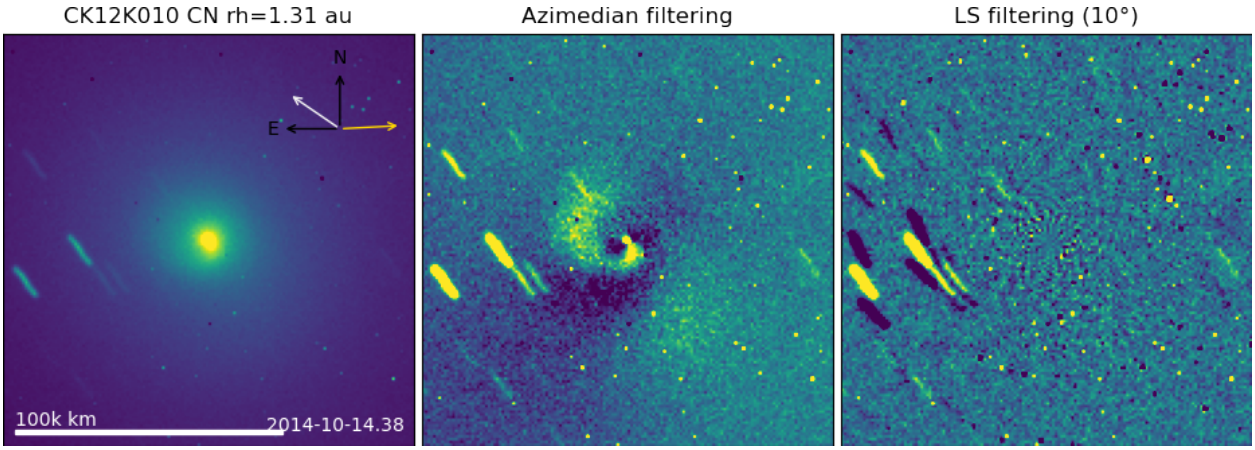

Figure 7.3: 56944 MJD. Spiral structure of CN emission around comet PanSTARRS

Coma morphology of Lovejoy

Lovejoy's coma shows the presence of broad triangular features, called fans, indicating the presence of at least two regions of higher activity. This fan structure starts to dim strongly after 65612 MJD, and completely disappears from our images after 56734 MJD. This time, no tail or jet structure is visible. Notably, no features are present around 56800 MJD, which was the date of the apparent peak in brightness observed in Figure 4.9. This absence of morphological feature changes further confirms that this peak in brightness does not reflect an increase in cometary activity but is instead due to phase angle effects.

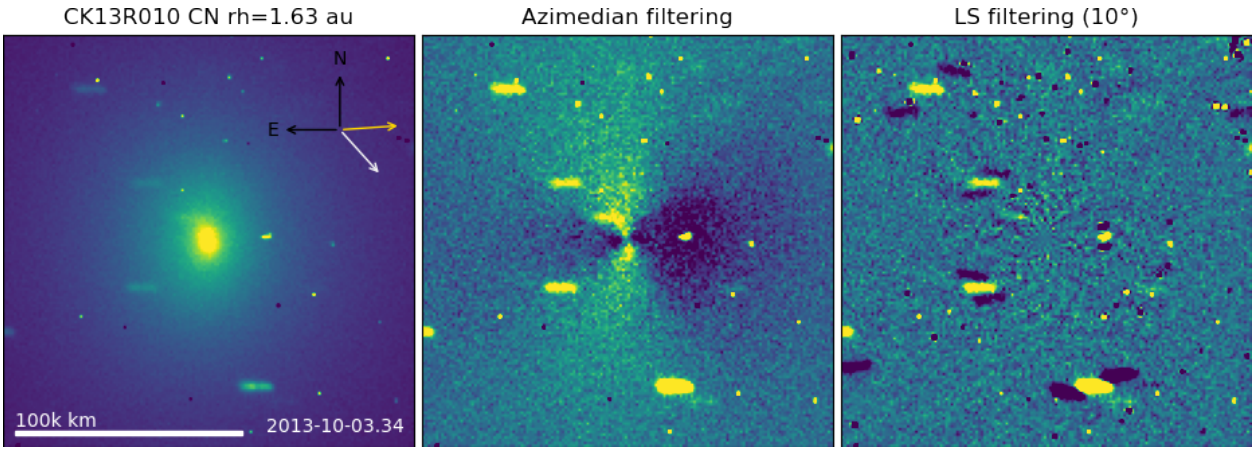

Figure 7.4: 56568 MJD. CN emission around comet Lovejoy

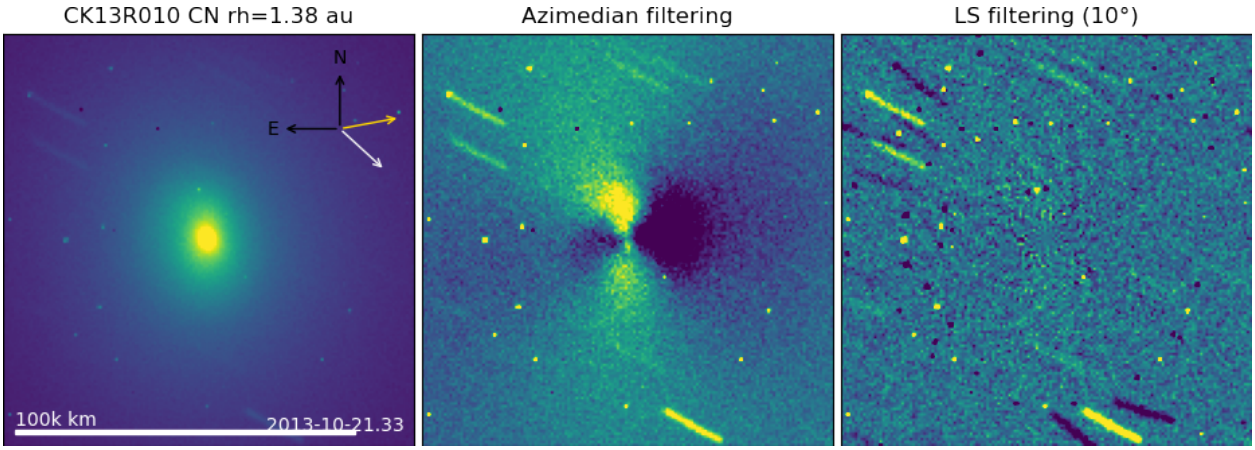

Figure 7.5: 56586 MJD. CN emission around comet Lovejoy

Chapter 8

Conclusion

Studying comets is essential to improve our understanding of the early solar system. In this work, we performed photometry and image monitoring of two comets: the dynamically new comet C/2012 K1 (PanSTARRS) and the long-period returning comet C/2013 R1 (Lovejoy).

This was accomplished using images from the TRAPPIST-South telescope at the La Silla Observatory. The comets were monitored before, during, and after their passage to perihelion, from March 2013 to December 2015 for PanSTARRS and from December 2013 to October 2014 for Lovejoy. Using TRAPPIST-South's various cometary filters, we monitored the evolution of the brightness by computing apparent and heliocentric magnitudes in the broadband BVRI filters. The gas production rates of OH, CN, NH, C_3, and C_2 were also derived using narrowband gas filters, as well as gas abundance ratios. Additionally, the production rate of H_2O was inferred from that of OH. The dust activity was monitored through the $Af\rho$ parameter using R, RC, BC, and GC filters over extended periods and was compared to the cometary gas production by computing dust-to-gas ratios. Finally, the morphology of each comet's coma was also analyzed in the various filters using image enhancement techniques.

For the DNC PanSTARRS comet, the heliocentric magnitude light curve in the BVRI filters revealed an asymmetry: the slopes before perihelion were flatter than those after perihelion. PanSTARRS has color indices very similar to LPCs, suggesting a similar composition. The study of the gas production rates revealed a gas outburst post-perihelion that was not reflected in the dust activity, indicating a gas-only event. The abundance ratio of PanSTARRS correlates with that of a carbon-typical comet. Its dust activity also showed a strong asymmetry, even more pronounced than in the magnitude evolution, with steeper slopes after perihelion than before, and was otherwise featureless. This asymmetry has been observed in DNCs before. Finally, the study of its morphological structures in the coma revealed a spiral structure in the CN gas coma of PanSTARRS, caused by at least one active region on the nucleus, possibly two with a fainter region on the opposite side. A faint tail was also detected.

The evolution of the heliocentric magnitude of Lovejoy is also asymmetric: the comet faded more rapidly after perihelion than it brightened beforehand. However, Lovejoy's apparent and heliocentric magnitudes showed much steeper slopes than PanSTARRS, indicating that Lovejoy is by far the more active comet of the two. Although the light curve displayed an apparent outburst post-perihelion, the study of the dust activity through the angle-corrected $Af\rho$ value revealed that it was only a geometric effect due to phase angle. Lovejoy's color indices were also consistent with those of LPCs, but interestingly, it was the DNC PanSTARRS that was the closest in color to the LPC average. In any case, both DNCs and returning LPCs have the same origin, the Oort Cloud.

Both the $Af\rho$ and gas production rates of Lovejoy followed steeper power-law slopes than PanSTARRS. Lovejoy's gas abundance ratios indicate that it is a carbon-typical comet. Its dust activity and gas production rate were mostly symmetric around perihelion, as is common for LPCs, though a small asymmetry remained: the rate of brightness increasing is faster than its rate of fading. Furthermore, the dust-to-gas ratio revealed that Lovejoy became dustier after perihelion. A possible cause for this behavior is a seasonal effect: the changing solar illumination angle as the comet passes perihelion may cause different active regions on the nucleus to become exposed or shadowed, impacting dust and gas emissions.

Finally, the analysis of the CN coma morphology revealed the presence of two fan structures, indicating the presence of at least two active zones on the surface of Lovejoy's nucleus. Both features dissipated some time after perihelion.

In conclusion, our work focused on monitoring and comparing the evolution of a DNC and a returning LPC. Repeating this type of analysis on a larger sample of DNCs and LPCs will allow us to progressively improve our understanding of the connection between a comet's origin, composition, and evolution. Understanding the source of the asymmetric evolution of DNCs will help us understand their internal structure and composition. Further detection and monitoring of active regions on cometary nuclei will help us characterize cometary surfaces. By applying this approach to a wide range of comets, we can ultimately improve our understanding of comets and, therefore, of the early solar system.

Appendix A

Computed gas production rates

This section contains the computed gas production rates of CN, C_2, C_3, NH, OH, and water of comets PanSTARRS and Lovejoy. MJD represents the date of the observation night in Modified Julian Days, and r_h and Δ represent, respectively, the heliocentric and geocentric distances are expressed in AU, while τ_0 and τ_1 represent the average lifetime of the parent and daughter molecules and are expressed in seconds. Finally, the production rate Q is in molecules per second.

A.1 Gas production rates of PanSTARRS

Computed gas production rates of CN of comet PanSTARRS						
Date	MJD	r_h	Δ	τ_0	τ_1	Q(CN) in molec/s
2014-02-03	56691	3.113	3.240	126000.0	2040000.0	$4.45\times10^{25}\pm5.78\times10^{24}$
2014-02-06	56694	3.079	3.160	123000.0	1990000.0	$3.93\times10^{25}\pm4.45\times10^{24}$
2014-02-09	56697	3.045	3.080	121000.0	1950000.0	$3.80\times10^{25}\pm4.22\times10^{24}$
2014-02-11	56699	3.023	3.027	119000.0	1920000.0	$4.04\times10^{25}\pm3.65\times10^{24}$
2014-02-14	56702	2.989	2.946	116000.0	1880000.0	$3.76\times10^{25}\pm4.29\times10^{24}$
2014-02-17	56705	2.955	2.865	114000.0	1830000.0	$5.63\times10^{25}\pm5.02\times10^{24}$
2014-02-19	56707	2.932	2.811	112000.0	1810000.0	$4.38\times10^{25}\pm4.16\times10^{24}$
2014-02-26	56714	2.852	2.623	106000.0	1710000.0	$5.27\times10^{25}\pm3.94\times10^{24}$
2014-03-04	56720	2.784	2.463	101000.0	1630000.0	$5.72\times10^{25}\pm4.19\times10^{24}$
2014-03-13	56729	2.680	2.232	93400.0	1510000.0	$5.71\times10^{25}\pm3.67\times10^{24}$
2014-03-23	56739	2.563	1.994	85400.0	1380000.0	$6.29\times10^{25}\pm3.90\times10^{24}$
2014-04-01	56748	2.458	1.806	78500.0	1270000.0	$7.03\times10^{25}\pm6.04\times10^{24}$
2014-04-08	56755	2.376	1.683	73400.0	1190000.0	$7.81\times10^{25}\pm6.71\times10^{24}$
2014-04-16	56763	2.283	1.574	67800.0	1090000.0	$7.36\times10^{25}\pm9.43\times10^{24}$
2014-04-23	56770	2.201	1.511	63000.0	1020000.0	$7.36\times10^{25}\pm7.56\times10^{24}$
2014-05-01	56778	2.107	1.475	57700.0	932000.0	$8.65\times10^{25}\pm1.01\times10^{25}$
2014-05-09	56786	2.013	1.479	52700.0	851000.0	$8.27\times10^{25}\pm9.91\times10^{24}$

Computed gas production rates of CN of comet PanSTARRS (continued)						
2014-05-18	56795	1.907	1.524	47300.0	764000.0	$7.57\times10^{25}\pm7.10\times10^{24}$
2014-05-20	56797	1.884	1.539	46100.0	745000.0	$9.05\times10^{25}\pm7.76\times10^{24}$
2014-05-30	56807	1.756	1.642	40100.0	648000.0	$9.22\times10^{25}\pm6.60\times10^{24}$
2014-06-07	56815	1.664	1.732	36000.0	581000.0	$1.02\times10^{26}\pm5.96\times10^{24}$
2014-06-08	56816	1.653	1.744	35500.0	574000.0	$9.06\times10^{25}\pm5.33\times10^{24}$
2014-06-09	56817	1.641	1.755	35000.0	566000.0	$8.49\times10^{25}\pm5.23\times10^{24}$
2014-06-14	56822	1.585	1.814	32700.0	528000.0	$8.31\times10^{25}\pm5.19\times10^{24}$
2014-06-23	56831	1.486	1.914	28700.0	464000.0	$9.75\times10^{25}\pm5.99\times10^{24}$
2014-06-29	56837	1.423	1.975	26300.0	425000.0	$1.18\times10^{26}\pm8.76\times10^{24}$
2014-07-03	56841	1.382	2.012	24800.0	401000.0	$1.24\times10^{26}\pm8.86\times10^{24}$
2014-09-06	56906	1.067	1.816	14800.0	239000.0	$1.35\times10^{26}\pm9.63\times10^{24}$
2014-09-07	56907	1.070	1.800	14900.0	240000.0	$1.18\times10^{26}\pm9.39\times10^{24}$
2014-09-20	56920	1.126	1.564	16500.0	266000.0	$9.59\times10^{25}\pm4.86\times10^{24}$
2014-09-27	56927	1.171	1.424	17800.0	288000.0	$9.29\times10^{25}\pm3.42\times10^{24}$
2014-09-28	56928	1.179	1.404	18100.0	292000.0	$1.00\times10^{26}\pm3.31\times10^{24}$
2014-10-06	56936	1.242	1.245	20100.0	324000.0	$9.66\times10^{25}\pm2.66\times10^{24}$
2014-10-07	56937	1.250	1.227	20300.0	328000.0	$1.07\times10^{26}\pm3.93\times10^{24}$
2014-10-11	56941	1.286	1.154	21500.0	347000.0	$7.44\times10^{25}\pm1.99\times10^{24}$
2014-10-13	56943	1.303	1.121	22100.0	357000.0	$8.63\times10^{25}\pm3.28\times10^{24}$
2014-10-13	56943	1.303	1.121	22100.0	357000.0	$8.49\times10^{25}\pm3.02\times10^{24}$
2014-10-13	56943	1.303	1.121	22100.0	357000.0	$8.48\times10^{25}\pm2.98\times10^{24}$
2014-10-13	56943	1.303	1.121	22100.0	357000.0	$9.03\times10^{25}\pm3.11\times10^{24}$
2014-10-13	56943	1.304	1.120	22100.0	357000.0	$8.51\times10^{25}\pm2.48\times10^{24}$
2014-10-13	56943	1.304	1.120	22100.0	357000.0	$8.44\times10^{25}\pm2.35\times10^{24}$
2014-10-13	56943	1.304	1.120	22100.0	357000.0	$8.29\times10^{25}\pm2.15\times10^{24}$
2014-10-13	56943	1.304	1.120	22100.0	357000.0	$8.18\times10^{25}\pm2.20\times10^{24}$
2014-10-13	56943	1.304	1.120	22100.0	357000.0	$8.07\times10^{25}\pm1.98\times10^{24}$
2014-10-14	56944	1.313	1.104	22400.0	362000.0	$7.21\times10^{25}\pm2.04\times10^{24}$
2014-10-14	56944	1.313	1.104	22400.0	362000.0	$7.59\times10^{25}\pm2.07\times10^{24}$
2014-10-14	56944	1.313	1.103	22400.0	362000.0	$7.21\times10^{25}\pm1.67\times10^{24}$
2014-10-23	56953	1.402	0.989	25600.0	413000.0	$7.28\times10^{25}\pm2.04\times10^{24}$
2014-10-27	56957	1.443	0.962	27100.0	437000.0	$7.74\times10^{25}\pm2.07\times10^{24}$
2014-11-04	56965	1.530	0.963	30400.0	492000.0	$5.56\times10^{25}\pm1.71\times10^{24}$
2014-11-06	56967	1.551	0.975	31300.0	505000.0	$6.34\times10^{25}\pm1.98\times10^{24}$
2014-11-07	56968	1.561	0.982	31700.0	512000.0	$5.70\times10^{25}\pm1.87\times10^{24}$
2014-11-09	56970	1.585	1.003	32700.0	528000.0	$6.34\times10^{25}\pm2.44\times10^{24}$
2014-11-10	56971	1.594	1.012	33000.0	534000.0	$5.41\times10^{25}\pm1.92\times10^{24}$
2014-11-13	56974	1.629	1.054	34500.0	557000.0	$5.48\times10^{25}\pm1.94\times10^{24}$
2014-11-13	56974	1.630	1.055	34500.0	558000.0	$5.83\times10^{25}\pm2.22\times10^{24}$
2014-11-18	56979	1.686	1.140	37000.0	597000.0	$5.86\times10^{25}\pm1.69\times10^{24}$
2014-11-27	56988	1.789	1.339	41600.0	672000.0	$5.36\times10^{25}\pm1.95\times10^{24}$
2014-12-04	56995	1.871	1.520	45500.0	735000.0	$4.47\times10^{25}\pm1.90\times10^{24}$

Computed gas production rates of CN of comet PanSTARRS (continued)						
2014-12-06	56997	1.895	1.575	46700.0	754000.0	$4.01\times10^{25}\pm2.86\times10^{24}$
2014-12-08	56999	1.918	1.629	47800.0	773000.0	$4.78\times10^{25}\pm2.20\times10^{24}$
2014-12-15	57006	2.000	1.829	52000.0	840000.0	$4.54\times10^{25}\pm1.95\times10^{24}$
2014-12-19	57010	2.047	1.943	54500.0	880000.0	$3.74\times10^{25}\pm1.23\times10^{24}$
2015-01-03	57025	2.224	2.381	64300.0	1040000.0	$3.30\times10^{25}\pm2.05\times10^{24}$
2015-01-09	57031	2.295	2.551	68500.0	1110000.0	$2.95\times10^{25}\pm1.84\times10^{24}$
2015-01-20	57042	2.424	2.851	76400.0	1230000.0	$2.56\times10^{25}\pm1.77\times10^{24}$
2015-01-28	57050	2.518	3.056	82400.0	1330000.0	$1.59\times10^{25}\pm1.74\times10^{24}$
2015-02-02	57055	2.576	3.179	86300.0	1390000.0	$1.50\times10^{25}\pm2.68\times10^{24}$

Computed gas production rates of C_2 of comet PanSTARRS						
Date	MJD	r_h	Δ	τ_0	τ_1	$Q(C_2)$
2014-02-03	56691	3.113	3.240	213000.0	640000.0	$7.60\times10^{25}\pm8.75\times10^{24}$
2014-02-07	56695	3.068	3.134	207000.0	621000.0	$4.87\times10^{25}\pm7.20\times10^{24}$
2014-02-09	56697	3.046	3.080	204000.0	612000.0	$4.31\times10^{25}\pm7.22\times10^{24}$
2014-02-11	56699	3.023	3.027	201000.0	603000.0	$5.68\times10^{25}\pm7.74\times10^{24}$
2014-02-14	56702	2.989	2.947	197000.0	590000.0	$5.07\times10^{25}\pm9.54\times10^{24}$
2014-02-20	56708	2.921	2.784	188000.0	563000.0	$7.20\times10^{25}\pm6.10\times10^{24}$
2014-02-26	56714	2.853	2.623	179000.0	537000.0	$7.12\times10^{25}\pm6.19\times10^{24}$
2014-03-04	56720	2.784	2.464	171000.0	512000.0	$8.43\times10^{25}\pm6.31\times10^{24}$
2014-03-13	56729	2.680	2.233	158000.0	474000.0	$7.48\times10^{25}\pm4.99\times10^{24}$
2014-03-23	56739	2.564	1.995	145000.0	434000.0	$7.06\times10^{25}\pm5.70\times10^{24}$
2014-04-01	56748	2.458	1.806	133000.0	399000.0	$6.75\times10^{25}\pm6.58\times10^{24}$
2014-04-08	56755	2.377	1.683	124000.0	373000.0	$7.56\times10^{25}\pm7.55\times10^{24}$
2014-04-16	56763	2.283	1.575	115000.0	344000.0	$9.23\times10^{25}\pm9.99\times10^{24}$
2014-04-23	56770	2.202	1.511	107000.0	320000.0	$9.36\times10^{25}\pm9.39\times10^{24}$
2014-05-06	56783	2.048	1.473	92300.0	277000.0	$8.05\times10^{25}\pm7.50\times10^{24}$
2014-05-09	56786	2.013	1.479	89100.0	267000.0	$9.68\times10^{25}\pm1.05\times10^{25}$
2014-05-18	56795	1.907	1.524	80000.0	240000.0	$1.10\times10^{26}\pm8.64\times10^{24}$
2014-05-20	56797	1.884	1.539	78100.0	234000.0	$1.19\times10^{26}\pm7.67\times10^{24}$
2014-06-07	56815	1.664	1.732	60900.0	183000.0	$1.55\times10^{26}\pm6.42\times10^{24}$
2014-06-08	56816	1.652	1.744	60000.0	180000.0	$1.39\times10^{26}\pm5.82\times10^{24}$
2014-06-09	56817	1.641	1.756	59200.0	178000.0	$1.42\times10^{26}\pm5.78\times10^{24}$
2014-06-14	56822	1.585	1.814	55300.0	166000.0	$1.29\times10^{26}\pm5.50\times10^{24}$
2014-06-23	56831	1.486	1.915	48600.0	146000.0	$1.69\times10^{26}\pm7.00\times10^{24}$
2014-07-03	56841	1.382	2.012	42000.0	126000.0	$1.98\times10^{26}\pm9.53\times10^{24}$
2014-09-06	56906	1.067	1.816	25000.0	75100.0	$2.40\times10^{26}\pm9.45\times10^{24}$
2014-09-07	56907	1.070	1.800	25200.0	75600.0	$2.19\times10^{26}\pm9.31\times10^{24}$
2014-09-20	56920	1.126	1.564	27900.0	83700.0	$1.74\times10^{26}\pm5.23\times10^{24}$
2014-09-27	56927	1.171	1.424	30200.0	90500.0	$1.71\times10^{26}\pm3.49\times10^{24}$
2014-09-28	56928	1.178	1.404	30500.0	91600.0	$1.72\times10^{26}\pm3.18\times10^{24}$
2014-10-06	56936	1.242	1.245	33900.0	102000.0	$1.68\times10^{26}\pm2.96\times10^{24}$
2014-10-07	56937	1.250	1.227	34400.0	103000.0	$1.88\times10^{26}\pm3.91\times10^{24}$
2014-10-11	56941	1.285	1.154	36300.0	109000.0	$1.59\times10^{26}\pm2.96\times10^{24}$
2014-10-13	56943	1.303	1.121	37400.0	112000.0	$1.42\times10^{26}\pm3.75\times10^{24}$
2014-10-13	56943	1.304	1.120	37400.0	112000.0	$1.35\times10^{26}\pm4.43\times10^{24}$
2014-10-14	56944	1.313	1.104	37900.0	114000.0	$1.46\times10^{26}\pm2.74\times10^{24}$
2014-10-23	56953	1.402	0.989	43200.0	130000.0	$1.24\times10^{26}\pm2.87\times10^{24}$
2014-10-27	56957	1.443	0.962	45800.0	137000.0	$1.14\times10^{26}\pm2.93\times10^{24}$
2014-11-07	56968	1.561	0.982	53600.0	161000.0	$8.48\times10^{25}\pm4.23\times10^{24}$
2014-11-09	56970	1.585	1.003	55300.0	166000.0	$8.21\times10^{25}\pm3.01\times10^{24}$
2014-11-10	56971	1.594	1.012	55900.0	168000.0	$8.13\times10^{25}\pm2.97\times10^{24}$

Computed gas production rates of C_2 of comet PanSTARRS (continued)						
2014-11-13	56974	1.629	1.054	58400.0	175000.0	$7.69\times10^{25}\pm2.59\times10^{24}$
2014-11-13	56974	1.629	1.055	58400.0	175000.0	$7.52\times10^{25}\pm2.46\times10^{24}$
2014-11-15	56976	1.652	1.087	60000.0	180000.0	$7.34\times10^{25}\pm3.44\times10^{24}$
2014-11-18	56979	1.685	1.139	62500.0	187000.0	$7.48\times10^{25}\pm2.20\times10^{24}$
2014-11-27	56988	1.790	1.340	70500.0	211000.0	$7.21\times10^{25}\pm2.47\times10^{24}$
2014-12-04	56995	1.871	1.521	77000.0	231000.0	$5.06\times10^{25}\pm2.80\times10^{24}$
2014-12-15	57006	2.000	1.829	88000.0	264000.0	$5.07\times10^{25}\pm2.56\times10^{24}$
2014-12-19	57010	2.047	1.944	92200.0	277000.0	$4.32\times10^{25}\pm1.63\times10^{24}$
2015-01-03	57025	2.225	2.382	109000.0	327000.0	$3.15\times10^{25}\pm3.85\times10^{24}$
2015-01-09	57031	2.295	2.551	116000.0	348000.0	$3.09\times10^{25}\pm3.28\times10^{24}$
2015-01-20	57042	2.425	2.852	129000.0	388000.0	$4.25\times10^{25}\pm3.07\times10^{24}$
2015-01-28	57050	2.518	3.057	139000.0	418000.0	$2.78\times10^{25}\pm3.01\times10^{24}$
2015-02-02	57055	2.577	3.179	146000.0	438000.0	$3.44\times10^{25}\pm4.86\times10^{24}$

Computed gas production rates of C_3 of comet PanSTARRS						
Date	MJD	r_h	Δ	τ_0	τ_1	Q(C_3)
2014-02-07	56695	3.068	3.134	26400.0	254000.0	$8.34\times10^{23}\pm8.86\times10^{23}$
2014-02-11	56699	3.023	3.027	25600.0	247000.0	$1.86\times10^{23}\pm8.59\times10^{23}$
2014-02-21	56709	2.910	2.758	23700.0	229000.0	$2.14\times10^{24}\pm2.41\times10^{24}$
2014-03-23	56739	2.564	1.994	18400.0	178000.0	$5.62\times10^{24}\pm1.56\times10^{24}$
2014-04-01	56748	2.458	1.805	16900.0	163000.0	$6.38\times10^{24}\pm1.98\times10^{24}$
2014-04-08	56755	2.376	1.683	15800.0	152000.0	$6.03\times10^{24}\pm2.63\times10^{24}$
2014-05-30	56807	1.756	1.643	8630.0	83300.0	$1.80\times10^{25}\pm2.37\times10^{24}$
2014-06-07	56815	1.664	1.732	7750.0	74800.0	$2.10\times10^{25}\pm1.93\times10^{24}$
2014-06-08	56816	1.653	1.744	7650.0	73800.0	$1.85\times10^{25}\pm1.82\times10^{24}$
2014-06-09	56817	1.641	1.755	7540.0	72700.0	$1.93\times10^{25}\pm1.85\times10^{24}$
2014-09-06	56906	1.067	1.816	3190.0	30700.0	$3.54\times10^{25}\pm3.51\times10^{24}$
2014-09-20	56920	1.126	1.564	3550.0	34200.0	$2.44\times10^{25}\pm1.85\times10^{24}$
2014-09-27	56927	1.171	1.424	3840.0	37000.0	$2.30\times10^{25}\pm1.16\times10^{24}$
2014-09-28	56928	1.178	1.404	3890.0	37500.0	$2.73\times10^{25}\pm1.08\times10^{24}$
2014-10-06	56936	1.242	1.245	4320.0	41600.0	$2.40\times10^{25}\pm8.89\times10^{23}$
2014-10-07	56937	1.250	1.227	4380.0	42200.0	$2.94\times10^{25}\pm1.91\times10^{24}$
2014-10-11	56941	1.286	1.154	4630.0	44700.0	$2.68\times10^{25}\pm1.43\times10^{24}$
2014-10-13	56943	1.303	1.121	4750.0	45800.0	$2.19\times10^{25}\pm1.15\times10^{24}$
2014-10-13	56943	1.304	1.120	4760.0	45900.0	$1.97\times10^{25}\pm1.44\times10^{24}$
2014-10-14	56944	1.313	1.104	4830.0	46500.0	$2.18\times10^{25}\pm7.21\times10^{23}$
2014-10-23	56953	1.402	0.989	5500.0	53100.0	$1.88\times10^{25}\pm5.91\times10^{23}$
2014-10-27	56957	1.443	0.962	5830.0	56200.0	$1.93\times10^{25}\pm6.05\times10^{23}$
2014-11-07	56968	1.561	0.982	6820.0	65800.0	$1.34\times10^{25}\pm8.16\times10^{23}$
2014-11-10	56971	1.594	1.012	7110.0	68600.0	$1.26\times10^{25}\pm9.57\times10^{23}$
2014-11-13	56974	1.629	1.054	7430.0	71600.0	$1.18\times10^{25}\pm9.36\times10^{23}$
2014-11-13	56974	1.630	1.055	7440.0	71700.0	$1.20\times10^{25}\pm7.01\times10^{23}$
2014-11-15	56976	1.653	1.087	7650.0	73800.0	$1.13\times10^{25}\pm1.28\times10^{24}$
2014-11-18	56979	1.685	1.139	7950.0	76700.0	$1.23\times10^{25}\pm8.17\times10^{23}$
2014-11-27	56988	1.789	1.339	8960.0	86400.0	$1.14\times10^{25}\pm8.74\times10^{23}$
2014-11-27	56988	1.790	1.339	8970.0	86500.0	$1.13\times10^{25}\pm9.14\times10^{23}$
2014-12-04	56995	1.871	1.520	9800.0	94500.0	$7.92\times10^{24}\pm9.90\times10^{23}$
2014-12-08	56999	1.918	1.630	10300.0	99300.0	$8.75\times10^{24}\pm1.25\times10^{24}$
2014-12-15	57006	2.0	1.829	11200.0	108000.0	$8.60\times10^{24}\pm6.67\times10^{23}$
2014-12-19	57010	2.047	1.944	11700.0	113000.0	$6.10\times10^{24}\pm4.75\times10^{23}$
2015-01-03	57025	2.225	2.381	13900.0	134000.0	$3.84\times10^{24}\pm1.14\times10^{24}$

Computed gas production rates of NH of comet PanSTARRS						
Date	MJD	r_h	Δ	τ_0	τ_1	Q(NH)
2014-02-21	56709	2.910	2.758	423000.0	1270000.0	$4.17\times10^{23}\pm3.56\times10^{25}$
2014-04-08	56755	2.376	1.683	282000.0	847000.0	$4.48\times10^{25}\pm1.01\times10^{26}$
2014-09-06	56906	1.067	1.816	56900.0	171000.0	$3.11\times10^{26}\pm4.81\times10^{25}$
2014-09-27	56927	1.171	1.424	68600.0	206000.0	$2.13\times10^{26}\pm1.73\times10^{25}$
2014-09-28	56928	1.179	1.404	69500.0	209000.0	$2.32\times10^{26}\pm1.69\times10^{25}$
2014-10-06	56936	1.242	1.245	77100.0	231000.0	$2.00\times10^{26}\pm1.31\times10^{25}$
2014-10-07	56937	1.250	1.227	78100.0	234000.0	$2.04\times10^{26}\pm1.83\times10^{25}$
2014-10-11	56941	1.286	1.154	82700.0	248000.0	$1.60\times10^{26}\pm1.17\times10^{25}$
2014-10-13	56943	1.304	1.120	85000.0	255000.0	$1.31\times10^{26}\pm1.86\times10^{25}$
2014-10-14	56944	1.313	1.104	86200.0	259000.0	$1.54\times10^{26}\pm1.02\times10^{25}$
2014-10-23	56953	1.402	0.989	98300.0	295000.0	$1.08\times10^{26}\pm8.95\times10^{24}$
2014-10-27	56957	1.443	0.962	104000.0	312000.0	$1.02\times10^{26}\pm9.99\times10^{24}$
2014-11-09	56970	1.585	1.003	126000.0	377000.0	$4.60\times10^{25}\pm1.61\times10^{25}$
2014-11-10	56971	1.594	1.012	127000.0	381000.0	$4.80\times10^{25}\pm1.27\times10^{25}$
2014-11-13	56974	1.629	1.054	133000.0	398000.0	$3.87\times10^{25}\pm1.20\times10^{25}$
2014-11-13	56974	1.630	1.055	133000.0	399000.0	$3.91\times10^{25}\pm1.66\times10^{25}$
2014-11-18	56979	1.686	1.140	142000.0	426000.0	$3.97\times10^{25}\pm7.95\times10^{24}$
2014-11-27	56988	1.789	1.339	160000.0	480000.0	$4.33\times10^{25}\pm9.48\times10^{24}$
2014-12-04	56995	1.871	1.520	175000.0	525000.0	$7.82\times10^{23}\pm1.12\times10^{25}$
2014-12-06	56997	1.895	1.575	180000.0	539000.0	$1.10\times10^{25}\pm1.65\times10^{25}$
2014-12-08	56999	1.918	1.629	184000.0	552000.0	$3.64\times10^{24}\pm1.06\times10^{25}$
2014-12-15	57006	2.000	1.828	200000.0	600000.0	$9.62\times10^{24}\pm8.11\times10^{24}$
2014-12-19	57010	2.046	1.943	209000.0	628000.0	$1.03\times10^{23}\pm1.60\times10^{24}$

Computed gas production rates of OH of comet PanSTARRS						
Date	MJD	r_h	Δ	τ_0	τ_1	Q(OH)
2014-03-23	56739	2.563	1.993	158000.0	1050000.0	$2.83\times10^{28}\pm8.89\times10^{27}$
2014-06-14	56822	1.585	1.814	60300.0	402000.0	$4.39\times10^{28}\pm1.47\times10^{28}$
2014-06-29	56837	1.423	1.975	48600.0	324000.0	$6.92\times10^{28}\pm2.22\times10^{28}$
2014-09-06	56906	1.067	1.816	27300.0	182000.0	$3.41\times10^{28}\pm1.20\times10^{28}$
2014-09-07	56907	1.070	1.800	27500.0	183000.0	$2.43\times10^{28}\pm7.55\times10^{27}$
2014-09-20	56920	1.126	1.564	30400.0	203000.0	$2.52\times10^{28}\pm5.42\times10^{27}$
2014-09-27	56927	1.171	1.424	32900.0	219000.0	$2.81\times10^{28}\pm4.01\times10^{27}$
2014-09-28	56928	1.179	1.403	33400.0	222000.0	$3.12\times10^{28}\pm3.97\times10^{27}$
2014-10-06	56936	1.242	1.245	37000.0	247000.0	$4.14\times10^{28}\pm4.25\times10^{27}$
2014-10-07	56937	1.250	1.227	37500.0	250000.0	$4.00\times10^{28}\pm5.38\times10^{27}$
2014-10-11	56941	1.286	1.153	39700.0	265000.0	$5.20\times10^{28}\pm4.77\times10^{27}$
2014-10-13	56943	1.304	1.120	40800.0	272000.0	$4.49\times10^{28}\pm4.68\times10^{27}$
2014-10-14	56944	1.313	1.103	41400.0	276000.0	$4.03\times10^{28}\pm3.59\times10^{27}$
2014-10-23	56953	1.402	0.989	47200.0	314000.0	$3.73\times10^{28}\pm3.08\times10^{27}$
2014-10-27	56957	1.443	0.962	50000.0	333000.0	$4.03\times10^{28}\pm3.36\times10^{27}$
2014-11-09	56970	1.585	1.003	60300.0	402000.0	$3.56\times10^{28}\pm3.92\times10^{27}$
2014-11-13	56974	1.629	1.054	63700.0	425000.0	$2.87\times10^{28}\pm3.17\times10^{27}$
2014-11-13	56974	1.630	1.055	63800.0	425000.0	$2.83\times10^{28}\pm3.68\times10^{27}$
2014-11-18	56979	1.686	1.140	68200.0	455000.0	$2.82\times10^{28}\pm3.17\times10^{27}$
2014-11-27	56988	1.789	1.339	76800.0	512000.0	$2.55\times10^{28}\pm3.01\times10^{27}$
2014-12-04	56995	1.871	1.519	84000.0	560000.0	$2.21\times10^{28}\pm2.59\times10^{27}$
2014-12-06	56997	1.895	1.575	86200.0	575000.0	$2.10\times10^{28}\pm3.33\times10^{27}$
2014-12-08	56999	1.917	1.629	88200.0	588000.0	$2.01\times10^{28}\pm2.43\times10^{27}$
2014-12-15	57006	2.000	1.828	96000.0	640000.0	$1.78\times10^{28}\pm2.15\times10^{27}$
2014-12-19	57010	2.046	1.942	100000.0	670000.0	$1.55\times10^{28}\pm1.62\times10^{27}$
2015-01-03	57025	2.224	2.380	119000.0	791000.0	$9.47\times10^{27}\pm1.76\times10^{27}$
2015-01-09	57031	2.295	2.550	126000.0	843000.0	$8.30\times10^{27}\pm1.66\times10^{27}$

Computed gas production rates of water of comet PanSTARRS						
Date	MJD	r_h	Δ	τ_0	τ_1	Q(H_2O)
2014-03-23	56739	2.563	1.993	158000.0	1050000.0	$2.40\times10^{28}\pm7.56\times10^{27}$
2014-06-14	56822	1.585	1.814	60300.0	402000.0	$4.74\times10^{28}\pm1.59\times10^{28}$
2014-06-29	56837	1.423	1.975	48600.0	324000.0	$7.90\times10^{28}\pm2.53\times10^{28}$
2014-09-06	56906	1.067	1.816	27300.0	182000.0	$4.50\times10^{28}\pm1.58\times10^{28}$
2014-09-07	56907	1.07	1.8	27500.0	183000.0	$3.20\times10^{28}\pm9.94\times10^{27}$
2014-09-20	56920	1.126	1.564	30400.0	203000.0	$3.23\times10^{28}\pm6.95\times10^{27}$
2014-09-27	56927	1.171	1.424	32900.0	219000.0	$3.53\times10^{28}\pm5.04\times10^{27}$
2014-09-28	56928	1.179	1.403	33400.0	222000.0	$3.91\times10^{28}\pm4.98\times10^{27}$
2014-10-06	56936	1.242	1.245	37000.0	247000.0	$5.06\times10^{28}\pm5.19\times10^{27}$
2014-10-07	56937	1.25	1.227	37500.0	250000.0	$4.87\times10^{28}\pm6.55\times10^{27}$
2014-10-11	56941	1.286	1.153	39700.0	265000.0	$6.24\times10^{28}\pm5.73\times10^{27}$
2014-10-13	56943	1.304	1.12	40800.0	272000.0	$5.35\times10^{28}\pm5.58\times10^{27}$
2014-10-14	56944	1.313	1.103	41400.0	276000.0	$4.79\times10^{28}\pm4.26\times10^{27}$
2014-10-23	56953	1.402	0.989	47200.0	314000.0	$4.29\times10^{28}\pm3.54\times10^{27}$
2014-10-27	56957	1.443	0.962	50000.0	333000.0	$4.57\times10^{28}\pm3.81\times10^{27}$
2014-11-09	56970	1.585	1.003	60300.0	402000.0	$3.85\times10^{28}\pm4.24\times10^{27}$
2014-11-13	56974	1.629	1.054	63700.0	425000.0	$3.06\times10^{28}\pm3.38\times10^{27}$
2014-11-13	56974	1.63	1.055	63800.0	425000.0	$3.01\times10^{28}\pm3.92\times10^{27}$
2014-11-18	56979	1.686	1.14	68200.0	455000.0	$2.96\times10^{28}\pm3.32\times10^{27}$
2014-11-27	56988	1.789	1.339	76800.0	512000.0	$2.59\times10^{28}\pm3.07\times10^{27}$
2014-12-04	56995	1.871	1.519	84000.0	560000.0	$2.20\times10^{28}\pm2.58\times10^{27}$
2014-12-06	56997	1.895	1.575	86200.0	575000.0	$2.08\times10^{28}\pm3.29\times10^{27}$
2014-12-08	56999	1.917	1.629	88200.0	588000.0	$1.97\times10^{28}\pm2.39\times10^{27}$
2014-12-15	57006	2.0	1.828	96000.0	640000.0	$1.71\times10^{28}\pm2.07\times10^{27}$
2014-12-19	57010	2.046	1.942	100000.0	670000.0	$1.48\times10^{28}\pm1.54\times10^{27}$
2015-01-03	57025	2.224	2.38	119000.0	791000.0	$8.65\times10^{27}\pm1.61\times10^{27}$
2015-01-09	57031	2.295	2.55	126000.0	843000.0	$7.46\times10^{27}\pm1.49\times10^{27}$

A.2 Gas production rates of Lovejoy

Computed gas production rates of CN of comet Lovejoy						
Date	MJD	r_h	Δ	τ_0	τ_1	Q(CN)
2013-09-11	56546	1.920	1.835	47900.0	774000.0	$2.62\times10^{25}\pm8.32\times10^{23}$
2013-09-16	56551	1.854	1.714	44700.0	722000.0	$2.97\times10^{25}\pm9.09\times10^{23}$
2013-09-21	56556	1.787	1.594	41500.0	671000.0	$2.99\times10^{25}\pm1.37\times10^{24}$
2013-09-24	56559	1.746	1.519	39600.0	640000.0	$3.24\times10^{25}\pm1.14\times10^{24}$
2013-09-25	56560	1.733	1.495	39000.0	631000.0	$3.36\times10^{25}\pm1.27\times10^{24}$
2013-09-29	56564	1.680	1.399	36700.0	593000.0	$3.61\times10^{25}\pm1.62\times10^{24}$
2013-10-03	56568	1.626	1.300	34400.0	555000.0	$3.72\times10^{25}\pm1.22\times10^{24}$
2013-10-04	56569	1.612	1.275	33800.0	546000.0	$3.93\times10^{25}\pm1.16\times10^{24}$
2013-10-05	56570	1.599	1.252	33200.0	537000.0	$4.00\times10^{25}\pm1.17\times10^{24}$
2013-10-06	56571	1.585	1.227	32700.0	528000.0	$3.67\times10^{25}\pm1.12\times10^{24}$
2013-10-08	56573	1.558	1.178	31600.0	510000.0	$3.47\times10^{25}\pm1.19\times10^{24}$
2013-10-10	56575	1.532	1.130	30500.0	493000.0	$4.56\times10^{25}\pm1.51\times10^{24}$
2013-10-20	56585	1.398	0.892	25400.0	410000.0	$5.15\times10^{25}\pm1.91\times10^{24}$
2013-10-21	56586	1.384	0.868	24900.0	402000.0	$5.85\times10^{25}\pm2.08\times10^{24}$
2013-10-24	56589	1.344	0.798	23500.0	379000.0	$6.47\times10^{25}\pm1.80\times10^{24}$
2013-10-26	56591	1.318	0.754	22600.0	365000.0	$6.48\times10^{25}\pm2.96\times10^{24}$
2013-11-02	56598	1.227	0.605	19600.0	316000.0	$8.05\times10^{25}\pm2.59\times10^{24}$
2014-02-13	56701	1.256	1.556	20500.0	331000.0	$7.83\times10^{25}\pm4.12\times10^{24}$
2014-02-14	56702	1.269	1.560	20900.0	338000.0	$6.44\times10^{25}\pm3.36\times10^{24}$
2014-02-16	56704	1.295	1.567	21800.0	352000.0	$5.48\times10^{25}\pm2.96\times10^{24}$
2014-02-21	56709	1.361	1.581	24100.0	389000.0	$5.33\times10^{25}\pm2.47\times10^{24}$
2014-03-06	56722	1.535	1.589	30600.0	495000.0	$4.65\times10^{25}\pm1.70\times10^{24}$
2014-03-13	56729	1.629	1.580	34500.0	557000.0	$3.99\times10^{25}\pm1.45\times10^{24}$
2014-03-18	56734	1.696	1.569	37400.0	604000.0	$3.44\times10^{25}\pm1.60\times10^{24}$
2014-03-20	56736	1.723	1.564	38600.0	623000.0	$3.41\times10^{25}\pm1.26\times10^{24}$
2014-03-25	56741	1.791	1.549	41700.0	674000.0	$3.44\times10^{25}\pm1.12\times10^{24}$
2014-03-26	56742	1.804	1.546	42300.0	683000.0	$3.58\times10^{25}\pm1.15\times10^{24}$
2014-04-04	56751	1.924	1.516	48100.0	777000.0	$2.74\times10^{25}\pm9.02\times10^{23}$
2014-04-10	56757	2.004	1.497	52200.0	843000.0	$3.00\times10^{25}\pm1.10\times10^{24}$
2014-04-14	56761	2.057	1.485	55000.0	889000.0	$2.34\times10^{25}\pm2.09\times10^{24}$
2014-04-18	56765	2.109	1.476	57800.0	934000.0	$2.40\times10^{25}\pm1.53\times10^{24}$
2014-04-22	56769	2.161	1.469	60700.0	981000.0	$2.62\times10^{25}\pm1.20\times10^{24}$
2014-04-25	56772	2.201	1.465	63000.0	1020000.0	$2.27\times10^{25}\pm1.07\times10^{24}$
2014-05-08	56785	2.369	1.478	73000.0	1180000.0	$1.73\times10^{25}\pm1.83\times10^{24}$
2014-05-14	56791	2.442	1.501	77500.0	1250000.0	$1.80\times10^{25}\pm2.24\times10^{24}$
2014-05-20	56797	2.520	1.539	82600.0	1330000.0	$7.48\times10^{24}\pm1.60\times10^{24}$
2014-05-24	56801	2.571	1.572	85900.0	1390000.0	$1.36\times10^{25}\pm1.96\times10^{24}$

Computed gas production rates of CN of comet Lovejoy (continued)						
2014-05-27	56804	2.608	1.600	88400.0	1430000.0	$1.45\times10^{25}\pm1.84\times10^{24}$
2014-05-31	56808	2.656	1.642	91700.0	1480000.0	$1.51\times10^{25}\pm1.22\times10^{24}$
2014-06-07	56815	2.743	1.734	97800.0	1580000.0	$1.28\times10^{25}\pm1.85\times10^{24}$
2014-06-22	56830	2.926	1.988	111000.0	1800000.0	$6.60\times10^{24}\pm1.35\times10^{24}$
2014-06-24	56832	2.950	2.027	113000.0	1830000.0	$7.16\times10^{24}\pm1.32\times10^{24}$
2014-06-30	56838	3.022	2.151	119000.0	1920000.0	$8.95\times10^{24}\pm2.13\times10^{24}$
2014-07-04	56842	3.067	2.234	122000.0	1980000.0	$9.21\times10^{24}\pm2.23\times10^{24}$
2014-07-06	56844	3.102	2.301	125000.0	2020000.0	$7.49\times10^{24}\pm1.80\times10^{24}$
2014-07-18	56856	3.234	2.568	136000.0	2200000.0	$4.73\times10^{24}\pm1.38\times10^{24}$
2014-08-04	56873	3.430	3.003	153000.0	2470000.0	$1.63\times10^{24}\pm2.52\times10^{24}$

Computed gas production rates of C_2 of comet Lovejoy						
Date	MJD	r_h	Δ	τ_0	τ_1	$Q(C_2)$
2013-09-12	56547	1.907	1.811	80000.0	240000.0	$2.20\times10^{25}\pm1.12\times10^{24}$
2013-09-16	56551	1.853	1.713	75500.0	227000.0	$2.58\times10^{25}\pm1.91\times10^{24}$
2013-09-21	56556	1.788	1.594	70300.0	211000.0	$2.83\times10^{25}\pm2.10\times10^{24}$
2013-09-25	56560	1.733	1.495	66100.0	198000.0	$3.80\times10^{25}\pm1.25\times10^{24}$
2013-09-29	56564	1.680	1.399	62100.0	186000.0	$4.17\times10^{25}\pm2.10\times10^{24}$
2013-10-03	56568	1.625	1.299	58100.0	174000.0	$3.95\times10^{25}\pm1.12\times10^{24}$
2013-10-08	56573	1.558	1.178	53400.0	160000.0	$4.06\times10^{25}\pm1.57\times10^{24}$
2013-10-10	56575	1.531	1.130	51600.0	155000.0	$5.10\times10^{25}\pm3.25\times10^{24}$
2013-10-20	56585	1.398	0.891	43000.0	129000.0	$6.65\times10^{25}\pm3.35\times10^{24}$
2013-10-21	56586	1.384	0.868	42100.0	126000.0	$6.91\times10^{25}\pm1.99\times10^{24}$
2013-10-24	56589	1.344	0.799	39700.0	119000.0	$8.49\times10^{25}\pm2.25\times10^{24}$
2013-10-26	56591	1.319	0.755	38300.0	115000.0	$8.60\times10^{25}\pm3.70\times10^{24}$
2013-11-02	56598	1.228	0.606	33200.0	99500.0	$1.19\times10^{26}\pm2.67\times10^{24}$
2014-02-13	56701	1.256	1.556	34700.0	104000.0	$1.20\times10^{26}\pm4.24\times10^{24}$
2014-02-15	56703	1.282	1.564	36200.0	108000.0	$1.00\times10^{26}\pm3.60\times10^{24}$
2014-02-21	56709	1.361	1.581	40800.0	122000.0	$7.66\times10^{25}\pm2.95\times10^{24}$
2014-02-22	56710	1.374	1.583	41500.0	125000.0	$8.52\times10^{25}\pm2.57\times10^{24}$
2014-02-28	56716	1.454	1.590	46500.0	140000.0	$6.54\times10^{25}\pm1.93\times10^{24}$
2014-03-06	56722	1.534	1.589	51800.0	155000.0	$6.28\times10^{25}\pm1.67\times10^{24}$
2014-03-13	56729	1.629	1.580	58400.0	175000.0	$5.10\times10^{25}\pm1.63\times10^{24}$
2014-03-18	56734	1.696	1.569	63300.0	190000.0	$4.27\times10^{25}\pm2.43\times10^{24}$
2014-03-25	56741	1.790	1.549	70500.0	211000.0	$4.10\times10^{25}\pm2.32\times10^{24}$
2014-03-26	56742	1.803	1.546	71500.0	215000.0	$3.87\times10^{25}\pm1.61\times10^{24}$
2014-04-04	56751	1.924	1.516	81400.0	244000.0	$2.97\times10^{25}\pm1.44\times10^{24}$
2014-04-10	56757	2.003	1.497	88300.0	265000.0	$2.90\times10^{25}\pm1.75\times10^{24}$
2014-04-14	56761	2.057	1.485	93100.0	279000.0	$2.35\times10^{25}\pm2.17\times10^{24}$
2014-04-18	56765	2.109	1.476	97900.0	294000.0	$2.30\times10^{25}\pm2.22\times10^{24}$
2014-04-22	56769	2.161	1.468	103000.0	308000.0	$2.72\times10^{25}\pm3.00\times10^{24}$
2014-04-25	56772	2.200	1.465	106000.0	319000.0	$1.62\times10^{25}\pm2.83\times10^{24}$
2014-05-08	56785	2.369	1.478	123000.0	370000.0	$6.19\times10^{24}\pm4.16\times10^{24}$
2014-05-14	56791	2.442	1.501	131000.0	394000.0	$1.47\times10^{25}\pm3.92\times10^{24}$
2014-05-20	56797	2.520	1.539	140000.0	419000.0	$7.75\times10^{24}\pm2.89\times10^{24}$
2014-05-31	56808	2.656	1.643	155000.0	466000.0	$1.47\times10^{25}\pm2.05\times10^{24}$
2014-06-07	56815	2.743	1.735	166000.0	497000.0	$2.33\times10^{25}\pm6.21\times10^{24}$
2014-06-24	56832	2.950	2.028	191000.0	574000.0	$2.44\times10^{24}\pm2.00\times10^{24}$
2014-07-04	56842	3.067	2.235	207000.0	621000.0	$7.21\times10^{24}\pm2.55\times10^{24}$
2014-07-07	56845	3.102	2.302	212000.0	635000.0	$1.34\times10^{25}\pm3.38\times10^{24}$
2014-07-13	56851	3.176	2.448	222000.0	666000.0	$3.12\times10^{25}\pm6.20\times10^{24}$
2014-07-18	56856	3.234	2.568	230000.0	690000.0	$1.34\times10^{25}\pm1.90\times10^{24}$
2014-08-04	56873	3.430	3.004	259000.0	776000.0	$4.79\times10^{24}\pm5.35\times10^{24}$

Computed gas production rates of C_3 of comet Lovejoy						
Date	MJD	r_h	Δ	τ_0	τ_1	Q(C_3)
2013-09-12	56547	1.907	1.810	10200.0	98200.0	$4.73\times10^{24}\pm3.41\times10^{23}$
2013-09-21	56556	1.787	1.593	8940.0	86200.0	$5.61\times10^{24}\pm6.26\times10^{23}$
2013-09-29	56564	1.68	1.398	7900.0	76200.0	$6.98\times10^{24}\pm3.33\times10^{23}$
2013-10-03	56568	1.625	1.300	7390.0	71300.0	$7.59\times10^{24}\pm3.26\times10^{23}$
2013-10-05	56570	1.599	1.251	7160.0	69000.0	$7.86\times10^{24}\pm3.41\times10^{23}$
2013-10-21	56586	1.384	0.868	5360.0	51700.0	$8.40\times10^{24}\pm3.96\times10^{23}$
2013-10-24	56589	1.344	0.798	5060.0	48800.0	$1.45\times10^{25}\pm7.98\times10^{23}$
2013-10-26	56591	1.318	0.754	4860.0	46900.0	$1.36\times10^{25}\pm6.55\times10^{23}$
2013-11-02	56598	1.227	0.605	4220.0	40600.0	$1.94\times10^{25}\pm6.57\times10^{23}$
2014-02-14	56702	1.269	1.560	4510.0	43500.0	$1.44\times10^{25}\pm1.26\times10^{24}$
2014-02-21	56709	1.361	1.581	5190.0	50000.0	$1.16\times10^{25}\pm1.02\times10^{24}$
2014-03-06	56722	1.535	1.589	6600.0	63600.0	$9.41\times10^{24}\pm5.67\times10^{23}$
2014-03-13	56729	1.629	1.580	7430.0	71600.0	$8.33\times10^{24}\pm6.78\times10^{23}$
2014-03-18	56734	1.696	1.569	8050.0	77700.0	$6.73\times10^{24}\pm8.23\times10^{23}$
2014-03-26	56742	1.804	1.546	9110.0	87900.0	$7.26\times10^{24}\pm3.79\times10^{23}$
2014-04-04	56751	1.924	1.516	10400.0	99900.0	$4.77\times10^{24}\pm3.23\times10^{23}$
2014-04-10	56757	2.004	1.497	11200.0	108000.0	$5.40\times10^{24}\pm4.17\times10^{23}$
2014-04-15	56762	2.069	1.483	12000.0	116000.0	$4.65\times10^{24}\pm5.83\times10^{23}$
2014-04-19	56766	2.122	1.474	12600.0	122000.0	$3.58\times10^{24}\pm9.10\times10^{23}$
2014-04-25	56772	2.201	1.465	13600.0	131000.0	$2.80\times10^{24}\pm5.00\times10^{23}$
2014-05-27	56804	2.608	1.600	19000.0	184000.0	$2.44\times10^{24}\pm4.39\times10^{23}$
2014-05-31	56808	2.656	1.643	19800.0	190000.0	$2.30\times10^{24}\pm6.45\times10^{23}$
2014-06-07	56815	2.743	1.734	21100.0	203000.0	$1.93\times10^{24}\pm9.61\times10^{23}$

Computed gas production rates of NH of comet Lovejoy						
Date	MJD	r_h	Δ	τ_0	τ_1	Q(NH)
2013-09-20	56555	1.800	1.617	162000.0	486000.0	$1.04\times10^{25}\pm9.49\times10^{24}$
2013-09-21	56556	1.787	1.593	160000.0	479000.0	$3.84\times10^{25}\pm1.44\times10^{25}$
2013-09-26	56561	1.719	1.470	148000.0	443000.0	$5.98\times10^{25}\pm1.05\times10^{25}$
2013-09-29	56564	1.679	1.398	141000.0	423000.0	$5.62\times10^{25}\pm1.11\times10^{25}$
2013-10-04	56569	1.612	1.275	130000.0	390000.0	$7.64\times10^{25}\pm8.99\times10^{24}$
2013-10-21	56586	1.384	0.867	95800.0	287000.0	$1.28\times10^{26}\pm1.41\times10^{25}$
2013-10-24	56589	1.344	0.798	90300.0	271000.0	$1.52\times10^{26}\pm1.44\times10^{25}$
2013-10-26	56591	1.318	0.754	86900.0	261000.0	$1.54\times10^{26}\pm1.43\times10^{25}$
2013-11-03	56599	1.214	0.585	73700.0	221000.0	$2.10\times10^{26}\pm1.60\times10^{25}$
2014-02-15	56703	1.282	1.564	82200.0	247000.0	$1.34\times10^{26}\pm2.57\times10^{25}$
2014-02-21	56709	1.361	1.581	92600.0	278000.0	$1.12\times10^{26}\pm2.01\times10^{25}$
2014-03-06	56722	1.535	1.589	118000.0	353000.0	$9.73\times10^{25}\pm1.41\times10^{25}$
2014-03-13	56729	1.629	1.580	133000.0	398000.0	$8.20\times10^{25}\pm1.26\times10^{25}$
2014-03-18	56734	1.696	1.569	144000.0	431000.0	$4.68\times10^{25}\pm1.63\times10^{25}$
2014-03-26	56742	1.804	1.546	163000.0	488000.0	$5.84\times10^{25}\pm9.17\times10^{24}$
2014-04-04	56751	1.924	1.516	185000.0	555000.0	$2.67\times10^{25}\pm1.06\times10^{25}$
2014-04-16	56763	2.084	1.480	217000.0	651000.0	$1.86\times10^{25}\pm2.01\times10^{25}$
2014-04-19	56766	2.122	1.474	225000.0	675000.0	$2.64\times10^{25}\pm2.12\times10^{25}$

Computed gas production rates of OH of comet Lovejoy						
Date	MJD	r_h	Δ	τ_0	τ_1	Q(OH)
2013-09-12	56547	1.907	1.810	87300.0	582000.0	$7.02\times10^{27}\pm1.22\times10^{27}$
2013-09-20	56555	1.800	1.617	77800.0	518000.0	$5.69\times10^{27}\pm7.31\times10^{26}$
2013-09-21	56556	1.787	1.592	76600.0	511000.0	$8.44\times10^{27}\pm1.01\times10^{27}$
2013-09-26	56561	1.720	1.471	71000.0	473000.0	$1.14\times10^{28}\pm1.35\times10^{27}$
2013-10-03	56568	1.626	1.300	63500.0	423000.0	$1.12\times10^{28}\pm1.48\times10^{27}$
2013-10-05	56570	1.599	1.252	61400.0	409000.0	$1.10\times10^{28}\pm1.51\times10^{27}$
2013-10-08	56573	1.558	1.178	58300.0	388000.0	$1.28\times10^{28}\pm1.62\times10^{27}$
2013-10-10	56575	1.532	1.131	56300.0	376000.0	$1.29\times10^{28}\pm1.95\times10^{27}$
2013-10-20	56585	1.398	0.892	46900.0	313000.0	$2.15\times10^{28}\pm3.35\times10^{27}$
2013-10-21	56586	1.384	0.867	46000.0	306000.0	$2.29\times10^{28}\pm2.45\times10^{27}$
2013-10-24	56589	1.344	0.798	43400.0	289000.0	$2.58\times10^{28}\pm2.77\times10^{27}$
2013-10-26	56591	1.318	0.754	41700.0	278000.0	$2.60\times10^{28}\pm3.04\times10^{27}$
2013-11-03	56599	1.214	0.585	35400.0	236000.0	$2.95\times10^{28}\pm3.52\times10^{27}$
2014-02-13	56701	1.256	1.556	37900.0	252000.0	$1.86\times10^{28}\pm4.16\times10^{27}$
2014-02-15	56703	1.282	1.564	39400.0	263000.0	$1.50\times10^{28}\pm2.96\times10^{27}$
2014-02-21	56709	1.361	1.581	44500.0	296000.0	$1.25\times10^{28}\pm2.15\times10^{27}$
2014-03-06	56722	1.535	1.589	56500.0	377000.0	$1.17\times10^{28}\pm1.57\times10^{27}$
2014-03-13	56729	1.629	1.580	63700.0	425000.0	$1.06\times10^{28}\pm1.30\times10^{27}$
2014-03-18	56734	1.696	1.569	69000.0	460000.0	$8.41\times10^{27}\pm1.12\times10^{27}$
2014-03-26	56742	1.804	1.546	78100.0	521000.0	$8.02\times10^{27}\pm7.85\times10^{26}$
2014-04-10	56757	2.004	1.497	96400.0	643000.0	$6.00\times10^{27}\pm6.64\times10^{26}$
2014-04-15	56762	2.069	1.483	103000.0	685000.0	$4.93\times10^{27}\pm6.32\times10^{26}$
2014-04-18	56765	2.110	1.475	107000.0	712000.0	$4.68\times10^{27}\pm5.66\times10^{26}$
2014-04-22	56769	2.160	1.469	112000.0	746000.0	$4.64\times10^{27}\pm5.43\times10^{26}$
2014-04-25	56772	2.201	1.465	116000.0	775000.0	$3.27\times10^{27}\pm4.72\times10^{26}$
2014-05-14	56791	2.442	1.500	143000.0	954000.0	$5.09\times10^{26}\pm1.12\times10^{27}$
2014-05-20	56797	2.520	1.539	152000.0	1020000.0	$6.42\times10^{26}\pm4.92\times10^{26}$
2014-05-27	56804	2.608	1.600	163000.0	1090000.0	$3.54\times10^{27}\pm7.40\times10^{26}$

Computed gas production rates of water of comet Lovejoy						
Date	MJD	r_h	Δ	τ_0	τ_1	Q(H_2O)
2013-09-12	56547	1.907	1.81	87300.0	582000.0	$6.92\times10^{27}\pm1.20\times10^{27}$
2013-09-20	56555	1.8	1.617	77800.0	518000.0	$5.77\times10^{27}\pm7.41\times10^{26}$
2013-09-21	56556	1.787	1.592	76600.0	511000.0	$8.59\times10^{27}\pm1.03\times10^{27}$
2013-09-26	56561	1.72	1.471	71000.0	473000.0	$1.18\times10^{28}\pm1.40\times10^{27}$
2013-10-03	56568	1.626	1.3	63500.0	423000.0	$1.19\times10^{28}\pm1.58\times10^{27}$
2013-10-05	56570	1.599	1.252	61400.0	409000.0	$1.18\times10^{28}\pm1.62\times10^{27}$
2013-10-08	56573	1.558	1.178	58300.0	388000.0	$1.40\times10^{28}\pm1.77\times10^{27}$
2013-10-10	56575	1.532	1.131	56300.0	376000.0	$1.42\times10^{28}\pm2.15\times10^{27}$
2013-10-20	56585	1.398	0.892	46900.0	313000.0	$2.47\times10^{28}\pm3.85\times10^{27}$
2013-10-21	56586	1.384	0.867	46000.0	306000.0	$2.64\times10^{28}\pm2.84\times10^{27}$
2013-10-24	56589	1.344	0.798	43400.0	289000.0	$3.03\times10^{28}\pm3.25\times10^{27}$
2013-10-26	56591	1.318	0.754	41700.0	278000.0	$3.08\times10^{28}\pm3.61\times10^{27}$
2013-11-03	56599	1.214	0.585	35400.0	236000.0	$3.64\times10^{28}\pm4.34\times10^{27}$
2014-02-13	56701	1.256	1.556	37900.0	252000.0	$2.26\times10^{28}\pm5.05\times10^{27}$
2014-02-15	56703	1.282	1.564	39400.0	263000.0	$1.80\times10^{28}\pm3.55\times10^{27}$
2014-02-21	56709	1.361	1.581	44500.0	296000.0	$1.46\times10^{28}\pm2.50\times10^{27}$
2014-03-06	56722	1.535	1.589	56500.0	377000.0	$1.29\times10^{28}\pm1.72\times10^{27}$
2014-03-13	56729	1.629	1.58	63700.0	425000.0	$1.13\times10^{28}\pm1.38\times10^{27}$
2014-03-18	56734	1.696	1.569	69000.0	460000.0	$8.79\times10^{27}\pm1.17\times10^{27}$
2014-03-26	56742	1.804	1.546	78100.0	521000.0	$8.12\times10^{27}\pm7.96\times10^{26}$
2014-04-10	56757	2.004	1.497	96400.0	643000.0	$5.76\times10^{27}\pm6.38\times10^{26}$
2014-04-15	56762	2.069	1.483	103000.0	685000.0	$4.66\times10^{27}\pm5.98\times10^{26}$
2014-04-18	56765	2.11	1.475	107000.0	712000.0	$4.39\times10^{27}\pm5.31\times10^{26}$
2014-04-22	56769	2.16	1.469	112000.0	746000.0	$4.29\times10^{27}\pm5.03\times10^{26}$
2014-04-25	56772	2.201	1.465	116000.0	775000.0	$3.00\times10^{27}\pm4.33\times10^{26}$
2014-05-14	56791	2.442	1.5	143000.0	954000.0	$4.43\times10^{26}\pm9.72\times10^{26}$
2014-05-20	56797	2.52	1.539	152000.0	1020000.0	$5.51\times10^{26}\pm4.22\times10^{26}$
2014-05-27	56804	2.608	1.6	163000.0	1090000.0	$2.98\times10^{27}\pm6.24\times10^{26}$

Appendix B

Gas production rates ratios

This section contains the logarithmic gas abundance ratios C_2-to-CN, C_3-to-CN, and OH-to-CN of comets PanSTARRS and Lovejoy. MJD represents the date of the observation night in Modified Julian Days, while r_h represents the heliocentric distance and is expressed in AU.

B.1 Gas abundance ratios of comet PanSTARRS

Abundance ratio $\log(Q(C_2)/Q(CN)$ of comet PanSTARRS			
Date	MJD	r_h	$\log(Q(C_2)/Q(CN))$
2014-02-03	56691	3.113	0.23 ± 0.08
2014-02-07	56695	3.068	0.09 ± 0.08
2014-02-09	56697	3.046	0.05 ± 0.09
2014-02-11	56699	3.023	0.15 ± 0.07
2014-02-14	56702	2.989	0.13 ± 0.10
2014-02-20	56708	2.921	0.22 ± 0.06
2014-02-26	56714	2.853	0.13 ± 0.05
2014-03-04	56720	2.784	0.17 ± 0.05
2014-03-13	56729	2.680	0.12 ± 0.04
2014-03-23	56739	2.564	0.05 ± 0.04
2014-04-01	56748	2.458	-0.02 ± 0.06
2014-04-08	56755	2.377	-0.01 ± 0.06
2014-04-16	56763	2.283	0.10 ± 0.07
2014-04-23	56770	2.202	0.10 ± 0.06
2014-05-09	56786	2.013	0.07 ± 0.07
2014-05-18	56795	1.907	0.16 ± 0.05
2014-05-20	56797	1.884	0.12 ± 0.05
2014-06-07	56815	1.664	0.18 ± 0.03
2014-06-08	56816	1.652	0.19 ± 0.03

Abundance ratio $\log(Q(C_2)/Q(CN)$ of comet PanSTARRS			
2014-06-09	56817	1.641	0.22 ± 0.03
2014-06-14	56822	1.585	0.19 ± 0.03
2014-06-23	56831	1.486	0.24 ± 0.03
2014-07-03	56841	1.382	0.20 ± 0.04
2014-09-06	56906	1.067	0.25 ± 0.04
2014-09-07	56907	1.070	0.27 ± 0.04
2014-09-20	56920	1.126	0.26 ± 0.03
2014-09-27	56927	1.171	0.26 ± 0.02
2014-09-28	56928	1.178	0.24 ± 0.02
2014-10-06	56936	1.242	0.24 ± 0.01
2014-10-07	56937	1.250	0.24 ± 0.02
2014-10-11	56941	1.285	0.33 ± 0.01
2014-10-13	56943	1.303	0.22 ± 0.02
2014-10-13	56943	1.304	0.22 ± 0.02
2014-10-14	56944	1.313	0.31 ± 0.01
2014-10-23	56953	1.402	0.23 ± 0.02
2014-10-27	56957	1.443	0.17 ± 0.02
2014-11-07	56968	1.561	0.17 ± 0.03
2014-11-09	56970	1.585	0.11 ± 0.02
2014-11-10	56971	1.594	0.18 ± 0.02
2014-11-13	56974	1.629	0.15 ± 0.02
2014-11-13	56974	1.629	0.11 ± 0.02
2014-11-18	56979	1.685	0.11 ± 0.02
2014-11-27	56988	1.790	0.13 ± 0.02
2014-12-04	56995	1.871	0.05 ± 0.03
2014-12-15	57006	2.000	0.05 ± 0.03
2014-12-19	57010	2.047	0.06 ± 0.02
2015-01-03	57025	2.225	-0.02 ± 0.06
2015-01-09	57031	2.295	0.02 ± 0.05
2015-01-20	57042	2.425	0.22 ± 0.04
2015-01-28	57050	2.518	0.24 ± 0.07
2015-02-02	57055	2.577	0.36 ± 0.10

Abundance ratio $\log(Q(C_3)/Q(CN)$ of comet PanSTARRS			
Date	MJD	r_h	$\log(Q(C_3)/Q(CN))$
2014-02-11	56699	3.023	-2.34 ± 2.00
2014-03-23	56739	2.564	-1.05 ± 0.12
2014-04-01	56748	2.458	-1.04 ± 0.14
2014-04-08	56755	2.376	-1.11 ± 0.19
2014-05-30	56807	1.756	-0.71 ± 0.06
2014-06-07	56815	1.664	-0.69 ± 0.05
2014-06-08	56816	1.653	-0.69 ± 0.05
2014-06-09	56817	1.641	-0.64 ± 0.05
2014-09-06	56906	1.067	-0.58 ± 0.05
2014-09-20	56920	1.126	-0.59 ± 0.04
2014-09-27	56927	1.171	-0.61 ± 0.03
2014-09-28	56928	1.178	-0.56 ± 0.02
2014-10-06	56936	1.242	-0.60 ± 0.02
2014-10-07	56937	1.250	-0.56 ± 0.03
2014-10-11	56941	1.286	-0.44 ± 0.03
2014-10-13	56943	1.303	-0.59 ± 0.03
2014-10-13	56943	1.304	-0.61 ± 0.03
2014-10-14	56944	1.313	-0.52 ± 0.02
2014-10-23	56953	1.402	-0.59 ± 0.02
2014-10-27	56957	1.443	-0.60 ± 0.02
2014-11-07	56968	1.561	-0.63 ± 0.03
2014-11-10	56971	1.594	-0.63 ± 0.04
2014-11-13	56974	1.629	-0.67 ± 0.04
2014-11-13	56974	1.630	-0.69 ± 0.03
2014-11-18	56979	1.685	-0.68 ± 0.03
2014-11-27	56988	1.789	-0.67 ± 0.04
2014-11-27	56988	1.790	-0.67 ± 0.04
2014-12-04	56995	1.871	-0.75 ± 0.06
2014-12-08	56999	1.918	-0.74 ± 0.07
2014-12-15	57006	2.000	-0.72 ± 0.04
2014-12-19	57010	2.047	-0.79 ± 0.04
2015-01-03	57025	2.225	-0.93 ± 0.13

Abundance ratio $\log(Q(NH)/Q(CN)$ of comet PanSTARRS			
Date	MJD	r_h	$\log(Q(NH)/Q(CN))$
2014-04-08	56755	2.376	-0.24 ± 0.98
2014-09-06	56906	1.067	0.36 ± 0.07
2014-09-27	56927	1.171	0.36 ± 0.04
2014-09-28	56928	1.179	0.37 ± 0.03
2014-10-06	56936	1.242	0.32 ± 0.03
2014-10-07	56937	1.250	0.28 ± 0.04
2014-10-11	56941	1.286	0.33 ± 0.03
2014-10-13	56943	1.304	0.19 ± 0.06
2014-10-14	56944	1.313	0.31 ± 0.03
2014-10-23	56953	1.402	0.17 ± 0.04
2014-10-27	56957	1.443	0.12 ± 0.04
2014-11-09	56970	1.585	-0.14 ± 0.15
2014-11-10	56971	1.594	-0.05 ± 0.12
2014-11-13	56974	1.629	-0.15 ± 0.14
2014-11-13	56974	1.630	-0.17 ± 0.19
2014-11-18	56979	1.686	-0.17 ± 0.09
2014-11-27	56988	1.789	-0.09 ± 0.10
2014-12-04	56995	1.871	-1.76 ± 6.20
2014-12-06	56997	1.895	-0.56 ± 0.65
2014-12-08	56999	1.918	-1.12 ± 1.27
2014-12-15	57006	2.000	-0.67 ± 0.37
2014-12-19	57010	2.046	-2.56 ± 6.71

Abundance ratio $\log(Q(OH)/Q(CN)$ of comet PanSTARRS			
Date	MJD	r_h	$\log(Q(OH)/Q(CN))$
2014-03-23	56739	2.563	2.65 ± 0.14
2014-06-14	56822	1.585	2.72 ± 0.15
2014-06-29	56837	1.423	2.77 ± 0.14
2014-09-06	56906	1.067	2.40 ± 0.16
2014-09-07	56907	1.070	2.31 ± 0.14
2014-09-20	56920	1.126	2.42 ± 0.10
2014-09-27	56927	1.171	2.48 ± 0.06
2014-09-28	56928	1.179	2.49 ± 0.06
2014-10-06	56936	1.242	2.63 ± 0.05
2014-10-07	56937	1.250	2.57 ± 0.06
2014-10-11	56941	1.286	2.84 ± 0.04
2014-10-13	56943	1.304	2.73 ± 0.05
2014-10-14	56944	1.313	2.75 ± 0.04
2014-10-23	56953	1.402	2.71 ± 0.04
2014-10-27	56957	1.443	2.72 ± 0.04
2014-11-09	56970	1.585	2.75 ± 0.05
2014-11-13	56974	1.629	2.72 ± 0.05
2014-11-13	56974	1.630	2.69 ± 0.06
2014-11-18	56979	1.686	2.68 ± 0.05
2014-11-27	56988	1.789	2.68 ± 0.05
2014-12-04	56995	1.871	2.69 ± 0.05
2014-12-06	56997	1.895	2.72 ± 0.08
2014-12-08	56999	1.917	2.62 ± 0.06
2014-12-15	57006	2.000	2.59 ± 0.06
2014-12-19	57010	2.046	2.62 ± 0.05
2015-01-03	57025	2.224	2.46 ± 0.09
2015-01-09	57031	2.295	2.45 ± 0.09

B.2 Gas abundance ratios of comet Lovejoy

Abundance ratio $\log(Q(C_2)/Q(CN)$ of comet Lovejoy			
Date	MJD	r_h	$\log(Q(C_2)/Q(CN))$
2013-09-12	56547	1.907	-0.08 ± 0.03
2013-09-16	56551	1.853	-0.06 ± 0.03
2013-09-21	56556	1.788	-0.02 ± 0.04
2013-09-25	56560	1.733	0.05 ± 0.02
2013-09-29	56564	1.680	0.06 ± 0.03
2013-10-03	56568	1.625	0.03 ± 0.02
2013-10-08	56573	1.558	0.07 ± 0.02
2013-10-10	56575	1.531	0.05 ± 0.03
2013-10-20	56585	1.398	0.11 ± 0.03
2013-10-21	56586	1.384	0.07 ± 0.02
2013-10-24	56589	1.344	0.12 ± 0.02
2013-10-26	56591	1.319	0.12 ± 0.03
2013-11-02	56598	1.228	0.17 ± 0.02
2014-02-13	56701	1.256	0.19 ± 0.03
2014-02-15	56703	1.282	0.19 ± 0.03
2014-02-21	56709	1.361	0.16 ± 0.03
2014-02-22	56710	1.374	0.20 ± 0.02
2014-03-06	56722	1.534	0.13 ± 0.02
2014-03-13	56729	1.629	0.11 ± 0.02
2014-03-18	56734	1.696	0.09 ± 0.03
2014-03-25	56741	1.790	0.08 ± 0.03
2014-03-26	56742	1.803	0.03 ± 0.02
2014-04-04	56751	1.924	0.04 ± 0.03
2014-04-10	56757	2.003	-0.02 ± 0.03
2014-04-14	56761	2.057	0.00 ± 0.06
2014-04-18	56765	2.109	-0.02 ± 0.05
2014-04-22	56769	2.161	0.02 ± 0.05
2014-04-25	56772	2.200	-0.15 ± 0.08
2014-05-08	56785	2.369	-0.45 ± 0.30
2014-05-14	56791	2.442	-0.09 ± 0.13
2014-05-20	56797	2.520	0.02 ± 0.19
2014-05-31	56808	2.656	-0.01 ± 0.07
2014-06-07	56815	2.743	0.26 ± 0.13
2014-06-24	56832	2.950	-0.47 ± 0.36
2014-07-04	56842	3.067	-0.11 ± 0.19
2014-07-07	56845	3.102	0.25 ± 0.15
2014-07-18	56856	3.234	0.45 ± 0.14

Abundance ratio $\log(Q(C_2)/Q(CN)$ of comet Lovejoy			
2014-08-04	56873	3.430	0.47 ± 0.83

Abundance ratio $\log(Q(C_3)/Q(CN)$ of comet Lovejoy			
Date	MJD	r_h	$\log(Q(C_3)/Q(CN))$
2013-09-21	56556	1.787	-0.73 ± 0.05
2013-09-29	56564	1.680	-0.71 ± 0.03
2013-10-03	56568	1.625	-0.69 ± 0.02
2013-10-05	56570	1.599	-0.71 ± 0.02
2013-10-21	56586	1.384	-0.84 ± 0.03
2013-10-24	56589	1.344	-0.65 ± 0.03
2013-10-26	56591	1.318	-0.68 ± 0.03
2013-11-02	56598	1.227	-0.62 ± 0.02
2014-02-14	56702	1.269	-0.65 ± 0.04
2014-02-21	56709	1.361	-0.66 ± 0.04
2014-03-06	56722	1.535	-0.69 ± 0.03
2014-03-13	56729	1.629	-0.68 ± 0.04
2014-03-18	56734	1.696	-0.71 ± 0.06
2014-03-26	56742	1.804	-0.69 ± 0.03
2014-04-04	56751	1.924	-0.76 ± 0.03
2014-04-10	56757	2.004	-0.75 ± 0.04
2014-04-15	56762	2.069	-0.70 ± 0.07
2014-04-19	56766	2.122	-0.83 ± 0.11
2014-04-25	56772	2.201	-0.91 ± 0.08
2014-05-27	56804	2.608	-0.77 ± 0.10
2014-05-31	56808	2.656	-0.82 ± 0.13
2014-06-07	56815	2.743	-0.82 ± 0.23

Abundance ratio $\log(Q(NH)/Q(CN)$ of comet Lovejoy			
Date	MJD	r_h	$\log(Q(NH)/Q(CN))$
2013-09-20	56555	1.800	-0.46 ± 0.40
2013-09-21	56556	1.787	0.11 ± 0.16
2013-09-29	56564	1.679	0.19 ± 0.09
2013-10-04	56569	1.612	0.29 ± 0.05
2013-10-21	56586	1.384	0.34 ± 0.05
2013-10-24	56589	1.344	0.37 ± 0.04
2013-10-26	56591	1.318	0.38 ± 0.04
2014-02-15	56703	1.282	0.32 ± 0.09
2014-02-21	56709	1.361	0.32 ± 0.08
2014-03-06	56722	1.535	0.32 ± 0.06
2014-03-13	56729	1.629	0.31 ± 0.07
2014-03-18	56734	1.696	0.13 ± 0.15
2014-03-26	56742	1.804	0.21 ± 0.07
2014-04-04	56751	1.924	-0.01 ± 0.17
2014-04-19	56766	2.122	0.04 ± 0.35

Abundance ratio $\log(Q(OH)/Q(CN)$ of comet Lovejoy			
Date	MJD	r_h	$\log(Q(OH)/Q(CN))$
2013-09-20	56555	1.800	2.28 ± 0.06
2013-09-21	56556	1.787	2.45 ± 0.06
2013-10-03	56568	1.626	2.48 ± 0.06
2013-10-05	56570	1.599	2.44 ± 0.06
2013-10-08	56573	1.558	2.57 ± 0.06
2013-10-10	56575	1.532	2.45 ± 0.07
2013-10-20	56585	1.398	2.62 ± 0.07
2013-10-21	56586	1.384	2.59 ± 0.05
2013-10-24	56589	1.344	2.60 ± 0.05
2013-10-26	56591	1.318	2.60 ± 0.05
2014-02-13	56701	1.256	2.38 ± 0.10
2014-02-15	56703	1.282	2.44 ± 0.09
2014-02-21	56709	1.361	2.37 ± 0.08
2014-03-06	56722	1.535	2.40 ± 0.06
2014-03-13	56729	1.629	2.42 ± 0.06
2014-03-18	56734	1.696	2.39 ± 0.06
2014-03-26	56742	1.804	2.35 ± 0.04
2014-04-10	56757	2.004	2.30 ± 0.05
2014-04-15	56762	2.069	2.32 ± 0.07
2014-04-18	56765	2.110	2.29 ± 0.06
2014-04-22	56769	2.160	2.25 ± 0.05
2014-04-25	56772	2.201	2.16 ± 0.07
2014-05-14	56791	2.442	1.45 ± 0.95
2014-05-20	56797	2.520	1.93 ± 0.35
2014-05-27	56804	2.608	2.39 ± 0.11

Appendix C

Computed $Af\rho$ parameter

This section presents the computed $Af\rho$ parameter in the R, RC, BC, and GC filters. The date of each observation is given in Modified Julian Days (MJD). The heliocentric distance r_h and geocentric distance Δ are expressed in AU, and the corresponding phase angle is also provided. The $Af\rho$ values, both uncorrected and corrected for phase angle, are expressed in centimeters.

C.1 $Af\rho$ of comet PanSTARRS

Computed $Af\rho$ parameter in the R filter of comet PanSTARRS						
Date	MJD	r_h	Δ	$Af\rho$	angle	corrected $Af\rho$
2013-03-28	56379	6.21	5.91	2948 ± 56	9.02	4150 ± 79
2013-03-28	56379	6.21	5.91	3076 ± 68	9.02	4330 ± 96
2013-03-28	56379	6.21	5.91	3001 ± 61	9.02	4225 ± 86
2013-03-28	56379	6.21	5.91	2765 ± 47	9.02	3893 ± 66
2013-03-28	56379	6.21	5.91	3032 ± 63	9.02	4269 ± 89
2013-03-30	56381	6.19	5.86	3376 ± 76	8.99	4748 ± 107
2013-03-30	56381	6.19	5.86	2957 ± 48	8.99	4159 ± 68
2013-03-30	56381	6.19	5.86	3138 ± 40	8.99	4413 ± 56
2013-03-30	56381	6.19	5.86	3041 ± 54	8.99	4278 ± 76
2013-04-06	56388	6.13	5.71	3008 ± 30	8.82	4206 ± 42
2013-04-06	56388	6.13	5.71	3086 ± 37	8.82	4315 ± 52
2013-04-06	56388	6.13	5.71	2877 ± 30	8.82	4023 ± 42
2013-04-13	56395	6.07	5.56	2797 ± 29	8.58	3878 ± 40
2013-04-13	56395	6.07	5.56	2971 ± 28	8.58	4119 ± 39
2013-04-13	56395	6.07	5.56	3038 ± 45	8.58	4212 ± 63
2013-04-13	56395	6.07	5.56	3022 ± 24	8.58	4190 ± 33
2013-04-20	56402	6.00	5.42	3060 ± 32	8.27	4197 ± 43
2013-04-20	56402	6.00	5.42	3032 ± 29	8.27	4160 ± 40

Computed $Af\rho$ parameter in the R filter of comet PanSTARRS (continued)						
2013-04-20	56402	6.00	5.42	3025 ± 27	8.27	4150 ± 37
2013-04-20	56402	6.00	5.42	2963 ± 33	8.27	4065 ± 45
2013-04-26	56408	5.95	5.31	2611 ± 78	7.97	3546 ± 106
2013-04-26	56408	5.95	5.31	2407 ± 61	7.97	3269 ± 83
2013-04-26	56408	5.95	5.31	2426 ± 95	7.97	3295 ± 129
2013-04-26	56408	5.95	5.31	2148 ± 86	7.97	2917 ± 116
2013-05-03	56415	5.88	5.19	3124 ± 38	7.62	4189 ± 51
2013-05-03	56415	5.88	5.19	3077 ± 37	7.62	4126 ± 50
2013-05-03	56415	5.88	5.19	2846 ± 29	7.62	3816 ± 39
2013-05-03	56415	5.88	5.19	3034 ± 37	7.62	4068 ± 49
2013-05-07	56419	5.85	5.13	3239 ± 40	7.44	4313 ± 53
2013-05-10	56422	5.82	5.09	2878 ± 28	7.31	3816 ± 37
2013-05-10	56422	5.82	5.09	2542 ± 28	7.31	3371 ± 38
2013-05-10	56422	5.82	5.09	2727 ± 31	7.31	3616 ± 42
2013-05-10	56422	5.82	5.09	2745 ± 32	7.31	3640 ± 42
2013-05-16	56428	5.77	5.00	3099 ± 33	7.10	4079 ± 44
2013-05-16	56428	5.77	5.00	3140 ± 32	7.10	4134 ± 42
2013-05-16	56428	5.77	5.00	3024 ± 31	7.10	3980 ± 41
2013-05-16	56428	5.77	5.00	3037 ± 32	7.10	3998 ± 42
2013-05-21	56433	5.72	4.95	3123 ± 32	7.00	4097 ± 42
2013-05-21	56433	5.72	4.95	3264 ± 38	7.00	4282 ± 50
2013-05-21	56433	5.72	4.95	2913 ± 34	7.00	3821 ± 45
2013-05-21	56433	5.72	4.95	3066 ± 35	7.00	4022 ± 45
2013-05-22	56434	5.71	4.93	3168 ± 47	6.99	4154 ± 61
2013-05-22	56434	5.71	4.93	2985 ± 43	6.99	3914 ± 56
2013-05-22	56434	5.71	4.93	3181 ± 39	6.99	4171 ± 51
2013-05-22	56434	5.71	4.93	3165 ± 36	6.99	4151 ± 47
2013-05-29	56441	5.65	4.86	2929 ± 42	7.02	3845 ± 55
2013-05-29	56441	5.65	4.86	2893 ± 33	7.02	3797 ± 43
2013-05-29	56441	5.65	4.86	2991 ± 33	7.02	3926 ± 43
2013-05-29	56441	5.65	4.86	2947 ± 43	7.02	3868 ± 57
2013-06-07	56450	5.57	4.79	3315 ± 25	7.33	4399 ± 34
2013-06-07	56450	5.57	4.79	3239 ± 28	7.33	4299 ± 38
2013-06-07	56450	5.56	4.79	3182 ± 26	7.33	4222 ± 34
2013-06-07	56450	5.56	4.79	3184 ± 27	7.33	4225 ± 36
2013-06-22	56465	5.42	4.73	3148 ± 74	8.39	4336 ± 103
2013-07-08	56481	5.28	4.73	3003 ± 31	9.83	4344 ± 44
2013-07-08	56481	5.28	4.73	2845 ± 25	9.83	4116 ± 37
2013-07-08	56481	5.28	4.73	2870 ± 23	9.83	4151 ± 34
2013-07-08	56481	5.28	4.73	2975 ± 25	9.83	4304 ± 36
2013-07-12	56485	5.24	4.73	2890 ± 25	10.17	4230 ± 37
2013-07-16	56489	5.20	4.74	3081 ± 26	10.49	4557 ± 39

Computed $Af\rho$ parameter in the R filter of comet PanSTARRS (continued)						
2013-07-19	56492	5.17	4.75	3107 ± 56	10.72	4630 ± 83
2013-08-01	56505	5.05	4.80	3012 ± 31	11.49	4602 ± 47
2013-08-01	56505	5.05	4.80	2960 ± 30	11.49	4523 ± 46
2013-08-01	56505	5.04	4.80	2974 ± 31	11.49	4545 ± 48
2013-08-01	56505	5.04	4.80	3024 ± 28	11.49	4621 ± 43
2013-08-14	56518	4.92	4.87	2837 ± 29	11.87	4388 ± 46
2013-08-14	56518	4.91	4.87	3219 ± 46	11.87	4980 ± 71
2013-08-14	56518	4.91	4.87	2987 ± 43	11.87	4620 ± 66
2013-08-14	56518	4.91	4.87	3169 ± 44	11.87	4902 ± 68
2013-08-14	56518	4.91	4.87	3002 ± 30	11.87	4645 ± 47
2013-08-18	56522	4.88	4.89	3015 ± 34	11.90	4670 ± 53
2013-08-18	56522	4.88	4.89	2820 ± 40	11.90	4368 ± 61
2013-08-18	56522	4.88	4.89	2959 ± 38	11.90	4582 ± 58
2013-08-18	56522	4.88	4.89	2903 ± 46	11.90	4496 ± 71
2013-08-20	56524	4.86	4.90	2990 ± 34	11.90	4630 ± 52
2013-08-20	56524	4.86	4.90	3047 ± 33	11.90	4719 ± 51
2013-08-20	56524	4.86	4.90	3244 ± 41	11.90	5023 ± 63
2013-08-20	56524	4.86	4.90	3153 ± 33	11.90	4884 ± 52
2013-09-12	56547	4.62	5.00	3383 ± 43	11.22	5126 ± 65
2013-09-12	56547	4.62	5.00	3282 ± 43	11.22	4973 ± 65
2013-09-12	56547	4.62	5.00	3190 ± 38	11.22	4833 ± 58
2013-09-12	56547	4.62	5.00	3260 ± 41	11.22	4939 ± 62
2014-02-03	56691	3.11	3.24	2845 ± 36	17.65	5221 ± 66
2014-02-05	56693	3.09	3.19	2876 ± 37	17.93	5321 ± 69
2014-02-06	56694	3.08	3.16	2914 ± 37	18.07	5409 ± 69
2014-02-07	56695	3.07	3.13	2892 ± 37	18.21	5388 ± 68
2014-02-08	56696	3.06	3.11	2835 ± 35	18.34	5301 ± 65
2014-02-09	56697	3.05	3.08	2734 ± 32	18.47	5130 ± 61
2014-02-10	56698	3.04	3.05	2826 ± 32	18.60	5321 ± 60
2014-02-11	56699	3.02	3.03	2906 ± 39	18.73	5489 ± 75
2014-02-14	56702	2.99	2.95	2757 ± 35	19.09	5258 ± 67
2014-02-15	56703	2.98	2.92	2622 ± 34	19.21	5015 ± 66
2014-02-16	56704	2.97	2.89	2672 ± 37	19.32	5127 ± 71
2014-02-17	56705	2.96	2.87	2826 ± 49	19.43	5437 ± 95
2014-02-19	56707	2.93	2.81	2740 ± 27	19.63	5299 ± 53
2014-02-20	56708	2.92	2.79	2606 ± 27	19.73	5052 ± 52
2014-02-21	56709	2.91	2.76	2709 ± 35	19.83	5265 ± 69
2014-02-23	56711	2.89	2.71	2789 ± 35	20.01	5446 ± 69
2014-02-26	56714	2.85	2.62	2726 ± 26	20.25	5355 ± 51
2014-03-01	56717	2.82	2.54	2786 ± 31	20.46	5501 ± 61
2014-03-04	56720	2.78	2.46	2645 ± 27	20.62	5245 ± 54
2014-03-13	56729	2.68	2.23	2622 ± 23	20.90	5234 ± 47

Computed $Af\rho$ parameter in the R filter of comet PanSTARRS (continued)						
2014-03-16	56732	2.65	2.16	2593 ± 27	20.92	5180 ± 54
2014-03-17	56733	2.63	2.13	2601 ± 29	20.91	5194 ± 57
2014-03-23	56739	2.56	2.00	2565 ± 27	20.85	5114 ± 54
2014-03-24	56740	2.55	1.97	2543 ± 25	20.83	5068 ± 50
2014-04-01	56748	2.46	1.81	2571 ± 27	20.69	5107 ± 54
2014-04-08	56755	2.38	1.68	2666 ± 32	20.79	5308 ± 64
2014-04-16	56763	2.28	1.57	2612 ± 50	21.56	5298 ± 102
2014-04-22	56769	2.21	1.52	2574 ± 48	22.80	5376 ± 101
2014-04-23	56770	2.20	1.51	2534 ± 54	23.06	5324 ± 114
2014-05-01	56778	2.11	1.48	2511 ± 59	25.66	5584 ± 130
2014-05-06	56783	2.05	1.47	2317 ± 57	27.56	5350 ± 132
2014-05-09	56786	2.01	1.48	2278 ± 56	28.71	5376 ± 132
2014-05-18	56795	1.91	1.52	2103 ± 44	31.85	5233 ± 110
2014-05-19	56796	1.88	1.54	2116 ± 41	32.15	5289 ± 102
2014-05-30	56807	1.76	1.64	2004 ± 32	34.41	5176 ± 83
2014-05-30	56807	1.76	1.64	2000 ± 31	34.41	5167 ± 81
2014-05-31	56808	1.75	1.64	2148 ± 44	34.52	5557 ± 114
2014-06-05	56813	1.69	1.71	2133 ± 31	34.77	5538 ± 81
2014-06-07	56815	1.66	1.73	2082 ± 33	34.74	5403 ± 85
2014-06-07	56815	1.66	1.73	2081 ± 33	34.74	5401 ± 85
2014-06-08	56816	1.65	1.74	2111 ± 32	34.71	5475 ± 83
2014-06-08	56816	1.65	1.74	2095 ± 33	34.71	5433 ± 86
2014-06-09	56817	1.64	1.75	2043 ± 28	34.65	5296 ± 74
2014-06-09	56817	1.64	1.76	2060 ± 35	34.65	5339 ± 91
2014-06-23	56831	1.49	1.92	2248 ± 45	32.02	5609 ± 113
2014-06-29	56837	1.42	1.98	2365 ± 51	29.89	5698 ± 123
2014-07-03	56841	1.38	2.01	2477 ± 53	28.14	5786 ± 124
2014-09-06	56906	1.07	1.82	2299 ± 58	27.62	5315 ± 135
2014-09-06	56906	1.07	1.82	2393 ± 58	27.62	5533 ± 135
2014-09-07	56907	1.07	1.80	2523 ± 64	28.58	5941 ± 151
2014-09-07	56907	1.07	1.80	2501 ± 61	28.58	5889 ± 144
2014-09-20	56920	1.13	1.56	1824 ± 32	39.55	4997 ± 88
2014-09-20	56920	1.13	1.56	1836 ± 30	39.55	5031 ± 83
2014-09-27	56927	1.17	1.43	1553 ± 24	43.91	4423 ± 68
2014-09-27	56927	1.17	1.42	1601 ± 20	43.91	4558 ± 58
2014-09-28	56928	1.18	1.40	1574 ± 18	44.42	4499 ± 51
2014-09-28	56928	1.18	1.40	1572 ± 16	44.42	4495 ± 47
2014-10-06	56936	1.24	1.25	1559 ± 13	47.32	4543 ± 39
2014-10-06	56936	1.24	1.25	1559 ± 12	47.32	4542 ± 36
2014-10-06	56936	1.24	1.25	1549 ± 13	47.32	4511 ± 37
2014-10-07	56937	1.25	1.23	1573 ± 24	47.52	4588 ± 71
2014-10-07	56937	1.25	1.23	1581 ± 19	47.52	4611 ± 57

Computed $Af\rho$ parameter in the R filter of comet PanSTARRS (continued)						
2014-10-11	56941	1.28	1.15	1463 ± 18	47.93	4276 ± 53
2014-10-11	56941	1.28	1.15	1469 ± 21	47.93	4292 ± 62
2014-10-13	56943	1.30	1.12	1441 ± 22	47.90	4210 ± 63
2014-10-13	56943	1.30	1.12	1433 ± 29	47.90	4187 ± 84
2014-10-29	56959	1.47	0.95	1256 ± 18	42.45	3529 ± 49
2014-11-04	56965	1.53	0.96	1258 ± 15	39.37	3441 ± 41
2014-11-06	56967	1.55	0.97	1288 ± 12	38.44	3490 ± 33
2014-11-07	56968	1.56	0.98	1279 ± 16	38.01	3451 ± 44
2014-11-09	56970	1.58	1.00	1279 ± 14	37.21	3421 ± 37
2014-11-10	56971	1.59	1.01	1100 ± 12	36.85	2929 ± 33
2014-11-13	56974	1.63	1.05	1238 ± 9	35.89	3261 ± 24
2014-11-13	56974	1.63	1.05	1243 ± 11	35.89	3275 ± 28
2014-11-15	56976	1.65	1.09	1170 ± 11	35.34	3061 ± 28
2014-11-18	56979	1.69	1.14	1209 ± 8	34.65	3134 ± 21
2014-11-19	56980	1.70	1.16	1245 ± 11	34.44	3218 ± 30
2014-11-27	56988	1.79	1.34	1188 ± 10	33.00	3009 ± 25
2014-11-27	56988	1.79	1.34	1176 ± 10	33.00	2977 ± 25
2014-12-04	56995	1.87	1.52	1162 ± 14	31.74	2887 ± 36
2014-12-04	56995	1.87	1.52	1150 ± 12	31.74	2857 ± 30
2014-12-06	56997	1.90	1.57	1164 ± 14	31.35	2873 ± 34
2014-12-08	56999	1.92	1.63	1167 ± 13	30.94	2863 ± 32
2014-12-08	56999	1.92	1.63	1165 ± 15	30.94	2859 ± 36
2014-12-15	57006	2.00	1.83	1130 ± 8	29.40	2700 ± 19
2014-12-15	57006	2.00	1.83	1130 ± 11	29.40	2700 ± 26
2014-12-19	57010	2.05	1.94	1175 ± 12	28.43	2758 ± 28
2014-12-19	57010	2.05	1.94	1194 ± 9	28.43	2804 ± 20
2015-01-03	57025	2.22	2.38	1182 ± 10	24.39	2559 ± 22
2015-01-09	57031	2.29	2.55	1205 ± 9	22.66	2510 ± 19
2015-01-20	57042	2.42	2.85	1239 ± 11	19.44	2384 ± 22
2015-01-29	57051	2.53	3.08	1205 ± 13	16.82	2162 ± 24
2015-01-29	57051	2.53	3.08	1190 ± 14	16.82	2135 ± 25
2015-01-29	57051	2.53	3.08	1258 ± 15	16.82	2256 ± 27
2015-02-12	57065	2.69	3.41	1216 ± 17	12.93	1945 ± 28
2015-02-12	57065	2.69	3.41	1206 ± 18	12.93	1930 ± 29
2015-02-12	57065	2.69	3.41	1259 ± 20	12.93	2014 ± 32
2015-02-12	57065	2.69	3.41	1231 ± 23	12.93	1969 ± 37
2015-05-18	57160	3.75	4.25	1060 ± 14	12.60	1678 ± 22
2015-05-18	57160	3.75	4.25	1009 ± 13	12.60	1597 ± 20
2015-05-31	57173	3.89	4.20	990 ± 21	13.70	1622 ± 34
2015-05-31	57173	3.89	4.20	946 ± 14	13.70	1550 ± 24
2015-05-31	57173	3.89	4.20	980 ± 18	13.70	1605 ± 29
2015-06-06	57179	3.95	4.16	1072 ± 16	14.03	1773 ± 27

Computed $Af\rho$ parameter in the R filter of comet PanSTARRS (continued)						
2015-06-06	57179	3.95	4.16	1016 ± 13	14.03	1681 ± 21
2015-06-06	57179	3.95	4.16	1052 ± 14	14.03	1740 ± 23
2015-06-11	57184	4.00	4.13	968 ± 15	14.20	1610 ± 25
2015-06-11	57184	4.00	4.13	962 ± 12	14.20	1600 ± 19
2015-06-18	57191	4.08	4.09	868 ± 10	14.29	1447 ± 17
2015-06-18	57191	4.08	4.09	861 ± 11	14.29	1435 ± 19
2015-06-18	57191	4.08	4.09	871 ± 10	14.29	1452 ± 17
2015-07-07	57210	4.27	3.96	918 ± 16	13.53	1495 ± 25
2015-07-07	57210	4.27	3.96	923 ± 22	13.53	1504 ± 35
2015-07-07	57210	4.27	3.96	913 ± 33	13.53	1487 ± 53
2015-07-17	57220	4.37	3.90	879 ± 12	12.52	1388 ± 19
2015-07-17	57220	4.37	3.90	858 ± 9	12.52	1355 ± 14
2015-07-17	57220	4.37	3.90	924 ± 8	12.52	1460 ± 13
2015-08-14	57248	4.66	3.83	884 ± 11	7.95	1200 ± 14
2015-08-14	57248	4.66	3.83	847 ± 12	7.95	1149 ± 17
2015-08-24	57258	4.75	3.85	931 ± 10	6.19	1186 ± 13
2015-08-24	57258	4.75	3.85	934 ± 10	6.19	1189 ± 12
2015-08-24	57258	4.75	3.85	899 ± 7	6.19	1145 ± 9
2015-08-26	57260	4.77	3.86	938 ± 24	5.89	1182 ± 30
2015-08-27	57261	4.78	3.87	910 ± 15	5.74	1140 ± 19
2015-08-27	57261	4.78	3.87	934 ± 14	5.74	1170 ± 17
2015-08-27	57261	4.78	3.87	932 ± 14	5.74	1168 ± 18
2015-09-01	57266	4.83	3.90	944 ± 23	5.14	1156 ± 28
2015-09-01	57266	4.83	3.90	1009 ± 33	5.14	1237 ± 41
2015-09-01	57266	4.83	3.90	977 ± 28	5.14	1197 ± 34
2015-09-04	57269	4.86	3.92	900 ± 16	4.90	1093 ± 19
2015-09-04	57269	4.86	3.92	944 ± 14	4.90	1146 ± 16
2015-09-13	57278	4.95	4.01	906 ± 10	4.83	1097 ± 12
2015-09-13	57278	4.95	4.01	909 ± 7	4.83	1101 ± 9
2015-09-13	57278	4.95	4.01	939 ± 12	4.83	1137 ± 14
2015-09-18	57283	5.00	4.08	842 ± 14	5.17	1032 ± 17
2015-09-18	57283	5.00	4.08	909 ± 10	5.17	1115 ± 13
2015-09-18	57283	5.00	4.08	856 ± 10	5.17	1050 ± 13
2015-09-30	57295	5.11	4.27	819 ± 48	6.57	1058 ± 61
2015-09-30	57295	5.11	4.27	819 ± 54	6.57	1057 ± 69
2015-09-30	57295	5.11	4.27	851 ± 43	6.57	1098 ± 56
2015-10-03	57298	5.14	4.32	722 ± 25	6.96	945 ± 33
2015-10-03	57298	5.14	4.33	591 ± 31	6.96	775 ± 40
2015-10-27	57322	5.37	4.84	636 ± 42	9.47	909 ± 60
2015-10-27	57322	5.37	4.84	584 ± 65	9.47	835 ± 93
2015-11-05	57331	5.45	5.07	633 ± 44	9.96	920 ± 64
2015-11-05	57331	5.45	5.07	616 ± 42	9.96	895 ± 61

Computed $Af\rho$ parameter in the R filter of comet PanSTARRS (continued)						
2015-11-05	57331	5.45	5.07	579 ± 41	9.96	841 ± 60
2015-11-08	57334	5.48	5.14	633 ± 17	10.06	923 ± 24
2015-11-08	57334	5.48	5.14	607 ± 17	10.06	885 ± 24
2015-11-08	57334	5.48	5.14	635 ± 18	10.06	926 ± 27
2015-11-13	57339	5.53	5.27	602 ± 20	10.16	881 ± 29
2015-11-13	57339	5.53	5.27	590 ± 32	10.16	864 ± 46
2015-11-13	57339	5.53	5.27	652 ± 29	10.16	954 ± 42
2015-11-18	57344	5.57	5.40	582 ± 17	10.18	852 ± 25
2015-11-18	57344	5.57	5.40	631 ± 21	10.18	924 ± 30
2015-11-18	57344	5.57	5.40	639 ± 24	10.18	935 ± 35
2015-12-06	57362	5.74	5.88	609 ± 20	9.65	876 ± 28
2015-12-06	57362	5.74	5.88	537 ± 20	9.65	772 ± 28
2015-12-06	57362	5.74	5.88	550 ± 23	9.65	791 ± 33
2015-12-08	57364	5.76	5.93	540 ± 22	9.54	774 ± 32
2015-12-08	57364	5.76	5.93	490 ± 29	9.54	703 ± 41
2015-12-08	57364	5.76	5.93	564 ± 40	9.54	807 ± 57
2015-12-14	57370	5.81	6.08	605 ± 27	9.16	856 ± 39
2015-12-14	57370	5.81	6.08	586 ± 29	9.16	829 ± 41
2015-12-14	57370	5.81	6.08	618 ± 29	9.16	874 ± 41

Computed $Af\rho$ parameter in the RC filter of comet PanSTARRS						
Date	MJD	r_h	Δ	$Af\rho$	angle	corrected $Af\rho$)
2013-06-22	56465	5.42	4.73	3052 ± 108	8.39	4205 ± 149
2013-07-12	56485	5.24	4.73	3093 ± 28	10.17	4526 ± 41
2013-08-14	56518	4.92	4.87	3102 ± 29	11.87	4799 ± 44
2013-08-19	56523	4.87	4.89	2891 ± 47	11.90	4477 ± 72
2014-02-05	56693	3.09	3.19	3083 ± 22	17.93	5703 ± 41
2014-02-07	56695	3.07	3.13	2943 ± 25	18.21	5484 ± 47
2014-02-08	56696	3.06	3.11	3009 ± 30	18.34	5627 ± 56
2014-02-10	56698	3.03	3.05	3050 ± 25	18.60	5743 ± 47
2014-02-16	56704	2.97	2.89	2861 ± 29	19.32	5489 ± 55
2014-02-23	56711	2.89	2.70	2827 ± 24	20.01	5521 ± 46
2014-03-01	56717	2.82	2.54	2816 ± 28	20.46	5560 ± 55
2014-03-17	56733	2.63	2.13	2513 ± 34	20.91	5020 ± 67
2014-03-23	56739	2.56	2.00	2688 ± 28	20.85	5360 ± 57
2014-04-01	56748	2.46	1.81	2707 ± 23	20.69	5376 ± 45
2014-04-08	56755	2.38	1.68	2827 ± 23	20.79	5630 ± 46
2014-04-16	56763	2.28	1.57	2699 ± 54	21.56	5475 ± 109
2014-04-22	56769	2.21	1.52	2716 ± 34	22.80	5672 ± 71
2014-05-01	56778	2.11	1.48	2296 ± 28	25.66	5105 ± 63
2014-05-06	56783	2.05	1.47	2117 ± 28	27.56	4890 ± 65
2014-05-09	56786	2.01	1.48	2030 ± 28	28.71	4791 ± 65
2014-05-18	56795	1.91	1.52	2255 ± 29	31.85	5611 ± 72
2014-06-07	56815	1.66	1.73	2181 ± 23	34.74	5660 ± 61
2014-06-08	56816	1.65	1.74	2180 ± 20	34.71	5654 ± 52
2014-06-23	56831	1.49	1.92	2319 ± 23	32.02	5787 ± 58
2014-09-06	56906	1.07	1.82	2298 ± 31	27.62	5314 ± 72
2014-09-20	56920	1.13	1.56	1813 ± 29	39.55	4967 ± 79
2014-09-27	56927	1.17	1.42	1599 ± 14	43.91	4553 ± 39
2014-09-28	56928	1.18	1.40	1566 ± 13	44.42	4477 ± 36
2014-10-06	56936	1.24	1.25	1591 ± 17	47.32	4636 ± 50
2014-10-07	56937	1.25	1.23	1578 ± 15	47.52	4602 ± 44
2014-10-11	56941	1.28	1.15	1514 ± 16	47.93	4424 ± 48
2014-10-13	56943	1.30	1.12	1471 ± 30	47.90	4297 ± 87
2014-10-23	56953	1.40	0.99	1315 ± 14	45.37	3787 ± 41
2014-10-27	56957	1.44	0.96	1337 ± 21	43.48	3794 ± 60
2014-11-07	56968	1.56	0.98	1339 ± 15	38.01	3613 ± 41
2014-11-10	56971	1.59	1.01	1298 ± 26	36.85	3457 ± 68
2014-11-13	56974	1.63	1.05	1274 ± 12	35.89	3354 ± 31
2014-11-13	56974	1.63	1.05	1335 ± 11	35.89	3515 ± 30
2014-11-15	56976	1.65	1.09	1257 ± 13	35.34	3288 ± 33
2014-11-18	56979	1.69	1.14	1326 ± 11	34.65	3437 ± 28

Computed $Af\rho$ parameter in the RC filter of comet PanSTARRS (continued)						
2014-11-27	56988	1.79	1.34	1247 ± 26	33.00	3158 ± 65
2014-12-04	56995	1.87	1.52	1230 ± 15	31.74	3055 ± 37
2014-12-15	57006	2.00	1.83	1280 ± 18	29.40	3059 ± 42
2014-12-19	57010	2.05	1.94	1308 ± 8	28.43	3072 ± 19
2015-01-03	57025	2.23	2.38	1278 ± 19	24.39	2766 ± 40
2015-01-09	57031	2.30	2.55	1250 ± 20	22.66	2603 ± 41
2015-01-20	57042	2.42	2.85	1271 ± 12	19.44	2447 ± 23
2015-01-28	57050	2.52	3.06	1224 ± 12	17.11	2213 ± 22
2015-02-02	57055	2.58	3.18	1228 ± 23	15.68	2133 ± 41
2015-09-01	57266	4.83	3.90	1059 ± 53	5.14	1297 ± 65

Computed $Af\rho$ parameter in the BC filter of comet PanSTARRS						
Date	MJD	r_h	Δ	$Af\rho$	angle	corrected $Af\rho$)
2013-07-12	56485	5.24	4.73	2808 ± 125	10.17	4110 ± 182
2013-08-13	56517	4.92	4.87	2779 ± 132	11.85	4298 ± 205
2013-08-19	56523	4.87	4.89	2683 ± 162	11.90	4156 ± 251
2014-02-05	56693	3.09	3.19	2459 ± 136	17.93	4548 ± 252
2014-02-08	56696	3.06	3.11	2484 ± 124	18.34	4644 ± 231
2014-02-09	56697	3.05	3.08	2412 ± 97	18.47	4526 ± 183
2014-02-10	56698	3.03	3.05	2540 ± 70	18.60	4783 ± 132
2014-02-11	56699	3.02	3.03	2320 ± 66	18.73	4383 ± 125
2014-02-16	56704	2.97	2.89	2410 ± 118	19.32	4624 ± 227
2014-02-19	56707	2.93	2.81	2385 ± 92	19.63	4612 ± 179
2014-02-21	56709	2.91	2.76	2204 ± 91	19.83	4285 ± 177
2014-02-23	56711	2.89	2.70	2263 ± 68	20.01	4418 ± 132
2014-02-26	56714	2.85	2.62	2262 ± 74	20.25	4444 ± 146
2014-03-01	56717	2.82	2.54	2219 ± 80	20.46	4381 ± 159
2014-03-04	56720	2.78	2.46	2248 ± 72	20.62	4457 ± 143
2014-03-13	56729	2.68	2.23	2415 ± 54	20.90	4821 ± 108
2014-03-16	56732	2.65	2.16	2372 ± 76	20.92	4738 ± 152
2014-03-23	56739	2.56	1.99	2254 ± 69	20.85	4493 ± 137
2014-04-01	56748	2.46	1.80	2408 ± 83	20.69	4783 ± 165
2014-04-08	56755	2.38	1.68	2485 ± 112	20.79	4948 ± 223
2014-04-16	56763	2.28	1.57	2311 ± 202	21.56	4688 ± 410
2014-04-22	56769	2.21	1.52	2281 ± 126	22.80	4763 ± 263
2014-04-23	56770	2.20	1.51	2124 ± 115	23.06	4463 ± 242
2014-05-01	56778	2.11	1.48	2211 ± 140	25.66	4917 ± 311
2014-05-09	56786	2.01	1.48	1998 ± 136	28.71	4715 ± 322
2014-05-18	56795	1.91	1.52	1927 ± 103	31.85	4796 ± 257
2014-06-07	56815	1.66	1.73	1777 ± 66	34.74	4610 ± 171
2014-06-08	56816	1.65	1.74	1768 ± 71	34.71	4587 ± 183
2014-06-09	56817	1.64	1.76	1751 ± 67	34.65	4539 ± 175
2014-06-23	56831	1.49	1.92	1845 ± 72	32.02	4603 ± 180
2014-06-29	56837	1.42	1.98	2079 ± 110	29.89	5010 ± 266
2014-07-03	56841	1.38	2.01	2073 ± 104	28.14	4841 ± 242
2014-09-06	56906	1.07	1.82	1873 ± 117	27.62	4331 ± 270
2014-09-07	56907	1.07	1.80	1872 ± 99	28.58	4406 ± 233
2014-09-20	56920	1.13	1.56	1380 ± 54	39.55	3782 ± 149
2014-09-27	56927	1.17	1.42	1198 ± 32	43.91	3412 ± 92
2014-09-28	56928	1.18	1.40	1173 ± 29	44.42	3353 ± 84
2014-10-06	56936	1.24	1.25	1181 ± 22	47.32	3441 ± 63
2014-10-07	56937	1.25	1.23	1172 ± 36	47.52	3419 ± 104
2014-10-11	56941	1.29	1.15	1028 ± 24	47.93	3003 ± 70

Computed $Af\rho$ parameter in the BC filter of comet PanSTARRS (continued)						
2014-10-13	56943	1.30	1.12	1131 ± 39	47.90	3305 ± 115
2014-10-23	56953	1.40	0.99	889 ± 25	45.37	2559 ± 73
2014-10-27	56957	1.44	0.96	981 ± 28	43.48	2784 ± 79
2014-11-04	56965	1.53	0.96	1013 ± 37	39.37	2770 ± 102
2014-11-07	56968	1.56	0.98	883 ± 29	38.01	2382 ± 79
2014-11-09	56970	1.58	1.00	1013 ± 42	37.21	2710 ± 112
2014-11-10	56971	1.59	1.01	947 ± 21	36.85	2524 ± 55
2014-11-13	56974	1.63	1.05	1006 ± 35	35.89	2648 ± 92
2014-11-13	56974	1.63	1.05	1010 ± 28	35.89	2659 ± 74
2014-11-15	56976	1.65	1.09	850 ± 58	35.34	2224 ± 153
2014-11-18	56979	1.69	1.14	992 ± 17	34.65	2572 ± 45
2014-12-04	56995	1.87	1.52	984 ± 36	31.74	2444 ± 89
2014-12-06	56997	1.90	1.58	1017 ± 49	31.35	2512 ± 120
2014-12-08	56999	1.92	1.63	1003 ± 39	30.94	2459 ± 95
2014-12-15	57006	2.00	1.83	985 ± 22	29.40	2352 ± 54
2014-12-19	57010	2.05	1.94	960 ± 21	28.43	2253 ± 50
2015-01-03	57025	2.23	2.38	1021 ± 35	24.39	2210 ± 77
2015-01-09	57031	2.29	2.55	1045 ± 40	22.66	2175 ± 84
2015-01-20	57042	2.42	2.85	972 ± 32	19.44	1870 ± 61
2015-01-28	57050	2.52	3.06	952 ± 43	17.11	1722 ± 78
2015-02-02	57055	2.58	3.18	947 ± 80	15.68	1645 ± 139
2015-09-01	57266	4.83	3.90	792 ± 179	5.14	970 ± 219

Computed $Af\rho$ parameter in the GC filter of comet PanSTARRS						
Date	MJD	r_h	Δ	$Af\rho$	angle	corrected $Af\rho$)
2013-07-12	56485	5.24	4.73	2924 ± 52	10.17	4279 ± 76
2013-08-14	56518	4.92	4.87	2768 ± 54	11.87	4282 ± 83
2013-08-19	56523	4.87	4.89	2650 ± 99	11.90	4104 ± 153
2014-02-03	56691	3.11	3.24	2698 ± 50	17.65	4951 ± 91
2014-02-06	56694	3.08	3.16	2613 ± 105	18.07	4850 ± 194
2014-02-08	56696	3.06	3.11	2570 ± 74	18.34	4805 ± 138
2014-02-09	56697	3.05	3.08	2578 ± 49	18.47	4836 ± 91
2014-02-14	56702	2.99	2.95	2449 ± 48	19.09	4670 ± 91
2014-02-16	56704	2.97	2.89	2455 ± 97	19.32	4710 ± 185
2014-02-20	56708	2.92	2.78	2438 ± 41	19.73	4727 ± 80
2014-02-23	56711	2.89	2.70	2196 ± 52	20.01	4289 ± 102
2014-03-01	56717	2.82	2.54	2367 ± 33	20.46	4674 ± 66
2014-03-17	56733	2.63	2.13	2399 ± 45	20.91	4792 ± 89
2014-03-23	56739	2.56	2.00	2282 ± 47	20.85	4551 ± 95
2014-04-01	56748	2.46	1.81	2342 ± 43	20.69	4653 ± 85
2014-04-08	56755	2.38	1.68	2485 ± 52	20.79	4948 ± 103
2014-04-16	56763	2.28	1.57	2218 ± 61	21.56	4500 ± 125
2014-04-22	56769	2.21	1.52	2299 ± 72	22.80	4803 ± 151
2014-05-01	56778	2.11	1.48	2119 ± 69	25.66	4713 ± 154
2014-05-09	56786	2.01	1.48	1893 ± 67	28.71	4467 ± 159
2014-05-18	56795	1.91	1.52	1950 ± 61	31.85	4853 ± 152
2014-05-31	56808	1.75	1.64	1825 ± 51	34.52	4721 ± 131
2014-06-07	56815	1.66	1.73	1788 ± 41	34.74	4641 ± 105
2014-06-08	56816	1.65	1.74	1856 ± 41	34.71	4814 ± 105
2014-09-06	56906	1.07	1.82	1956 ± 59	27.62	4523 ± 137
2014-09-20	56920	1.13	1.56	1481 ± 37	39.55	4058 ± 101
2014-09-27	56927	1.17	1.42	1290 ± 21	43.91	3674 ± 61
2014-09-28	56928	1.18	1.40	1286 ± 22	44.42	3678 ± 62
2014-10-06	56936	1.24	1.25	1284 ± 18	47.32	3741 ± 52
2014-10-07	56937	1.25	1.23	1289 ± 26	47.52	3760 ± 75
2014-10-11	56941	1.28	1.15	1223 ± 21	47.93	3574 ± 62
2014-10-13	56943	1.30	1.12	1189 ± 28	47.90	3473 ± 82
2014-10-23	56953	1.40	0.99	1041 ± 14	45.37	2996 ± 39
2014-10-27	56957	1.44	0.96	1076 ± 26	43.48	3052 ± 74
2014-11-07	56968	1.56	0.98	1010 ± 21	38.01	2725 ± 56
2014-11-10	56971	1.59	1.01	1067 ± 17	36.85	2843 ± 45
2014-11-13	56974	1.63	1.05	1063 ± 14	35.89	2800 ± 36
2014-11-15	56976	1.65	1.09	1001 ± 21	35.34	2619 ± 55
2014-11-18	56979	1.69	1.14	1040 ± 24	34.65	2695 ± 61
2014-11-27	56988	1.79	1.34	1035 ± 17	33.00	2621 ± 44

Computed $Af\rho$ parameter in the GC filter of comet PanSTARRS (continued)						
2014-12-04	56995	1.87	1.52	1024 ± 22	31.74	2544 ± 55
2014-12-15	57006	2.00	1.83	1048 ± 20	29.40	2503 ± 47
2014-12-19	57010	2.05	1.94	1062 ± 13	28.43	2493 ± 30
2015-01-03	57025	2.23	2.38	1151 ± 37	24.39	2492 ± 81

C.2 $Af\rho$ of comet Lovejoy

Computed $Af\rho$ parameter in the R filter of comet Lovejoy						
Date	MJD	r_h	Δ	$Af\rho$	angle	corrected $Af\rho$)
2013-09-11	56546	1.92	1.83	168 ± 3	30.88	412 ± 8
2013-09-12	56547	1.91	1.81	179 ± 4	31.17	440 ± 11
2013-09-16	56551	1.85	1.71	178 ± 4	32.32	447 ± 9
2013-09-20	56555	1.80	1.62	161 ± 5	33.52	410 ± 12
2013-09-21	56556	1.79	1.59	190 ± 6	33.83	487 ± 16
2013-09-25	56560	1.73	1.50	229 ± 6	35.11	598 ± 17
2013-09-26	56561	1.72	1.47	231 ± 4	35.44	604 ± 10
2013-09-29	56564	1.68	1.40	227 ± 9	36.45	602 ± 23
2013-10-03	56568	1.63	1.30	278 ± 4	37.86	749 ± 12
2013-10-04	56569	1.61	1.27	276 ± 5	38.22	746 ± 13
2013-10-05	56570	1.60	1.25	277 ± 7	38.60	752 ± 20
2013-10-06	56571	1.58	1.23	282 ± 5	38.97	767 ± 13
2013-10-08	56573	1.56	1.18	273 ± 6	39.74	748 ± 17
2013-10-10	56575	1.53	1.13	339 ± 10	40.54	938 ± 29
2013-10-20	56585	1.40	0.89	452 ± 7	45.02	1298 ± 19
2013-10-21	56586	1.38	0.87	411 ± 9	45.53	1184 ± 26
2013-10-24	56589	1.34	0.80	515 ± 10	47.13	1499 ± 28
2013-10-24	56589	1.34	0.80	543 ± 8	47.13	1581 ± 23
2013-10-26	56591	1.32	0.76	573 ± 14	48.28	1678 ± 40
2013-11-02	56598	1.23	0.61	685 ± 10	53.03	2025 ± 28
2014-02-13	56701	1.26	1.56	1675 ± 30	39.38	4583 ± 81
2014-02-14	56702	1.27	1.56	1513 ± 28	39.24	4133 ± 76
2014-02-15	56703	1.28	1.56	1463 ± 27	39.11	3993 ± 73
2014-02-16	56704	1.29	1.57	1392 ± 30	38.99	3795 ± 81
2014-02-21	56709	1.36	1.58	1203 ± 23	38.42	3261 ± 62
2014-02-22	56710	1.37	1.58	1261 ± 16	38.31	3415 ± 43
2014-03-01	56717	1.47	1.59	1015 ± 10	37.59	2727 ± 28
2014-03-06	56722	1.53	1.59	917 ± 10	37.03	2449 ± 27
2014-03-13	56729	1.63	1.58	757 ± 9	36.10	1999 ± 24
2014-03-17	56733	1.68	1.57	700 ± 15	35.46	1832 ± 41
2014-03-18	56734	1.70	1.57	654 ± 12	35.29	1709 ± 31
2014-03-25	56741	1.79	1.55	575 ± 10	33.87	1473 ± 25
2014-03-26	56742	1.80	1.55	567 ± 23	33.63	1450 ± 58
2014-04-04	56751	1.92	1.52	442 ± 14	31.13	1087 ± 34
2014-04-10	56757	2.00	1.50	444 ± 9	29.04	1053 ± 21
2014-04-14	56761	2.06	1.49	394 ± 8	27.44	907 ± 19
2014-04-15	56762	2.07	1.48	408 ± 20	27.02	932 ± 46

Computed $Af\rho$ parameter in the R filter of comet Lovejoy (continued)						
2014-04-16	56763	2.08	1.48	374 ± 9	26.58	847 ± 20
2014-04-18	56765	2.11	1.48	355 ± 12	25.68	789 ± 27
2014-04-22	56769	2.16	1.47	352 ± 13	23.77	752 ± 29
2014-04-25	56772	2.20	1.47	393 ± 23	22.24	811 ± 48
2014-05-06	56783	2.34	1.47	237 ± 30	16.01	416 ± 52
2014-05-08	56785	2.37	1.48	318 ± 19	14.80	538 ± 33
2014-05-14	56791	2.44	1.50	287 ± 25	11.11	433 ± 38
2014-05-20	56797	2.52	1.54	249 ± 12	7.39	331 ± 16
2014-05-24	56801	2.57	1.57	359 ± 28	4.96	437 ± 34
2014-05-27	56804	2.61	1.60	377 ± 11	3.18	429 ± 12
2014-05-31	56808	2.66	1.64	429 ± 8	0.91	445 ± 8
2014-06-22	56830	2.93	1.99	243 ± 11	9.25	345 ± 16
2014-06-24	56832	2.95	2.03	279 ± 6	9.94	404 ± 9
2014-06-30	56838	3.02	2.15	241 ± 12	11.76	372 ± 19
2014-07-04	56842	3.07	2.23	199 ± 8	12.78	316 ± 13
2014-07-06	56844	3.10	2.30	195 ± 9	13.24	314 ± 15
2014-07-13	56851	3.18	2.45	191 ± 18	14.57	321 ± 30
2014-07-18	56856	3.23	2.57	170 ± 8	15.29	293 ± 14
2014-07-25	56863	3.32	2.75	138 ± 28	15.99	242 ± 48
2014-08-04	56873	3.43	3.00	96 ± 13	16.49	170 ± 22
2014-08-09	56878	3.50	3.16	122 ± 8	16.54	218 ± 15
2014-08-09	56878	3.50	3.16	145 ± 6	16.54	257 ± 11
2014-08-09	56878	3.50	3.16	133 ± 10	16.54	236 ± 18
2014-08-09	56878	3.50	3.16	125 ± 9	16.54	222 ± 17
2014-08-20	56889	3.61	3.43	111 ± 11	16.27	196 ± 19
2014-08-20	56889	3.61	3.43	114 ± 10	16.27	201 ± 17
2014-08-20	56889	3.61	3.43	111 ± 8	16.27	196 ± 14
2014-08-20	56889	3.61	3.43	120 ± 7	16.27	212 ± 13
2014-09-06	56906	3.80	3.88	65 ± 12	15.04	111 ± 20
2014-09-06	56906	3.80	3.88	79 ± 13	15.04	134 ± 22
2014-09-06	56906	3.80	3.88	60 ± 17	15.04	102 ± 30
2014-09-06	56906	3.80	3.88	64 ± 15	15.04	110 ± 25

Computed $Af\rho$ parameter in the RC filter of comet Lovejoy						
Date	MJD	r_h	Δ	$Af\rho$	angle	corrected $Af\rho$)
2013-09-12	56547	1.91	1.81	174 ± 4	31.17	428 ± 11
2013-09-21	56556	1.79	1.59	194 ± 7	33.83	496 ± 18
2013-09-29	56564	1.68	1.40	273 ± 6	36.45	724 ± 16
2013-10-06	56571	1.58	1.23	295 ± 8	38.97	803 ± 22
2013-10-21	56586	1.38	0.87	477 ± 8	45.53	1375 ± 23
2013-10-26	56591	1.32	0.76	561 ± 12	48.28	1642 ± 34
2013-11-02	56598	1.23	0.61	693 ± 8	53.03	2049 ± 23
2014-02-14	56702	1.27	1.56	1574 ± 28	39.24	4300 ± 76
2014-02-22	56710	1.37	1.58	1326 ± 17	38.31	3589 ± 45
2014-03-01	56717	1.47	1.59	1102 ± 14	37.59	2959 ± 36
2014-03-17	56733	1.68	1.57	783 ± 14	35.46	2050 ± 35
2014-03-18	56734	1.70	1.57	718 ± 14	35.29	1878 ± 37
2014-03-26	56742	1.80	1.55	601 ± 29	33.63	1536 ± 73
2014-04-04	56751	1.92	1.52	491 ± 11	31.13	1209 ± 27
2014-04-10	56757	2.00	1.50	459 ± 18	29.04	1090 ± 43
2014-04-15	56762	2.07	1.48	448 ± 20	27.02	1024 ± 46
2014-04-18	56765	2.11	1.48	404 ± 27	25.68	900 ± 60
2014-04-25	56772	2.20	1.47	411 ± 20	22.24	847 ± 42
2014-05-20	56797	2.52	1.54	283 ± 22	7.39	377 ± 30
2014-05-27	56804	2.61	1.60	446 ± 29	3.18	508 ± 32
2014-06-07	56815	2.74	1.74	422 ± 12	2.84	474 ± 14
2014-06-22	56830	2.93	1.99	212 ± 11	9.25	301 ± 15
2014-06-24	56832	2.95	2.03	125 ± 11	9.94	181 ± 15
2014-07-18	56856	3.23	2.57	198 ± 16	15.29	339 ± 28
2014-08-04	56873	3.43	3.00	93 ± 55	16.49	165 ± 98

Computed $Af\rho$ parameter in the BC filter of comet Lovejoy						
Date	MJD	r_h	Δ	$Af\rho$	angle	corrected $Af\rho$)
2013-09-16	56551	1.85	1.71	141 ± 7	32.32	354 ± 18
2013-09-21	56556	1.79	1.59	168 ± 10	33.83	432 ± 27
2013-09-25	56560	1.73	1.50	146 ± 12	35.11	381 ± 31
2013-09-29	56564	1.68	1.40	176 ± 9	36.45	466 ± 24
2013-10-03	56568	1.62	1.30	222 ± 10	37.86	597 ± 26
2013-10-05	56570	1.60	1.25	222 ± 6	38.60	604 ± 18
2013-10-08	56573	1.56	1.18	241 ± 9	39.74	661 ± 24
2013-10-10	56575	1.53	1.13	259 ± 9	40.54	715 ± 25
2013-10-20	56585	1.40	0.89	322 ± 11	45.02	924 ± 32
2013-10-24	56589	1.34	0.80	361 ± 15	47.13	1051 ± 45
2013-10-26	56591	1.32	0.75	461 ± 14	48.28	1348 ± 41
2014-02-13	56701	1.26	1.56	1473 ± 60	39.38	4031 ± 165
2014-02-15	56703	1.28	1.56	1255 ± 51	39.11	3424 ± 140
2014-02-21	56709	1.36	1.58	1018 ± 33	38.42	2758 ± 88
2014-02-22	56710	1.37	1.58	1045 ± 34	38.31	2828 ± 92
2014-02-28	56716	1.45	1.59	792 ± 22	37.69	2130 ± 58
2014-03-01	56717	1.47	1.59	864 ± 31	37.59	2321 ± 83
2014-03-06	56722	1.53	1.59	767 ± 18	37.03	2047 ± 47
2014-03-13	56729	1.63	1.58	651 ± 24	36.10	1718 ± 64
2014-03-17	56733	1.68	1.57	563 ± 49	35.46	1476 ± 128
2014-03-18	56734	1.70	1.57	606 ± 21	35.29	1584 ± 56
2014-03-25	56741	1.79	1.55	481 ± 18	33.87	1233 ± 46
2014-03-26	56742	1.80	1.55	484 ± 18	33.63	1237 ± 46
2014-04-04	56751	1.92	1.52	279 ± 16	31.13	687 ± 38
2014-04-10	56757	2.00	1.50	367 ± 15	29.04	872 ± 35
2014-04-14	56761	2.06	1.49	358 ± 21	27.44	825 ± 48
2014-04-18	56765	2.11	1.48	318 ± 23	25.68	708 ± 50
2014-04-22	56769	2.16	1.47	305 ± 18	23.77	651 ± 38
2014-04-25	56772	2.20	1.47	316 ± 13	22.24	651 ± 27
2014-05-08	56785	2.37	1.48	358 ± 24	14.80	607 ± 41
2014-05-14	56791	2.44	1.50	283 ± 47	11.11	427 ± 71
2014-05-20	56797	2.52	1.54	252 ± 17	7.39	335 ± 23
2014-05-24	56801	2.57	1.57	328 ± 33	4.96	399 ± 40
2014-05-27	56804	2.61	1.60	326 ± 32	3.18	370 ± 36
2014-05-31	56808	2.66	1.64	395 ± 12	0.91	410 ± 12
2014-06-07	56815	2.74	1.73	338 ± 19	2.84	379 ± 22
2014-06-22	56830	2.93	1.99	226 ± 26	9.25	321 ± 37
2014-06-24	56832	2.95	2.03	198 ± 18	9.94	287 ± 25
2014-06-30	56838	3.02	2.15	189 ± 23	11.76	291 ± 36
2014-07-04	56842	3.07	2.23	176 ± 20	12.78	280 ± 32

Computed $Af\rho$ parameter in the BC filter of comet Lovejoy (continued)						
2014-07-07	56845	3.10	2.30	150 ± 31	13.45	244 ± 51
2014-07-18	56856	3.23	2.57	100 ± 23	15.29	172 ± 40
2014-08-04	56873	3.43	3.00	50 ± 57	16.49	89 ± 101

Computed $Af\rho$ parameter in the GC filter of comet Lovejoy						
Date	MJD	r_h	Δ	$Af\rho$	angle	corrected $Af\rho$)
2013-09-12	56547	1.91	1.81	139 ± 6	31.17	342 ± 15
2013-09-29	56564	1.68	1.40	196 ± 7	36.45	520 ± 19
2013-10-05	56570	1.60	1.25	240 ± 6	38.60	651 ± 16
2013-10-21	56586	1.38	0.87	382 ± 12	45.53	1101 ± 36
2013-10-26	56591	1.32	0.76	463 ± 14	48.28	1355 ± 40
2013-11-02	56598	1.23	0.61	498 ± 9	53.03	1472 ± 26
2014-02-14	56702	1.27	1.56	1331 ± 34	39.24	3637 ± 93
2014-02-22	56710	1.37	1.58	1089 ± 19	38.31	2947 ± 53
2014-03-01	56717	1.47	1.59	898 ± 14	37.59	2412 ± 39
2014-03-17	56733	1.68	1.57	624 ± 16	35.46	1635 ± 42
2014-03-18	56734	1.70	1.57	577 ± 16	35.29	1507 ± 42
2014-03-26	56742	1.80	1.55	513 ± 10	33.63	1310 ± 26
2014-04-04	56751	1.92	1.52	353 ± 9	31.13	869 ± 22
2014-04-10	56757	2.00	1.50	375 ± 11	29.04	890 ± 26
2014-04-15	56762	2.07	1.48	359 ± 16	27.02	821 ± 38
2014-04-18	56765	2.11	1.48	378 ± 15	25.68	841 ± 33
2014-04-25	56772	2.20	1.47	299 ± 13	22.24	617 ± 26
2014-05-20	56797	2.52	1.54	252 ± 22	7.39	335 ± 29
2014-05-27	56804	2.61	1.60	434 ± 15	3.18	494 ± 17
2014-05-31	56808	2.66	1.64	410 ± 11	0.91	425 ± 11
2014-06-07	56815	2.74	1.74	362 ± 12	2.84	406 ± 14
2014-07-04	56842	3.07	2.23	180 ± 30	12.78	286 ± 48
2014-08-04	56873	3.43	3.00	117 ± 61	16.49	208 ± 109

Appendix D

Dust-to-gas ratios

This section contains the logarithmic dust-to-gas abundance ratios. The $Af\rho$ parameter is in cm and measured in the R and RC filters, and is compared to the gas productions of CN and H_2O, in molecules per second. The ratios of $Af\rho$ (R) values and CN production rates, $Af\rho$ (RC) values and CN production rates, $Af\rho$ (R) values and H_2O production rates and $Af\rho$ (RC) values and H_2O production rates are each presented in individual tables, for each comet.
MJD represents the date of the observation night in Modified Julian Days, while r_h represents the heliocentric distance and is expressed in AU.

D.1 Dust-to-gas ratio of comet PanSTARRS

Ratios of $Af\rho$ (R) values and CN production rates of comet PanSTARRS			
Date	MJD	r_h	$\log(Af\rho(R)/Q(CN))$
2014-02-03	56691	3.113	-21.93 ± 0.06
2014-02-06	56694	3.079	-21.86 ± 0.05
2014-02-09	56697	3.045	-21.87 ± 0.05
2014-02-11	56699	3.023	-21.87 ± 0.04
2014-02-14	56702	2.989	-21.85 ± 0.05
2014-02-17	56705	2.955	-22.01 ± 0.04
2014-02-19	56707	2.932	-21.92 ± 0.04
2014-02-26	56714	2.852	-21.99 ± 0.03
2014-03-04	56720	2.784	-22.04 ± 0.03
2014-03-13	56729	2.680	-22.04 ± 0.03
2014-03-23	56739	2.563	-22.09 ± 0.03
2014-04-01	56748	2.458	-22.14 ± 0.04
2014-04-08	56755	2.376	-22.17 ± 0.04
2014-04-16	56763	2.283	-22.14 ± 0.06
2014-04-23	56770	2.201	-22.14 ± 0.05

Ratios of $Af\rho$ (R) values and CN production rates of comet PanSTARRS (continued)			
2014-05-01	56778	2.107	-22.19 ± 0.05
2014-05-09	56786	2.013	-22.19 ± 0.05
2014-05-18	56795	1.907	-22.16 ± 0.04
2014-05-20	56797	1.884	-22.23 ± 0.04
2014-05-30	56807	1.756	-22.25 ± 0.03
2014-06-07	56815	1.664	-22.27 ± 0.03
2014-06-08	56816	1.653	-22.22 ± 0.03
2014-06-09	56817	1.641	-22.21 ± 0.03
2014-06-23	56831	1.486	-22.24 ± 0.03
2014-06-29	56837	1.423	-22.32 ± 0.03
2014-07-03	56841	1.382	-22.33 ± 0.03
2014-09-06	56906	1.067	-22.39 ± 0.03
2014-09-07	56907	1.070	-22.30 ± 0.04
2014-09-20	56920	1.126	-22.28 ± 0.02
2014-09-27	56927	1.171	-22.31 ± 0.02
2014-09-28	56928	1.179	-22.35 ± 0.02
2014-10-06	56936	1.242	-22.33 ± 0.01
2014-10-07	56937	1.250	-22.37 ± 0.02
2014-10-11	56941	1.286	-22.24 ± 0.01
2014-10-13	56943	1.303	-22.31 ± 0.02
2014-10-13	56943	1.303	-22.31 ± 0.02
2014-10-13	56943	1.303	-22.31 ± 0.02
2014-10-13	56943	1.303	-22.33 ± 0.02
2014-10-13	56943	1.304	-22.31 ± 0.02
2014-10-13	56943	1.304	-22.30 ± 0.01
2014-10-13	56943	1.304	-22.30 ± 0.01
2014-10-13	56943	1.304	-22.29 ± 0.01
2014-10-13	56943	1.304	-22.28 ± 0.01
2014-11-04	56965	1.530	-22.21 ± 0.01
2014-11-06	56967	1.551	-22.26 ± 0.01
2014-11-07	56968	1.561	-22.22 ± 0.02
2014-11-09	56970	1.585	-22.27 ± 0.02
2014-11-10	56971	1.594	-22.27 ± 0.02
2014-11-13	56974	1.629	-22.22 ± 0.02
2014-11-13	56974	1.630	-22.25 ± 0.02
2014-11-18	56979	1.686	-22.27 ± 0.01
2014-11-27	56988	1.789	-22.26 ± 0.02
2014-12-04	56995	1.871	-22.19 ± 0.02
2014-12-06	56997	1.895	-22.14 ± 0.03
2014-12-08	56999	1.918	-22.22 ± 0.02
2014-12-15	57006	2.000	-22.23 ± 0.02
2014-12-19	57010	2.047	-22.13 ± 0.01

Ratios of $Af\rho$ (R) values and CN production rates of comet PanSTARRS (continued)			
2015-01-03	57025	2.224	-22.11 ± 0.03
2015-01-09	57031	2.295	-22.07 ± 0.03
2015-01-20	57042	2.424	-22.03 ± 0.03

Ratios of $Af\rho$ (RC) values and CN production rates of comet PanSTARRS			
Date	MJD	r_h	$\log(Af\rho(RC)/Q(CN))$
2014-02-06	56694	3.079	-21.85 ± 0.05
2014-02-09	56697	3.045	-21.82 ± 0.05
2014-03-23	56739	2.563	-22.07 ± 0.03
2014-04-01	56748	2.458	-22.12 ± 0.04
2014-04-08	56755	2.376	-22.14 ± 0.04
2014-04-16	56763	2.283	-22.13 ± 0.06
2014-04-23	56770	2.201	-22.11 ± 0.04
2014-05-01	56778	2.107	-22.23 ± 0.05
2014-05-09	56786	2.013	-22.24 ± 0.05
2014-05-18	56795	1.907	-22.13 ± 0.04
2014-06-07	56815	1.664	-22.25 ± 0.03
2014-06-08	56816	1.653	-22.20 ± 0.03
2014-06-09	56817	1.641	-22.18 ± 0.03
2014-06-23	56831	1.486	-22.23 ± 0.03
2014-09-06	56906	1.067	-22.40 ± 0.03
2014-09-20	56920	1.126	-22.29 ± 0.02
2014-09-27	56927	1.171	-22.31 ± 0.02
2014-09-28	56928	1.179	-22.35 ± 0.01
2014-10-06	56936	1.242	-22.32 ± 0.01
2014-10-07	56937	1.250	-22.37 ± 0.02
2014-10-11	56941	1.286	-22.23 ± 0.01
2014-10-13	56943	1.303	-22.30 ± 0.02
2014-10-13	56943	1.303	-22.30 ± 0.02
2014-10-13	56943	1.303	-22.30 ± 0.02
2014-10-13	56943	1.303	-22.32 ± 0.02
2014-10-13	56943	1.304	-22.30 ± 0.02
2014-10-13	56943	1.304	-22.29 ± 0.01
2014-10-13	56943	1.304	-22.29 ± 0.01
2014-10-13	56943	1.304	-22.28 ± 0.01
2014-10-13	56943	1.304	-22.27 ± 0.01
2014-10-23	56953	1.402	-22.28 ± 0.01
2014-10-27	56957	1.443	-22.31 ± 0.01
2014-11-06	56967	1.551	-22.24 ± 0.01
2014-11-07	56968	1.561	-22.20 ± 0.02
2014-11-09	56970	1.585	-22.26 ± 0.02
2014-11-10	56971	1.594	-22.19 ± 0.02
2014-11-13	56974	1.629	-22.21 ± 0.02
2014-11-13	56974	1.630	-22.22 ± 0.02
2014-11-18	56979	1.686	-22.23 ± 0.01
2014-11-27	56988	1.789	-22.23 ± 0.02

Ratios of $Af\rho$ (RC) values and CN production rates of comet PanSTARRS (continued)			
2014-12-04	56995	1.871	-22.17 ± 0.02
2014-12-15	57006	2.000	-22.17 ± 0.02
2014-12-19	57010	2.047	-22.09 ± 0.01
2015-01-03	57025	2.224	-22.08 ± 0.03
2015-01-09	57031	2.295	-22.05 ± 0.03
2015-01-20	57042	2.424	-22.02 ± 0.03
2015-01-28	57050	2.518	-21.86 ± 0.05
2015-02-02	57055	2.576	-21.85 ± 0.08

Ratios of $Af\rho$ (R) values and H_2O production rates of comet PanSTARRS			
Date	MJD	r_h	$\log(Af\rho(R)/Q(H_2O))$
2014-03-23	56739	2.563	-24.67 ± 0.14
2014-06-29	56837	1.423	-25.14 ± 0.14
2014-09-06	56906	1.067	-24.91 ± 0.15
2014-09-07	56907	1.070	-24.73 ± 0.14
2014-09-20	56920	1.126	-24.81 ± 0.09
2014-09-27	56927	1.171	-24.89 ± 0.06
2014-09-28	56928	1.179	-24.94 ± 0.06
2014-10-06	56936	1.242	-25.05 ± 0.04
2014-10-07	56937	1.250	-25.02 ± 0.06
2014-10-11	56941	1.286	-25.16 ± 0.04
2014-10-13	56943	1.304	-25.11 ± 0.05
2014-11-09	56970	1.585	-25.05 ± 0.05
2014-11-13	56974	1.629	-24.97 ± 0.05
2014-11-13	56974	1.630	-24.96 ± 0.06
2014-11-18	56979	1.686	-24.97 ± 0.05
2014-11-27	56988	1.789	-24.94 ± 0.05
2014-12-04	56995	1.871	-24.88 ± 0.05
2014-12-06	56997	1.895	-24.86 ± 0.07
2014-12-08	56999	1.917	-24.84 ± 0.05
2014-12-15	57006	2.000	-24.80 ± 0.05
2014-12-19	57010	2.046	-24.73 ± 0.05
2015-01-03	57025	2.224	-24.53 ± 0.08
2015-01-09	57031	2.295	-24.47 ± 0.09

Ratios of $Af\rho$ (RC) values and H_2O production rates of comet PanSTARRS			
Date	MJD	r_h	$\log(Af\rho(RC)/Q(H_2O))$
2014-03-23	56739	2.563	-24.65 ± 0.14
2014-09-06	56906	1.067	-24.93 ± 0.15
2014-09-20	56920	1.126	-24.81 ± 0.09
2014-09-27	56927	1.171	-24.89 ± 0.06
2014-09-28	56928	1.179	-24.94 ± 0.06
2014-10-06	56936	1.242	-25.04 ± 0.04
2014-10-07	56937	1.250	-25.02 ± 0.06
2014-10-11	56941	1.286	-25.15 ± 0.04
2014-10-13	56943	1.304	-25.10 ± 0.05
2014-10-23	56953	1.402	-25.05 ± 0.04
2014-10-27	56957	1.443	-25.08 ± 0.04
2014-11-09	56970	1.585	-25.05 ± 0.05
2014-11-13	56974	1.629	-24.94 ± 0.05
2014-11-13	56974	1.630	-24.93 ± 0.06
2014-11-18	56979	1.686	-24.93 ± 0.05
2014-11-27	56988	1.789	-24.91 ± 0.05
2014-12-04	56995	1.871	-24.86 ± 0.05
2014-12-15	57006	2.000	-24.75 ± 0.05
2014-12-19	57010	2.046	-24.68 ± 0.05
2015-01-03	57025	2.224	-24.49 ± 0.08
2015-01-09	57031	2.295	-24.46 ± 0.09

D.2 Dust-to-gas ratio of comet Lovejoy

Ratios of $Af\rho$ (R) values and CN production rates of comet Lovejoy			
Date	MJD	r_h	$\log(Af\rho(R)/Q(CN))$
2013-09-11	56546	1.920	-22.80 ± 0.02
2013-09-16	56551	1.854	-22.82 ± 0.02
2013-09-21	56556	1.787	-22.79 ± 0.02
2013-09-24	56559	1.746	-22.73 ± 0.02
2013-09-25	56560	1.733	-22.75 ± 0.02
2013-09-29	56564	1.680	-22.78 ± 0.03
2013-10-03	56568	1.626	-22.70 ± 0.02
2013-10-04	56569	1.612	-22.72 ± 0.01
2013-10-05	56570	1.599	-22.73 ± 0.02
2013-10-06	56571	1.585	-22.68 ± 0.02
2013-10-08	56573	1.558	-22.67 ± 0.02
2013-10-10	56575	1.532	-22.69 ± 0.02
2013-10-20	56585	1.398	-22.60 ± 0.02
2013-10-21	56586	1.384	-22.69 ± 0.02
2013-10-24	56589	1.344	-22.61 ± 0.01
2013-10-26	56591	1.318	-22.59 ± 0.02
2013-11-02	56598	1.227	-22.60 ± 0.02
2014-02-13	56701	1.256	-22.23 ± 0.02
2014-02-14	56702	1.269	-22.19 ± 0.02
2014-02-16	56704	1.295	-22.16 ± 0.03
2014-02-21	56709	1.361	-22.21 ± 0.02
2014-03-06	56722	1.535	-22.28 ± 0.02
2014-03-13	56729	1.629	-22.30 ± 0.02
2014-03-18	56734	1.696	-22.30 ± 0.02
2014-03-25	56741	1.791	-22.37 ± 0.02
2014-03-26	56742	1.804	-22.39 ± 0.02
2014-04-04	56751	1.924	-22.40 ± 0.02
2014-04-10	56757	2.004	-22.45 ± 0.02
2014-04-14	56761	2.057	-22.41 ± 0.04
2014-04-18	56765	2.109	-22.48 ± 0.03
2014-04-22	56769	2.161	-22.54 ± 0.03
2014-04-25	56772	2.201	-22.45 ± 0.03
2014-05-08	56785	2.369	-22.51 ± 0.05
2014-05-14	56791	2.442	-22.62 ± 0.07
2014-05-20	56797	2.520	-22.35 ± 0.10
2014-05-24	56801	2.571	-22.49 ± 0.07
2014-05-27	56804	2.608	-22.53 ± 0.06

Ratios of $Af\rho$ (R) values and CN production rates of comet Lovejoy (continued)			
2014-05-31	56808	2.656	-22.53 ± 0.04
2014-06-22	56830	2.926	-22.28 ± 0.09
2014-06-24	56832	2.950	-22.25 ± 0.08
2014-06-30	56838	3.022	-22.38 ± 0.11
2014-07-04	56842	3.067	-22.46 ± 0.11
2014-07-06	56844	3.102	-22.38 ± 0.11
2014-07-18	56856	3.234	-22.21 ± 0.13
2014-08-04	56873	3.430	-21.98 ± 0.68

Ratios of $Af\rho$ (RC) values and CN production rates of comet Lovejoy			
Date	MJD	r_h	$\log(Af\rho(RC)/Q(CN))$
2013-09-11	56546	1.920	-22.79 ± 0.02
2013-09-21	56556	1.787	-22.78 ± 0.03
2013-09-29	56564	1.680	-22.70 ± 0.02
2013-10-06	56571	1.585	-22.66 ± 0.02
2013-10-21	56586	1.384	-22.63 ± 0.02
2013-10-26	56591	1.318	-22.60 ± 0.02
2013-11-02	56598	1.227	-22.59 ± 0.01
2014-02-13	56701	1.256	-22.26 ± 0.02
2014-02-14	56702	1.269	-22.18 ± 0.02
2014-03-18	56734	1.696	-22.26 ± 0.02
2014-03-25	56741	1.791	-22.35 ± 0.03
2014-03-26	56742	1.804	-22.37 ± 0.02
2014-04-04	56751	1.924	-22.36 ± 0.02
2014-04-10	56757	2.004	-22.44 ± 0.02
2014-04-14	56761	2.057	-22.36 ± 0.04
2014-04-18	56765	2.109	-22.43 ± 0.04
2014-04-25	56772	2.201	-22.43 ± 0.03
2014-05-20	56797	2.520	-22.30 ± 0.10
2014-05-27	56804	2.608	-22.45 ± 0.06
2014-06-07	56815	2.743	-22.43 ± 0.06
2014-06-22	56830	2.926	-22.34 ± 0.09
2014-06-24	56832	2.950	-22.60 ± 0.09
2014-07-18	56856	3.234	-22.14 ± 0.13
2014-08-04	56873	3.430	-21.99 ± 0.72

Ratios of $Af\rho$ (R) values and H_2O production rates of comet Lovejoy			
Date	MJD	r_h	$\log(Af\rho(R)/Q(H_2O))$
2013-09-12	56547	1.907	-25.20 ± 0.08
2013-09-20	56555	1.800	-25.15 ± 0.06
2013-09-21	56556	1.787	-25.25 ± 0.05
2013-09-26	56561	1.720	-25.29 ± 0.05
2013-10-03	56568	1.626	-25.20 ± 0.06
2013-10-05	56570	1.599	-25.20 ± 0.06
2013-10-08	56573	1.558	-25.27 ± 0.06
2013-10-10	56575	1.532	-25.18 ± 0.07
2013-10-20	56585	1.398	-25.28 ± 0.07
2013-10-21	56586	1.384	-25.35 ± 0.05
2013-10-24	56589	1.344	-25.28 ± 0.05
2013-10-26	56591	1.318	-25.26 ± 0.05
2014-02-13	56701	1.256	-24.69 ± 0.10
2014-02-15	56703	1.282	-24.65 ± 0.09
2014-02-21	56709	1.361	-24.65 ± 0.08
2014-03-06	56722	1.535	-24.72 ± 0.06
2014-03-13	56729	1.629	-24.75 ± 0.05
2014-03-18	56734	1.696	-24.71 ± 0.06
2014-03-26	56742	1.804	-24.75 ± 0.05
2014-04-10	56757	2.004	-24.74 ± 0.05
2014-04-15	56762	2.069	-24.70 ± 0.06
2014-04-18	56765	2.110	-24.75 ± 0.05
2014-04-22	56769	2.160	-24.76 ± 0.05
2014-04-25	56772	2.201	-24.57 ± 0.07
2014-05-14	56791	2.442	-24.01 ± 0.95
2014-05-20	56797	2.520	-24.22 ± 0.33
2014-05-27	56804	2.608	-24.84 ± 0.09

Ratios of $Af\rho$ (RC) values and H_2O production rates of comet Lovejoy			
Date	MJD	r_h	$\log(Af\rho(RC)/Q(H_2O))$
2013-09-12	56547	1.907	-25.21 ± 0.08
2013-09-20	56555	1.800	-25.07 ± 0.06
2013-09-21	56556	1.787	-25.24 ± 0.05
2013-10-21	56586	1.384	-25.28 ± 0.05
2013-10-26	56591	1.318	-25.27 ± 0.05
2014-02-13	56701	1.256	-24.72 ± 0.10
2014-02-21	56709	1.361	-24.61 ± 0.07
2014-03-18	56734	1.696	-24.67 ± 0.06
2014-03-26	56742	1.804	-24.72 ± 0.05
2014-04-10	56757	2.004	-24.72 ± 0.05
2014-04-15	56762	2.069	-24.66 ± 0.06
2014-04-18	56765	2.110	-24.69 ± 0.06
2014-04-25	56772	2.201	-24.55 ± 0.07
2014-05-20	56797	2.520	-24.16 ± 0.33
2014-05-27	56804	2.608	-24.77 ± 0.10

Bibliography

[1] Hans Kerp. "Book Review: The biology and evolution of fossil plants. by T.N. Taylor and E.L. Taylor. Prentice Hall, Englewood Cliffs, NJ. 982 pp. ISBN 0-13-651589-4. US 95.00". In: *Review of Palaeobotany and Palynology* 79.3 (Jan. 1993), pp. 369–370. DOI: 10.1016/0034-6667(93)90030-X.

[2] European Space Agency. *Rosetta's comet contains ingredients for life*. URL: https://www.esa.int/Science_Exploration/Space_Science/Rosetta/Rosetta_s_comet_contains_ingredients_for_life. (accessed: 17.08.2025).

[3] Maria Teresa Capria et al. "Surface characteristics and activity of a dynamically new comet". In: *EPSC-DPS Joint Meeting 2019*. Vol. 2019. Sept. 2019, EPSC-DPS2019-1559, EPSC-DPS2019–1559.

[4] Licandro, J. et al. "The nature of comet-asteroid transition object (3200) Phaethon". In: *AA* 461.2 (2007), pp. 751–757. DOI: 10.1051/0004-6361:20065833. URL: https://doi.org/10.1051/0004-6361:20065833.

[5] J. R. Christianson and Tycho Brahe. "Tycho Brahe's German Treatise on the Comet of 1577: A Study in Science and Politics". In: *Isis* 70.1 (1979), pp. 110–140. ISSN: 00211753, 15456994. URL: http://www.jstor.org/stable/230882 (visited on 08/17/2025).

[6] Edmundo Halleio. "Astronomiae Cometicae Synopsis, Autore Edmundo Halleio apud Oxonienses. Geometriae Professore Saviliano, & Reg. Soc. S." In: *Philosophical Transactions of the Royal Society of London Series I* 24 (Jan. 1704), pp. 1882–1899.

[7] Kathy A. Miles and Charles F. Peters II. *Dirty Snowballs in Space*. URL: https://web.archive.org/web/20130129035627/http://starryskies.com/solar_system/Comet/dirty_snowballs.html. (accessed: 01.09.2016).

[8] Nathan X. Roth et al. "The Composition of Comet C/2012 K1 (PanSTARRS) and the Distribution of Primary Volatile Abundances Among Comets". In: *The Astronomical Journal* 153.4 (Mar. 2017), p. 168. DOI: 10.3847/1538-3881/aa5d18. URL: https://dx.doi.org/10.3847/1538-3881/aa5d18.

[9] Futura Sciences. *Hubble a déterminé la taille du noyau de la plus grosse comète jamais observée*. URL: https://www.futura-sciences.com/sciences/actualites/comete-hubble-determine-taille-noyau-plus-grosse-comete-jamais-observee-88192/. (accessed: 13.08.2025).

[10] Dale P. Cruikshank, W. K. Hartmann, and David J. Tholen. "Colour, albedo and nucleus size of Halley's comet". In: *Nature* 315.6015 (May 1, 1985), pp. 122–124. ISSN: 1476-4687. DOI: 10.1038/315122a0. URL: https://doi.org/10.1038/315122a0.

[11] *astro today, section 14.2: comets*. URL: http://lifeng.lamost.org/courses/astrotoday/CHAISSON/AT314/HTML/AT31402.HTM. (accessed: 04.05.2025).

[12] David Jewitt. *The Splintering of Comet 17P/Holmes During a Mega-Outburst*. URL: http://www2.ess.ucla.edu/~jewitt/holmes.html. (accessed: 04.05.2025).

[13] Maria Womack, Gal Sarid, and Kacper Wierzchos. "CO and Other Volatiles in Distantly Active Comets". In: *Publications of the Astronomical Society of the Pacific* 129 (Mar. 2017), p. 031001. DOI: 10.1088/1538-3873/129/973/031001.

[14] Michael F. A'Hearn et al. "The Ensemble Properties of Comets: Results from Narrowband Photometry of 85 Comets, 1976-1992". In: *Icarus* 118.2 (1995), pp. 223–270. ISSN: 0019-1035. DOI: https://doi.org/10.1006/icar.1995.1190. URL: https://www.sciencedirect.com/science/article/pii/S0019103585711906.

[15] H. Raab E. Kolmhofer. *Space Walk | What are comets*. Apr. 1997. URL: https://commons.wikimedia.org/w/index.php?curid=6756556. (accessed: 05.05.2025).

[16] *Space Walk | What are comets*. URL: https://starwalk.space/en/news/what-are-comets. (accessed: 05.05.2025).

[17] Robert Nemiroff and Jerry Bonnell. *NASA | Astronomy Picture of the Day*. URL: https://apod.nasa.gov/apod/ap050522.html. (accessed: 05.05.2025).

[18] K. Birkle et al. "Dust Tail Striae in Comet Hale-Bopp". In: *Astronomische Gesellschaft Abstract Series*. Vol. 14. Astronomische Gesellschaft Abstract Series. Jan. 1998, p. 100.

[19] Alessandro Morbidelli. *Origin and Dynamical Evolution of Comets and their Reservoirs*. 2005. arXiv: astro-ph/0512256 [astro-ph]. URL: https://arxiv.org/abs/astro-ph/0512256.

[20] H. F. Levison. "Comet Taxonomy". In: *Completing the Inventory of the Solar System*. Ed. by Terrence Rettig and Joseph M. Hahn. Vol. 107. Astronomical Society of the Pacific Conference Series. Jan. 1996, pp. 173–191.

[21] M. Duncan, H. Levison, and L. Dones. "Dynamical evolution of ecliptic comets". In: *Comets II*. Ed. by Michel C. Festou, H. Uwe Keller, and Harold A. Weaver. 2004, p. 193.

[22] ESA. *The Kuiper Belt and the Oort Cloud in context*. URL: https://www.esa.int/ESA_Multimedia/Images/2014/12/Kuiper_Belt_and_Oort_Cloud_in_context. (accessed: 24.03.2025).

[23] E. Jehin et al. "TRAPPIST: TRAnsiting Planets and PlanetesImals Small Telescope". In: *The Messenger* 145 (Sept. 2011), pp. 2–6.

[24] Tony L. Farnham, David G. Schleicher, and Michael F. A'Hearn. "The HB Narrowband Comet Filters: Standard Stars and Calibrations". In: *Icarus* 147.1 (2000), pp. 180–204. ISSN: 0019-1035. DOI: https://doi.org/10.1006/icar.2000.6420. URL: https://www.sciencedirect.com/science/article/pii/S0019103500964200.

[25] Opitom, C. et al. "TRAPPIST monitoring of comet C/2012 F6 (Lemmon)". In: *AA* 574 (2015), A38. DOI: 10.1051/0004-6361/201424582. URL: https://doi.org/10.1051/0004-6361/201424582.

[26] Minor Planet Center. *MPEC 2012-K36*. URL: http://www.minorplanetcenter.net/mpec/. (accessed: 03.03.2025).

[27] Kathy A. Miles and Charles F. Peters II. *Nasa Orbit Viewer*. URL: https://ssd.jpl.nasa.gov/tools/orbit_viewer.html. (accessed: 04.03.2025).

[28] Jet Production Laboratory. *JPL Horizons System*. URL: https://ssd.jpl.nasa.gov/horizons/app.html#/. (accessed: 22.03.2025).

[29] NASA. *Comet Lovejoy near Big Dipper*. URL: https://www.nasa.gov/image-article/comet-lovejoy-near-big-dipper. (accessed: 29.04.2025).

[30] Brian Warner. *A Practical Guide to Lightcurve Photometry and Analysis*. In collab. with Alan W. Harris. New York, NY: Springer New York, 2006. 1 p. ISBN: 978-0-387-29365-3 978-0-387-33391-5.

[31] S. Hmiddouch et al. *Variations in Volatile-Driven Activity of Comet C/2017 K2 (PanSTARRS) Revealed by Long-Term Multi-Wavelength Observations*. 2025. arXiv: 2507.13451 [astro-ph.EP]. URL: https://arxiv.org/abs/2507.13451.

[32] T. M. Bettio, A. S. Betzler, and O. F. de Sousa. "Nuclear parameters of comets 63P/Wild 1 and C/2012 K1 (PANSTARRS)". In: *Bulletin of the Astronomical Society of Brazil* 32 (Apr. 2020), pp. 176–177.

[33] D. Schleicher. *Composite Dust Phase Function for Comets*. URL: https://asteroid.lowell.edu/comet/dustphase/. (accessed: 21.03.2025).

[34] M. C. De Sanctis, J. Lasue, and M. T. Capria. "SEASONAL EFFECTS ON COMET NUCLEI EVOLUTION: ACTIVITY, INTERNAL STRUCTURE, AND DUST MANTLE FORMATION". In: *The Astronomical Journal* 140.1 (May 2010), p. 1. DOI: 10.1088/0004-6256/140/1/1. URL: https://dx.doi.org/10.1088/0004-6256/140/1/1.

[35] David Jewitt. "COLOR SYSTEMATICS OF COMETS AND RELATED BODIES". In: *The Astronomical Journal* (2015). DOI: http://dx.doi.org/10.1088/0004-6256/150/6/201.

[36] J. Holmberg, C. Flynn, and L. Portinari. "The colours of the Sun". In: *Monthly Notices of the Royal Astronomical Society* 367.2 (Apr. 1, 2006), pp. 449–453. ISSN: 0035-8711, 1365-2966. DOI: 10.1111/j.1365-2966.2005.09832.x. URL: https://academic.oup.com/mnras/article-lookup/doi/10.1111/j.1365-2966.2005.09832.x (visited on 03/23/2025).

[37] Leo Haser. "Distribution d'intensité dans la tête d'une comète". In: *Bulletin de la Classe des sciences* 43.1 (1957), pp. 740–750. ISSN: 0001-4141. DOI: 10.3406/barb.1957.68714. URL: https://www.persee.fr/doc/barb_0001-4141_1957_num_43_1_68714 (visited on 02/17/2025).

[38] Youssef Moulane. "Monitoring the activity and composition of comets with TRAPPIST telescopes". English. PhD thesis. ULiège - Université de Liège, 22 March 2021, p. 45. HDL: https://orbi.uliege.be/2268/258533.

[39] K. S. K. Swamy. "Physics of comets". In: *Singapore : World Scientific Publication* (1986).

[40] David G. Schleicher and Michael F. A'Hearn. "The Fluorescence of Cometary OH". In: 331 (Aug. 1988), p. 1058. DOI: 10.1086/166622.

[41] M. F. A'Hearn et al. "Comet Bowell 1980b". In: 89 (Apr. 1984), pp. 579–591. DOI: 10.1086/113552. URL: https://ui.adsabs.harvard.edu/abs/1984AJ.....89..579A. Provided by the SAO/NASA Astrophysics Data System.

[42] Michael F. A'Hearn et al. "The ensemble properties of comets: Results from narrowband photometry of 85 comets, 1976-1992." In: 118.2 (Dec. 1995), pp. 223–270. DOI: 10.1006/icar.1995.1190. URL: https://ui.adsabs.harvard.edu/abs/1995Icar..118..223A. Provided by the SAO/NASA Astrophysics Data System.

[43] Carrie E. Holt et al. "Brightness Behavior of Distant Oort Cloud Comets". In: *The Planetary Science Journal* 5.12 (Dec. 2024), p. 273. DOI: 10.3847/PSJ/ad8e38. URL: https://dx.doi.org/10.3847/PSJ/ad8e38.

[44] S. M. Larson and Z. Sekanina. "Coma morphology and dust-emission pattern of periodic Comet Halley. I - High-resolution images taken at Mount Wilson in 1910". In: 89 (Apr. 1984), pp. 571–578. DOI: 10.1086/113551.

[45] Michael Solontoi et al. "Ensemble properties of comets in the Sloan Digital Sky Survey". In: *Icarus* 218.1 (Mar. 2012), pp. 571–584. ISSN: 00191035. DOI: 10.1016/j.icarus.2011.10.008. URL: https://linkinghub.elsevier.com/retrieve/pii/S0019103511004015 (visited on 03/23/2025).

[46] Boyce Astro. *Brief Video Lesson CCD UBVRI and JC Filters*. URL: https://boyce-astro.org/ubvri-jc-filters/. (accessed: 30.04.2025).

[47] Said Hmiddouch et al. "Long-term TRAPPIST monitoring of a few Long Period and Dynamically New Comets." In: *European Planetary Science Congress*. Sept. 2024, EPSC2024-1139, EPSC2024–1139. DOI: 10.5194/epsc2024-1139.